

NUMERICAL ANALYSIS OF FLUID FLOW AND HEAT  
TRANSFER IN ATRIA GEOMETRIES

By

AARON KITAGAWA, B.Eng.

A Thesis

Submitted to the School of Graduate Studies

In Partial Fulfillment of the Requirements

For the Degree

Masters of Applied Sciences

McMaster University

© Copyright by Aaron Kitagawa, November 2011

NUMERICAL ANALYSIS OF FLUID FLOW AND HEAT  
TRANSFER IN ATRIA GEOMETRIES

MASTER OF APPLIED SCIENCES  
(Mechanical Engineering)

McMaster University  
Hamilton, Ontario

TITLE: Numerical Analysis of Fluid Flow and Heat Transfer in Atria Geometries

AUTHOR: Aaron Kitagawa, B.Eng, M.E.E.I. (McMaster University)

SUPERVISOR: Professor M.F. Lightstone

Number of Pages: xiii, 203

# Abstract

The design, simulation, and analysis of a reference atrium using Computational Fluid Dynamics (CFD) are presented. Atria geometries can be observed in many buildings but their understanding from an energy perspective is not fully understood. Due to the many physical phenomena occurring within these atria, it is often difficult to assess the thermal comfort, energy consumption, and functionality of an atrium's design. The scale of an atrium's structure coupled with dynamic physical phenomena creates a complex problem to solve. One particular tool that is useful in solving for detailed energy quantities is CFD. Validation studies have been conducted using previous experimental atria data to ensure confidence in the predictions. These validation studies were successful and also provided further insight on turbulence models, glazing systems, HVAC systems, thermal mass, and fluid flow and heat transfer behavior in atria geometries. A design for a reference atrium located in Toronto, Canada was then simulated for typical summer and winter conditions using various configurations for glazing, solar heat flux, wall materials, occupant load, and HVAC. These simulations provide a realistic analysis of the reference atria and conclusions for the behavior of the reference atria are made.

# Acknowledgments

I would like to thank Dr. Lightstone for her guidance and support throughout this thesis. Your kindness, insight, and support have motivated me throughout this thesis. Thank you very much.

I would also like to thank Charles Rundle, who provided me with insight and assistance throughout this work.

I would also like to thank the Solar Buildings Research Network for their support and funding throughout this thesis.

I would also like to thank Dr. Oosthuizen for his recommendations which helped me guide this research in the right direction.

I would like to thank all of the individuals who helped me along the path throughout the course of my research, this includes: professors, lab mates, family, and friends.

I would like to dedicate this work to my parents who have always encouraged and supported me in achieving my dreams. Thank you.

# Table of Contents

Abstract	iii
Acknowledgments	iv
List of Figures	vii
Nomenclature	x
1 Introduction	
1.1 Background	1
1.2 Objectives and Strategy	2
1.3 Thesis Outline	2
2 Literature Review	
2.1 Heat transfer and Fluid Flow in Atria Geometries	4
2.2 Physical Phenomena in Atria	4
2.3 Design Considerations	11
2.4 Simulation Tools	18
2.5 Previous Atria Modeling Work	21
2.6 Conclusions	27
3 Atrium Validation Studies	
3.1 Purpose	28
3.2 The Concordia University Atrium	28
3.2.1 Modeling and Simulation	31
3.2.2 Boundary Conditions	34
3.2.3 Turbulence Model	35
3.2.4 Mesh	36
3.2.5 Results	36
3.2.6 Conclusions	40
3.3 The Yokohama Atrium	
3.3.1 Experimental Data	43
3.3.2 Previous Modeling Work	44
3.3.3 Cases Considered	45
3.3.4 Boundary Conditions	46
3.3.5 Turbulence Model	51
3.3.6 Mesh	51
3.3.7 Results and Analysis	53
3.3.8 Conclusions	62
4 The Reference Atrium	
4.1 Objective	65
4.2 Design of Reference Atrium	65

4.3	Cases Considered	66
4.4	Thermal Mass of Concrete	74
4.5	Turbulence Model	89
4.6	Mesh and Grid Independence	89
4.7	Results	91
4.8	Results Analysis	120
4.9	Conclusions	129
5	Summary and Conclusions	
5.1	Summary	131
5.2	Conclusions	134
5.3	Recommendations for Future Work	136
	References	137
A	Turbulence Models in CFX	141
B	Properties of Glazing Systems	149
C	Radiation Validation Problem	156
D	Reference Atrium Case Results	162
E	Calculation of Solar Quantities	172
F	Natural Convection Validation	179

## Table of Figures

<b>Figure #</b>	<b>Description</b>	<b>Page</b>
2.1	PMV-PPD relationship	14
3.1	Image of the Concordia University EV building. Multiple atria are located throughout the middle of the building.	30
3.2	North facing interior view of the Concordia University EV building atrium.	30
3.3	Schematic of detailed geometry of Concordia University atrium.	32
3.4	Schematic of simplified geometry of Concordia University atrium.	32
3.5	Locations of lines and planes for comparison of results for simplified and detailed geometries.	33
3.6	Temperature specified boundary condition for the facade.	34
3.7	Temperature distribution comparison between simplified (left) and detailed (right) geometries at Plane 1.	37
3.8	Temperature distribution comparison between simplified (left) and detailed (right) geometries at Plane 2.	37
3.9	Temperature distribution comparison between simplified (left) and detailed (right) geometries at Plane 3.	38
3.1	u-velocity distribution for simple and detailed geometries at Line 1.	39
3.11	u-velocity distribution for simple and detailed geometries at Line 2.	39
3.12	u-velocity distribution for simple and detailed geometries at Line 3.	40
3.13	An image of the Yokohama atrium.	42
3.14	The Yokohama atrium geometry. Note that the HVAC openings (indicated by grey regions) are located on the North Wall.	42
3.15	The Yokohama atrium north wall and positioning of openings.	42
3.16	Positions of 3 measurement planes within the atrium.	43

3.17	Positions of 9 temperature measurement points within Plane 1.	44
3.18	Grid independence study using natural convection case.	52
3.19	Plot of experimental and predicted results for natural convection case.	53
3.2	Experimental and predicted temperature values for HVAC case.	54
3.21	Temperature distribution plot for HVAC case when supply is halved.	57
3.22	Temperature distribution plot for HVAC case with directed supply. Supply was aimed at Points 13 and 14.	57
3.23	Temperature distribution plot for HVAC case using solar heat flux boundary conditions.	59
3.24	Comparison of temperature specified and constant solar heat flux boundary conditions.	60
3.25	Temperature contour plots at centre plane perpendicular to south facade for: temperature specified boundary conditions and constant solar heat flux boundary condition for North Wall and Floor surfaces.	61
3.26	Temperature contour plots at the centre plane parallel to south facade for: temperature specified boundary conditions and constant solar heat flux boundary condition for North Wall and Floor surfaces.	61
4.1	Geometry of the reference atrium.	66
4.2	Sunlit area of the reference atrium for Summer Case at solar noon.	72
4.3	Sunlit area of the reference atrium for Winter Case at solar noon.	72
4.4	Temperature Profile for Temperature Specified Condition at t=7200s	77
4.5	Temperature Profile for Constant Heat Flux Condition at t=7200s	78
4.6	Temperature Profile for Surface Convection Condition at t=7200s	78

4.7	Diagram of solar heat flux hitting concrete floor, where a portion of the heat is lost due to surface convection and the remaining is lost through conduction.	80
4.8	Plot of floor temperature versus time with varying initial temperatures.	81
4.9	Plot of floor temperature versus time with varying heat transfer coefficients	81
4.10	Diagram of solar heat flux hitting concrete floor, with some of the heat being lost due to surface convection and the remaining being lost through conduction.	83
4.11	Floor temperature versus time with conduction, convection, and radiation losses. Sensitivity to the floor's initial temperature was also investigated.	84
4.12	Floor temperature with conduction, convection, and radiation heat losses with sensitivity to surrounding wall temperatures.	84
4.13	Horizontal surface radiation versus time for a clear summer day (July 1) in Toronto, Canada. The horizontal surface radiation is representative of the energy entering the atrium space.	87
4.14	150x100x100 mesh used for reference atrium simulations.	90
4.15	Grid independence study for velocities measured along a line at the centre of the atrium for summer case with single glazing with supply set to 19°C at 1m/s and heat flux on floor set to 170 W/m <sup>2</sup> .	90
4.16	Vertical planes parallel to the facade at locations 1m, 3.5m, and 7.5m away from the facade.	92
4.17	Horizontal planes at heights 1m from the floor, 2m from the floor, and 5m from the floor.	92
4.18	Vertical planes perpendicular to the facade at locations 3m, 7.5m, and 12m away from the east wall.	92
4.19	Figure 4.9 Location of lines used to measure temperatures for the base cases.	93
4.20	Temperature contour and velocity distribution plots for base summer case.	94
4.21	Temperature distribution for summer base case at Line 1.	95

4.22	Temperature distribution for summer base case at Line 2.	95
4.23	Temperature distribution for summer base case at Line 3.	96
4.24	Temperature distribution for summer base case at Line 4.	96
4.25	Temperature contour and velocity distribution plots for summer case single glazed versus double glazed.	97
4.26	Temperature contour and velocity distribution plots for summer case double glazed with and without people (6by6).	100
4.27	Temperature contour and velocity distribution plots for double glazed summer case with west wall outlet.	103
4.28	Temperature contour and velocity distribution plots for double glazed summer case with changing glazing emissivity.	105
4.29	Temperature contour and velocity distribution plots for base winter case.	107
4.30	Temperature distribution for winter base case at Line 1.	108
4.31	Temperature distribution for winter base case at Line 2.	108
4.32	Temperature distribution for winter base case at Line 3.	109
4.33	Temperature distribution for winter base case at Line 4.	109
4.34	Temperature contour and velocity distribution plots for winter case single glazed versus double glazed.	110
4.35	Temperature contour and velocity distribution plots for winter case double glazed with and without people (6by6).	113
4.36	Temperature contour and velocity distribution plots for double glazed winter case with west wall outlet.	116
4.37	Temperature contour and velocity distribution plots for double glazed winter case with changing glazing emissivity.	118

# Nomenclature

A	area
g	acceleration due to gravity
H	height
h	coefficient of heat transfer
I	radiation intensity
k	thermal conductivity, turbulent kinetic energy
L	length
Q	heat flow
$P_k$	turbulence production
$P_{kb}$	buoyancy turbulence production
q	heat flux
T	temperature
$\Delta T$	temperature stratification
t	time
U	mean velocity
$u_\tau$	friction velocity
V	velocity
v	velocity component in y direction
x	horizontal direction
$\Delta x$	grid spacing
y	vertical direction (opposite of gravity acceleration)
$y^+$	dimensionless distance from wall
Z	Zenith

## Greek Symbols

$\alpha$	thermal diffusivity
$\beta$	thermal expansivity
$\epsilon$	emissivity, turbulent dissipation
$\kappa$	von Karman constant
$\rho$	density, reflectivity
$\sigma$	Stefan-Boltzman constant
$\mu$	dynamic viscosity
$\mu_T$	turbulent viscosity
$\tau$	shear stress
$\theta_s$	solar elevation
$\omega$	turbulent frequency
$\nu$	kinematic viscosity

## Subscript

amb	ambient value
c	cold value
conv	convection value
cool	cool wall value
h	hot value
hot	hot wall value
façade	façade value
ND	dimensionless value
new	value from this iteration
old	value from previous iteration
t	turbulent value
rad	radiation value

ref	reference value
solar	solar value
wall	wall value
$\infty$	infinitely extreme value

### Dimensionless Numbers

Pr	Prandtl number $Pr = \frac{C_p \mu}{k}$
Nu	average Nusselt number $\overline{Nu} = \frac{QL}{Ak(T_h - T_c)}$
$T_{ND}$	Non-dimensional temperature
Ra	Rayleigh number $Ra = \frac{g\beta(T_h - T_c)L^3}{\nu\alpha}$
$v_{ND}$	Dimensionless velocity vector $v_{ND} = \frac{v}{\sqrt{g\beta L(T_h - T_c)}}$
$\theta$	Theta non dimensional temperature $\theta = \frac{T - T_{Amb}}{T_{Ref}}$

## **Chapter 1: Introduction**

### 1.1 Background

An atrium can be defined as a large open space, usually several stories in height with one or more large glazed surfaces which allow for sunlight to transmit through. Atria provide a very welcoming atmosphere to its occupants by providing an open meeting place where they can view the exterior environment while being exposed to natural daylight. Indeed, studies have shown that the morale and productivity of workers within the building is significantly improved by implementing structures that allow for penetration of natural daylight [Saxon 1983]. Aside from the aesthetic effects of atria, if incorporated correctly into building design they can also provide significant energy benefits through various physical phenomena. Natural ventilation, daylighting, and solar radiation can all be harnessed to reduce the overall energy consumption of the building.

Across the world there is growing concern for the environmental sustainability for energy consumption and usage. Heavily relied on natural resources are being depleted at a significant rate. While, renewable energy is one method of choice to combat the global energy crisis there is also a need to reduce energy demand through enhanced energy efficiency. Buildings currently consume a third of the world's energy supply and are also a major contributor to pollution. There are new organizations, academic research initiatives, and green building design standards that are helping to change the effect that buildings have on the environment. Newly designed buildings in recent years have become more energy efficient, less polluting, and have reduced their overall carbon footprint. As mentioned above, atria present an excellent opportunity to utilize solar

energy and natural ventilation to help make the buildings they are attached to more energy efficient.

## 1.2 Objectives and Strategy

The objective of this thesis is to explore the thermal comfort and heating, ventilation, and air-conditioning (HVAC) conditions in a reference atrium for typical summer and winter days in Toronto, Ontario, Canada. This thesis will systematically evaluate the key physical phenomena observed in atria through a number of validation studies using Computational Fluid Dynamics (CFD). Once each phenomenon can be validated for accuracy, they will be combined to simulate and analyze whole atrium systems. Furthermore, a reference atrium located in Toronto, Ontario, Canada will be modeled, simulated, and analyzed utilizing the knowledge gleaned from these previous studies. As a result of this study, recommendations and guidelines to the design and modeling of atria using CFD will be made.

## 1.3 Thesis Outline

This thesis will carefully analyze the various physical phenomena through a series of validation studies using CFD. The physical phenomena being investigated are: natural convection, turbulence, solar radiation, and conjugate heat transfer. After these analyses are made, the information derived from these studies is applied to an actual atrium located at Concordia University in Montreal, Quebec. The simulation of the Concordia University is compared to the previous validation work of Rundle [2009]. In order to

further validate predictions, an atrium located in Yokohama, Japan is also modeled, simulated, and compared with experimental results. Lastly, a reference atrium located in Toronto, Ontario, Canada is designed, modeled, simulated, and analyzed. The impact of glazing, HVAC conditions, and other boundary conditions are explored for both summer and winter conditions. Lastly, information derived from these simulations will be used to provide recommendations and guidelines for designing and modeling atria geometries using CFD.

## **Chapter 2: Literature Review**

### **2.1 Heat Transfer and Fluid Flow in Atria Geometries**

This section presents a literature review of atria systems. Heat transfer and fluid flow in atria have intricate inter-relationships of multiple physical phenomena which include natural convection, natural ventilation, convection from the HVAC system, and surface to surface radiation. Once a thorough understanding of these physical phenomena as applied to atria is accomplished one can better design and optimize atria for energy efficiency, thermal comfort, and effective functionality. The following is a literature review covering the various physical phenomena within atria, atria design considerations, building simulation tools, and previous atria modeling work.

### **2.2 Physical Phenomena in Atria**

The physical phenomena pertaining to the heat transfer and fluid flow in atria are: natural convection, turbulence, radiation heat transfer, conjugate heat transfer and natural ventilation. These phenomena are investigated below to provide a general background to better understand their application in atria systems.

#### **Natural Convection**

Natural convection flows occur when a heated body of air rises as a result of density and pressure differences between the heated air and its surroundings. Atria typically have very large scales and have the potential to create natural convection flows that are turbulent [Oosthuizen & Lightstone, 2009]. Natural convection turbulent flow

within atria can cause significant changes in heat transfer and airflow patterns which need to be carefully considered to optimize the thermal comfort of occupants and energy efficiency of the building.

### Turbulence

The majority of flows observed in atria are turbulent. This can be attributed to the overall size of typical atria and the scale of energy sources within it. Turbulence occurs when the Reynolds number exceeds a critical value causing a chaotic and stochastic behavior in its fluid motion. This random motion has a significant potential to cause greater mixing and greater heat transfer compared to laminar flows. Its unpredictable nature has made turbulent flow a problem of significant challenge in classical physics.

Turbulent flow can be solved through direct numerical solution of the Navier-Stokes equations, however, computational costs are prohibitively intensive at high Reynolds numbers. Instead, turbulence modeling has been a more popular approach for characterization of turbulent flows. Utilizing the Navier-Stokes equations and the assumption of separating the turbulent flow into mean and instantaneous quantities, turbulent flow can be modeled in many ways that are both effective and accurate. After the mean and instantaneous terms for velocity are substituted into the Navier-Stokes equations and time averaged, a term called the Reynolds stress tensor is left as a by product of the substitution. In order to close these equations, the Reynolds stress term is often approximated as a function of the turbulent eddy viscosity and the mean velocity gradients. The turbulent eddy viscosity term is similar to the kinematic viscosity term but

changes in value depending on space and time. In two equation turbulence models the eddy viscosity is represented as a function of two variables:  $k$  representing the kinetic energy and  $\varepsilon$  representing dissipation. Transport equations are developed for each variable and can be modeled and modified to fit its particular application. Two-equation models are often the ideal compromise for computing fluid velocities because of their relative accuracy and moderate computational time. For example, Murakami et al. [1996], Gocer [1996], and Schild [2000] used the  $k$ - $\varepsilon$  model to simulate airflow within atria. Their results were in good agreement with experimental measurements. Appendix A provides details on three commonly applied two equation turbulence models:  $\kappa$ - $\varepsilon$ ,  $\kappa$ - $\omega$ , and SST.

### Radiation

Radiation heat transfer plays a major role in atria systems. Sunlight enters the atrium space and causes interior objects to heat up and emit electromagnetic energy which is absorbed and reflected by other surfaces. Depending on the emissivity and temperatures of these surfaces the radiative heat transfer can be significant especially in large atria systems.

The thermophysical properties of interior surfaces and the facade are important factors when simulating atria systems. The emissivity of gypsum walls, and concrete floors are often close to that of a blackbody (i.e. emissivity close to one). Untreated glass also possesses a high emissivity value and is usually within the range of 0.90 to 0.95 [Incropera and DeWitt, 2000]. There are also numerous treatments for glass and types of

glazing systems that can significantly affect the overall heat transfer of the glazing systems. A further discussion of thermophysical properties of glazing systems can be found in Appendix B.

It is important to model radiation accurately when simulating atria. The two radiation heat transfer models that are typically available in commercial CFD codes are the Monte Carlo model and Discrete Transfer model [ANSYS, 2011]. The difference between the Discrete Transfer radiation model and the Monte Carlo radiation model is how incident radiation is calculated. The Discrete Transfer model assumes that the radiation field is homogenous and scattering is isotropic; and also solves a simplified version of the radiation transport equation. The Monte Carlo assumes the radiation field is heterogeneous and anisotropic. The Monte Carlo model tracks and calculates each photon leaving a boundary and accounts for energy that is absorbed or reflected whereas the Discrete Transfer model assumes an aggregate amount of energy landing and leaving a surface. As such, the Monte Carlo model requires a greater number of calculations to resolve the energy at each boundary.

Rundle [2009] conducted an analysis comparing the two models for a closed cube that was heated on a single side using the commercial code ANSYS-CFX . Rundle compared his predicted results with an analytical solution for three separate cases which considered a constant heat flux, a constant temperature, and a solar heat flux case. Rundle assumed the cavity was filled with a non-conductive fluid to isolate calculations for radiation heat transfer. From the analysis it was found that both models provided good predictions of the analytical results, however, computational effort was significantly

reduced with the Discrete Transfer model. As such, the Discrete Transfer model was recommended for modelling radiation heat transfer in atria. A radiation validation study was also conducted in the current research to test the accuracy of the commercial code when emissivities of wall and glazing temperatures were changed. The one dimensional problem consisted of a heated wall and a glazed surface. The emissivities of the wall and facade were changed while a constant heat flux was applied at the wall. The problem was solved analytically and numerically; and results were compared with each other. The results between the two solutions were very comparable and it was concluded that ANSYS-CFX handled the radiation problem effectively. The results of the radiation study can be seen in Appendix C.

### Conjugate Heat Transfer

Thermal mass is the property of a material to store and release heat over time. It is governed by the specific heat capacity of the material, the density of a material, and the temperature difference between itself and the surrounding environment. The thermal mass in office buildings is usually contained in walls, concrete floors, and equipment. The dynamic absorption and release of heat over time through these objects can significantly impact the heat transfer within the room especially in well sunlit areas such as the interior surfaces of atria. If the building is designed optimally, thermal mass can be used to absorb heat during a summer day and gradually released during the night when temperatures are much cooler. The time dependent effect of thermal mass and its ability

to store and release large amounts of energy makes the study of conjugate heat transfer very important.

One of the main components of an atrium that contains a large amount of thermal mass is the concrete floor. Numerous studies have been put forth to understand the heat transfer effects of concrete slab floors on the ground. One of the earliest studies to consider steady state heat transfer through a concrete slab floor was by Macey [1949]. His work provided an expression to approximate the heat loss through a concrete slab floor based on the geometry of the slab, the surface temperature of the ground, the surface temperature of the floor, and the thermophysical properties. Macey's approximation was crude at best but helped to provide a basis for the study of heat losses through concrete slabs on solid ground. Billington [1950] and other researchers modified Macey's formula to better fit experimental data.

Macey's approximation and others based off of Macey's work were based on steady state cases. Muncey and Spencer [1978], Kusuda [1982], and Delsante et al. [1988] have all provided a method to approximate transient heat losses for a slab of concrete on the ground floor. Many of these studies assume that the floor temperature is known and none of them considered an alternate case where a known solar heat flux was applied to the concrete. As such, there was a need within the current research to approximate the transient heat transfer effects of a concrete floor as applied to atria where solar heat flux, rather than floor temperature, is known. As part of the reference atrium studied in Chapter 4, the concrete floor transient heat loss with an applied solar heat flux was investigated using the fundamental semi-infinite wall solution. This analytical

solution as well as a one-dimensional transient heat conduction numerical solution was used to determine floor temperatures and heat losses seen by the reference atrium. This study can be found in Appendix D.

### Natural Ventilation

One of the major benefits of incorporating an atrium into an office building is the potential for natural ventilation. Natural ventilation is the process where a large column of air is ventilated through two or more openings placed at the top and bottom of the space. The differences in air temperature, air density, and pressure drive air from the bottom through the vents at the top.

Natural ventilation can be used to cool office buildings and provide significant savings in energy costs. For example, the thermal mass within the atrium can be cooled at night using natural ventilation resulting in cooler temperatures for the next day. Breesch, Bossaer and Janssens [2005] demonstrated the energy savings of night time natural ventilation by conducting experiments in a low-energy office building. They were able to prove that by using natural ventilation, the overall temperatures of the building envelope were much lower compared to non-naturally ventilated days. In turn, these lower temperatures reduced the overall cooling load required for the building. Holford and Hunt [2003] optimized the natural ventilation within an atrium by modifying the locations and sizes of openings. They were able to determine that the upper opening should be of intermediate size and the lower opening should be sufficiently small to enhance the effect of natural ventilation. Chen [2008] provided an overview of the

various methods that can be used to assess the ventilation performance of buildings.

Chen concluded that CFD is an effective and popular tool used to study natural ventilation mainly because of the level of detail CFD provides.

## 2.3 Design Considerations

### Aesthetic Appeal and Daylighting

The aesthetic appeal of atria can be pleasing to both occupants and exterior viewers. The openness of the atrium, daylighting, and view to the exterior environment through the large glazed surfaces provides its occupants a general feeling of calmness and a connection to the outside. Studies have shown that these building characteristics can provide significant benefits to the physiological mindset of workers causing them to feel more relaxed and motivated to conduct work [Saxon, 1983]. A well designed atrium can provide a building with a sense of uniqueness and novelty.

### Energy Efficiency

Through daylighting, natural ventilation, and controlled solar heating, energy usage can be significantly reduced with a carefully designed atrium. However, in many cases atria have not been designed with energy efficiency in mind; instead they have only been constructed for aesthetic purposes. These unsuccessful designs have all pointed to a need for improved design procedures for atria [Oosthuizen and Lightstone, 2009]. Due to the size of most atria the impact of thermal effects from the sun are amplified and it can cause significant changes in the air flow pattern, temperature distribution, and overall

energy balance of the space. In order to maximize the energy efficiency of atria the designer must understand the effect of physical phenomena occurring in atria and be able to account for them during the design process. Detailed calculation of air flow velocities and temperature distributions from the complex physical relationships occurring within an atrium requires the use of numerical solvers like CFD.

Energy efficiency is achieved through the use of energy efficient building materials, glazing systems, and HVAC systems. Building materials with high levels of insulation are implemented to limit heat transfer to the outdoor environment. Multi-layered glazing systems can have a significant impact on the insulation and incoming solar radiation in an atrium. Selecting the optimum HVAC system and settings also allows the atrium to perform efficiently and reduce energy consumption. HVAC systems are further described in the section below.

### Thermal Comfort

The thermal comfort of occupants is a very important factor when designing any building. Thermal comfort conditions are often based on air temperature, air humidity, air velocities, and personal parameters (i.e. clothing). There are three recognized standards at the international level: the International Organization for Standardization (ISO), the European Committee for Standardization (CEN) and the American Society of Heating, Refrigerating and Air Conditioning Engineers (ASHRAE). The models and assumptions used in each organization's standards are different and as a result affect the range of values for thermal comfort. Thermal comfort can be divided into two

categories: general thermal comfort and local thermal comfort. General thermal comfort looks at the overall general thermal comfort of a body of people and defines a percentage of dissatisfied people given certain environmental conditions. Local thermal comfort looks at the comfort level of occupants on an individual level considering variables such as draught, turbulence intensity, and air temperature. Currently, there is no model that combines these two categories of thermal comfort.

Fanger [1970] developed a thermal comfort model by conducting experiments in a controlled climate chamber with 1296 Danish students using a steady state heat transfer model. During these studies students were dressed in standard clothing and conducted standard activities while being exposed to different thermal conditions. For each thermal condition and activity, students were asked to record their thermal comfort using the ASHRAE thermal sensation scale. The seven point scale is defined as cold (-3) to hot (+3) with neutral being represented by (0). Fanger's model combined heat balance methods with physiology of thermoregulation to determine a range of thermally comfortable conditions. Fanger cautioned that his results were highly dependent on the individual being tested because of the individual ability of the human body to automatically adjust itself to its environment. In order to predict conditions where thermal neutrality would occur, Fanger conducted further experiments studying the relationship between activity level and physiological processes. He was able to derive a linear relationship for activity level and mean skin temperature, and another linear relationship between activity level and perspiration rate.

Fanger then substituted these relationships into the heat balance equations and an ideal comfort equation was developed. The Predicted Mean Vote (PMV) equation predicts the mean response of a large group who are thermally comfortable given a thermal condition. After several modifications of these equations using experimental data and a coupling to the Percentage of People Dissatisfied (PPD) index, Fanger's PMV-PPD model was created. The PPD index predicts the percentage of people who are dissatisfied given certain environmental conditions. As demonstrated in Figure 2.1, the relationship between PMV and PPD is symmetrical about the neutral point, where the PPD is the lowest at PMV equal to zero and highest near the extremes where PMV equals  $\pm 3$ .

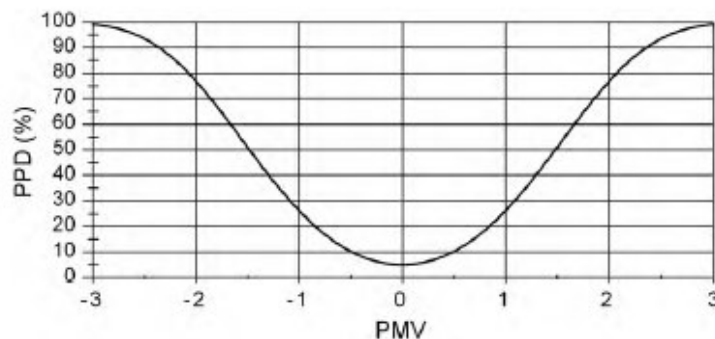


Figure 2.1 PMV-PPD relationship [Fanger, 1970].

Although there are numerous thermal comfort models, Fanger's Predicted Mean Vote and Predicted Percentage Dissatisfied (PMV-PPD) model is the most widely used and accepted general thermal comfort model. It utilizes ASHRAE's seven point scale for thermal comfort and is able to predict effectively the percentage of occupants that will be dissatisfied for a given condition within an indoor space. It should be noted that the

PMV-PPD model is useful only for predicting steady-state comfort of occupants, while other models such as the Pierce's two node model can be used to predict occupant responses for transient cases [Lin and Deng, 2008]. The PMV-PPD model is specific to each application and provides a range of operative temperatures for the space [Olsen, 2004]. It is often used as the primary model to define thermal comfort standards within occupied indoor spaces.

Different standards for thermally comfortable conditions exist due to each organizations calculation of thermal comfort. Assuming a standard indoor relative humidity of 50% for the summer, ASHRAE specifies that thermally comfortable temperatures should be in the range of 23°C -25.5°C; and for the winter assuming a standard relative humidity of 35%, ASHRAE specifies that thermally comfortable temperatures should be in the range of 20°C -22.5°C. CEN Standards recommends the following range of temperatures for the summer and winter in an auditorium type environment: 24.5°C±1.5°C and 23.5°C ±1.5°C respectively.

Acceptable velocities for occupant comfort is also an important factor of design. For office environments like atria, the acceptable air velocity for supply is 0.8 m/s and the acceptable mean air velocity for the occupied space is 0.22 m/s [ASHRAE, 2004].

### Ventilation Requirements

The quality of air is also a very important factor in the design of buildings. ASHRAE Standard 62 outlines the outdoor air requirements for ventilation and suggests that for large spaces like atria one person should have 8 L/s of outdoor air. This value is

associated with an indoor space with an estimated maximum occupancy of 150 people per 100m<sup>2</sup>. [ASHRAE, 2003]. Using these scales for large spaces the supply velocities can be determined for a number of occupant scenarios. For example, 25% occupied, 50% occupied etc.

## HVAC

Heating, Ventilating, and Air Conditioning accounts for 39% of a typical commercial building's energy consumption while the rest is consumed by lighting and equipment. High performance HVAC along with energy efficient building design can have an enormous effect on the energy consumption of the building. HVAC systems are designed to satisfy the maximum heating and cooling loads during time of maximum occupancy. During the rest of the time, it is the function of controls that ensure HVAC systems perform reliably and efficiently. Thermostats and humidistats sense the temperature and humidity within a zone and relay this information to a central control centre. The control centre then opens and closes dampers, increases and decreases temperatures of coils, and changes fan speeds to modify the air requirements. There are four types of HVAC systems that can be used in atria systems: Constant Air Volume (CAV), Variable Air Volume (VAV), dual duct and multi zone.

Constant Air Volume or reheat systems control the temperature of the supply air while keeping the flow rate constant. CAV systems cool the air in the air handler unit to meet the needs of the zone with the highest demands. The remaining zones are left overcooled and often require terminal reheat units to provide thermally comfortable

conditions. CAV systems are not energy efficient and require excessive energy to constantly power the fan and its reheat units. The main benefit of CAV systems is that they can consistently maintain loads that require low humidity.

Variable Air Volume systems control the air flow rate into the zones while keeping the temperature constant. Once a zone's temperature is satisfied, dampers are closed to control the flow rate. As the dampers are closed the pressure sensors within the main duct sense the pressure increase and reduce the fan speed. In order to meet ventilation requirements as well as temperature settings, the system is specified to constantly introduce fresh air into the zones. VAV systems are much more energy efficient compared to other systems such as CAV systems because of the ability to control the speed of the fan. Considerable energy savings can be made through the use of a VAV system [McQuiston et al., 2005].

Dual-duct systems supply air through the use of two separate ducts, one for cool air and one for warm air. A mixing box for each zone is then used to combine the warm and cool air to provide the specific air conditions for each zone. This system is responsive to spikes in sensible heat loads because of its dedicated streams of supply air; and is very flexible in satisfying numerous zones with different load requirements. The mixing of the warm air and cool air generally causes dual duct systems to be energy inefficient compared to other systems.

Multizone systems are similar to dual-duct systems with two air supplies but instead of being mixed at each zone the air is mixed at the air handler unit. The system produces conditioned air required by the zone at the air handler unit before entering the

specific zone. This system can be quite limited in its application to provide simultaneous air supplies with different air conditions. This system is suitable for applications having high sensible heat loads and limited ventilation requirements.

## 2.4 Simulation Tools

There are a number of simulation tools available for simulating heat transfer and fluid flow in atria: Building Energy Simulation (BES) programs, Zonal Model programs, and CFD programs. Each tool has its advantages and disadvantages but the application of each tool is dependent on the user's requirements of simulated information.

### Building Energy Simulation Programs

Building energy simulation programs provide energy analysis for an entire building. Spaces or rooms within the building are space averaged for temperature and analyzed as a single node connected to other adjacent nodes. BES programs do not calculate velocity and temperature quantities in detail; instead they provide a broad description of the overall energy analysis. Energy calculations are often done using empirical correlations which provide very approximate results. Boundary conditions for the building can be defined in BES programs by defining the building's construction, outdoor conditions, energy loads, and HVAC loads. Although BES programs can provide information about the energy use of a building they are not particularly useful tools for evaluating advanced design requirements such as thermal comfort. DOE-2 and

TRNSYS, and ESP-r are a few examples of BES programs that are commonly used to evaluate the overall energy performance of buildings.

Wall [1997] studied a highly glazed room during the summertime and compared experimental measurements for energy with the predictions of four BES programs: DEROB-LTH, TRNSYS, FRES, and tsbi3. He determined that BES programs often do not account for solar gains appropriately and they often over predict the amount of energy within the atrium. It was also mentioned that definitions of the boundary conditions for the building envelope were not consistent across all the BES programs tested. Some BES programs now have the capability to modify the energy gain from solar radiation and have improved overall modeling of solar radiation effects within buildings [IEA, 1996].

### Zonal Models

Zonal Models divide a volume into separate zones (medium to large sized volumes) and calculates quantities using the energy equation, continuity equation and a power law equation which describes the motion of the airflow. This model was initially developed by Bouia and Dalicieux [1991] and Wurtz [1995] to obtain an approximate and quicker solution compared to CFD models to predict air flow quantities in large indoor spaces. One of the major disadvantages of using zonal models is that each of these zones assumes a well mixed volume with a homogenous composition where temperature and density are constant while pressure varies hydrostatically. With this assumption, it is apparent that zonal models cannot predict accurate results for large indoor spaces or local airflows, however, it is an excellent tool to approximate airflow

quantities with less computational effort compared to CFD [Mora et al., 2003]. Another disadvantage of zonal models is that they do not follow the principle of conservation of momentum; instead, power law equations are used to govern the mass flow from zone to zone. There are various types of power law functions that describe particular flows like jets and plumes.

Mora et al. [2003] compared zonal and CFD predictions for isothermal airflows within a room with experimental data. Through their investigation Mora et al. [2003] were able to determine that the zonal models provided a rough estimate of airflow and did not produce accurate results when compared to experimental data. Mora et al. also compared their results with CFD simulations. CFD provided highly accurate results and a coarse grid CFD solution was recommended as a suitable replacement for the zonal method. COMIS and CONTAM are two examples of Zonal Model programs.

### Computational Fluid Dynamics

CFD is a powerful design and analysis tool that can be used to predict highly detailed information regarding airflow and heat transfer quantities. CFD is the simulation of fluid flow and heat transfer through numerical solution of a set of governing equations (e.g. conservation of mass, conservation of momentum, conservation of a scalar such as energy) on a discretized volume. The conservation of mass, momentum and scalar equations are listed in Equations 2.1, 2.2, and 2.3 respectively. Boundary conditions in CFD can be precisely defined so that an accurate and effective solution can be obtained. Moreover, modifications to an atrium's design can easily be made and tested using CFD

without the need to test experimentally. Although CFD requires more computational power, CFD is an excellent tool to evaluate thermal comfort and the effectiveness of heat transfer processes within a room. The following section looks at previous CFD atria modeling work and its results.

$$\frac{\partial \rho}{\partial t} + \frac{\partial}{\partial x_j} (\rho U_j) = 0 \quad \text{Equation 2.1}$$

$$\frac{\partial \rho U_i}{\partial t} + \frac{\partial}{\partial x_j} (\rho U_j U_i) = -\frac{\partial p}{\partial x_i} + \frac{\partial}{\partial x_j} \left( \mu_{eff} \left( \frac{\partial U_i}{\partial x_j} + \frac{\partial U_j}{\partial x_i} \right) \right) + \rho g_i \quad \text{Equation 2.2}$$

$$\frac{\partial}{\partial t} (\rho \phi) + \frac{\partial}{\partial x_j} (\rho U_j \phi) = \frac{\partial}{\partial x_j} \left( \alpha_{eff} \left( \frac{\partial \phi}{\partial x_j} \right) \right) + S_\phi \quad \text{Equation 2.3}$$

## 2.5 Previous Atria Modeling Work

There are a number of analytical, experimental and numerical simulation studies that have been done to better understand the characteristics of atrium air flow and energy transfer. Confidence in the accuracy of predicted results of atria simulations can be achieved through careful validation studies where predictions are compared against experimental measurements. This section will focus on the works that are particularly pertinent to the study of atria modeling using CFD.

Gocer et al. [2006] investigated the thermal performance of a prototype atrium design located in Istanbul, Turkey. They utilized a building energy simulation program and a commercial CFD code to simulate the various boundary conditions for typical days at the location. They were able to determine the temperature distribution within the atrium using CFD and mean temperatures for the rest of the building using a Building

Energy Simulation tool. Reasonable temperatures for the atrium as well as the office spaces were predicted but could not actually be verified as this was only a simulation study that focused on the effectiveness of the prototype building design with respect to annual energy loads.

Rundle [2010] attempted to validate CFD simulation results for an atrium located at Concordia University in Montreal, Canada. Measurements, provided by Mouriki et al. [2008], at various locations within the atrium were taken for a number of different cases. Cases consisted of varying conditions for solar gains, blinds, outdoor temperature, and HVAC. Rundle's work investigated a particular case where the blinds were closed and HVAC supply was active. According to his findings, it was concluded that accuracy for temperature and velocity values were highly dependent on modeled boundary conditions (e.g. temperature distribution on facade.) Some boundary condition simplifications were made during the course of these simulations and proved to greatly affect predictions. For example, the atrium was modeled such that an adjacent corridor was modeled as a closed adiabatic surface and infiltration through various openings were not modeled. These simplifications, although sometimes necessary to simplify the complexity of the problem, may have lead to inaccurate results. However, the modeled atrium produced reasonable qualitative trends for temperature distribution and it was demonstrated that CFD was an acceptable tool for modeling atria.

The International Energy Association (IEA) Annex 26 Yokohama Atrium was created for the purpose of better understanding the airflow and heat transfer characteristics of atria. This project was investigated by numerous researchers as a

validation study to test the accuracy of their atria modeling codes. Heiselberg et al. [1998], Hiramatsu et al. [1996], and Ozeki et al [1996] modeled the atrium for various cases for outdoor conditions, solar radiation, HVAC, and different types of glazing. Simplified assumptions were also made in the modeling of the atrium in these studies; infiltration was assumed to be minimal, and heat gain from the glazing frames were roughly estimated and not modeled. Simulated results for temperature were comparable to experimental results for the majority of cases. The results indicated that accuracy of temperature values were dependent on the estimation of the heat gain from the glazing frames. Schild et al. [1995] modeled the glazing frames and was able to achieve greater accuracy in results that were closer to experimental measurements. Hiramatsu et al. [1996] also investigated the effect of the steel frames by applying a heat balance estimation that considered the steel frames. They were able to produce an empirical correlation for the frame's heat transfer effect on the heat balance and were able to improve accuracy of simulated results as well. It was concluded that CFD was an acceptable and reliable tool to model the air flow and heat transfer within an atrium.

Kato et al. [1995] investigated an atrium design with a height of 130 meters using CFD. The atrium was sandwiched between two adjacent buildings with its glazing surfaces in the east and west directions. Corridors and offices on thirty levels were open to the atrium's air flow and these spaces were air conditioned for thermal comfort. Kato et al. attempted to assess the design of the atrium for its energy usage for a number of typical scenarios with varying conditions for solar gain, HVAC, and outdoor temperature. Using CFD they were able to adequately determine realistic results for temperature and

velocity distributions. The researchers concluded that the atrium's design could be comfortable using appropriate settings for HVAC and natural ventilation was able to relieve the high temperatures in the upper levels.

Allocca et al. [2003] investigated the effect of single sided natural ventilation for a stack of rooms sharing a vertical ventilation space. A CFD model was used to assess the effects of buoyancy and wind, on ventilation rates and indoor conditions. Predicted results were compared with empirical analytical solutions for buoyancy driven flow. The researchers considered heat sources from the rooms but without any air conditioning. Alloca et al. [2003] were able to predict CFD results within 10% of analytical solutions for buoyancy driven flow, while combined wind and buoyancy flow results were within 25% of empirical/analytical solutions.

Liu et al. [2009] investigated a reduced scale model for a building and compared their measurements with CFD results for natural ventilation. The 1/20 scale model contained a central atrium with adjacent spaces attached on all three levels. A small heater was used to simulate a heat load on the floor and air inflow was introduced through small openings in the adjacent spaces. A series of experiments and simulations were performed using a number of configurations for vents at the ceiling of the atrium. It was discovered that the outdoor temperature had a greater effect on the temperature distribution compared to using different internal thermal loads. It was suggested by Liu et al. that the buoyancy driven ventilation in a hot and humid climate (e.g. outdoor temperatures above 35°C) requires an atrium of significant height to be effective. The

model in this atrium was not high enough to achieve thermally comfortable conditions with natural ventilation alone.

Lau and Niu [2003] investigated a 25 meter high exhibition atrium located in Hong Kong. Air temperatures at six different heights were measured. A CFD simulation of the atrium was then carried out for a variety of cases and compared against measurements. The different cases consisted of combinations of heat loads from occupant load, lighting load, equipment load and floor heat source. It was determined that the different loads could be handled as one individual load when modeling the thermal load for a CFD atrium simulation. Lau and Niu noted that surface heat transfer should be carefully modeled and oversimplifications of such surfaces (i.e. treating walls as adiabatic), may lead to inaccurate results.

There have also been a variety of papers published that investigate natural ventilation using other numerical analysis tools such as zonal modeling and building energy simulation. Voelzel et al. [2001] utilized a customized zonal modeling code to simulate the IEA Annex 26 Yokohama Atrium and a small scale experiment for an atrium. Their newly developed zonal modeling code, known as AIRGLAZE, was tested for each of the above two cases and compared against experimental measurements. AIRGLAZE was based on a zonal airflow module with an envelope module that accurately models the internal distribution of shortwave and longwave radiation in a space. The results of the study compare reasonably well with experimental measurements, but were not as accurate when compared to CFD results. Zonal models

have known to have a deficiency in predicting highly accurate velocity values because zonal models do not solve the momentum equations.

Building energy simulation tools have also been utilized by researchers to study the overall energy efficiency of buildings with atria. BES tools often use empirical and analytical solutions to determine temperature and velocity distributions and therefore do not provide a high level of detail especially when compared to CFD simulations.

Laouadi and Atif [1999], investigated a three level building located in Ottawa, Canada. Each of the levels were air conditioned and were open to interact with an adjacent atrium. Laouadi and Atif used the building energy simulation program ESP-r to simulate the overall energy use of the building and to determine mean temperatures for various heights of the atrium. Mehta [2005] investigated a design for a building with an atrium using the building simulation tool COMIS. COMIS is a building energy simulation tool based on a multi-zone airflow model. Mehta was able to determine the varying temperatures of the atrium and the overall ventilation rates for the building.

There are also a few notable papers that discuss CFD and its application to atria simulation. Oosthuizen and Lightstone [2009] provide a paper that looks into some recent atria CFD validation studies, applicable turbulence models, thermal comfort, day lighting, and natural ventilation. Murakami [1992] also provides a study that discusses CFD and its application to atria simulation. Murakami looks at a few experimental cases and discusses how these cases should be modeled. Murakami provides particular emphasis on selection of turbulence models, grid discretization, and definition of boundary conditions. Finally, Schild et al. [1995] presents a paper that discusses

guidelines for CFD modeling of Atria. Schild et al. provides information on successful radiation models, wall treatments, thermal comfort and turbulence models. It is recommended by Schild that the low-Reynolds-number k- $\epsilon$  turbulence model provides greater accuracy when compared to the standard k- $\epsilon$  model [Schild, 2000] The above mentioned studies all conclude that CFD is an acceptable tool in simulating atria designs because of its ability to provide a detailed solution for air flow and energy transfer.

## 2.6 Conclusions

As a result of this literature review, it can be concluded that there is still much to understand about the behavior of fluid flow and heat transfer in atria. Experimental studies and numerical modeling of atria are limited and there is an opportunity to uncover greater knowledge of atria systems and atria simulation. CFD can provide specific details on the flow field and heat transfer of an atrium and has proven to be an excellent tool to analyze atria designs. This thesis will utilize CFD to validate predictions of experimental atria studies and to model a hypothetical atrium located in Toronto, Ontario, Canada. The results from the atria simulations will help to provide a better understanding of the pertinent factors of atria systems and atria modeling using CFD.

## **Chapter 3: CFD Atrium Validation**

### 3.1 Purpose of Atrium Validation

This section presents results of a validation study of CFD code predictions against experimental measurements and results. These studies are used to assess the accuracy and correct application of the CFD code. The use of CFD code requires a number of detailed inputs such as definition of meshes, domains, boundary conditions, turbulence models, and convergence criteria. Careful implementation of these inputs is required to provide accurate simulation results. The Concordia University atrium and the Yokohama atrium have been selected as atrium validation studies. In the following section, each atrium has been modeled, simulated and compared against experimental data to ensure that the CFD code is being used effectively and to assess the accuracy of its results.

### 3.2 The Concordia University Atrium

The Concordia University EV Building's atrium, pictured in Figures 3.1 and 3.2, was investigated by researchers at Concordia to better understand fluid flow and heat transfer within an atrium geometry. After construction of the EV building, experimental measurements for temperature throughout the entire atrium were taken by Mouriki et al. [2007]. Measurements were taken for a number of different days throughout the year for supply temperature, supply velocity, interior temperatures, outdoor temperatures, facade temperatures, and wind speeds. These data sets were then used by researchers [Cable,

2007; Rundle, 2009; Basarir, 2009] to validate CFD simulations for particular days and cases.

Rundle [2009] modeled a specific case which occurred on October 26, 2007 when the facade was covered by blinds and air conditioning was activated. The detailed geometry of the atrium and locations of HVAC openings can be seen in Figure 3.3. The boundary conditions for this case were as follows:

- A temperature distribution function was created from measurements to represent the temperature along the facade/blinds
- The HVAC inlet supplied cooled air at 0.272 m/s at a temperature of 17°C
- The back end of the atrium was modeled as a closed adiabatic surface. The actual atrium at Concordia University opens to a public corridor as seen in Figure 3.2
- Partial sunlight passing through blinds and striking the floor were modeled as additional sources of heat with a constant heat flux representative of the solar radiation measured that day.
- All remaining surfaces were treated as smooth adiabatic surfaces

Rundle [2009] was able to successfully predict overall qualitative trends when comparing predicted results to experimental measurements for this particular case.

Predicted values for temperatures were fairly accurate when compared to experimental measurements with an average error of less than 1°C. The differences between predicted and experimental values were attributed to the definition of boundary conditions in: infiltration/exfiltration, adiabatic treatment of surfaces, and the closed modeling of the

atrium's back end. Rundle was able to show that his analysis produced favorable results for the application of CFD to the modeling of fluid flow and heat transfer in atria.



Figure 3.1 Image of the Concordia University EV building. Multiple atria are located throughout the middle of the building.



Figure 3.2 North facing interior view of the Concordia University EV building atrium.

### 3.2.1 Modeling & Simulation

In further investigating the Concordia University atrium, the detailed geometry modeled by Rundle [2009] was simplified into a rectangular box to see if the simplification in geometry had a profound effect on velocity and temperature predictions. The simplified model of the Concordia University atrium was created keeping the same volume, length, and height while the width was modified to produce the same volume. As demonstrated in Figures 3.3 and 3.4, the detailed geometry's indentation along the supply/outlet wall was simplified as one flat surface creating a large rectangular atrium. The simplified model was then simulated under the same boundary conditions used in Rundle's simulations and the predicted results for temperature and velocities between the two geometries were compared. Temperatures were compared along 3 lines and 3 planes within the atrium. The locations of these lines and planes can be seen in Figure 3.5.

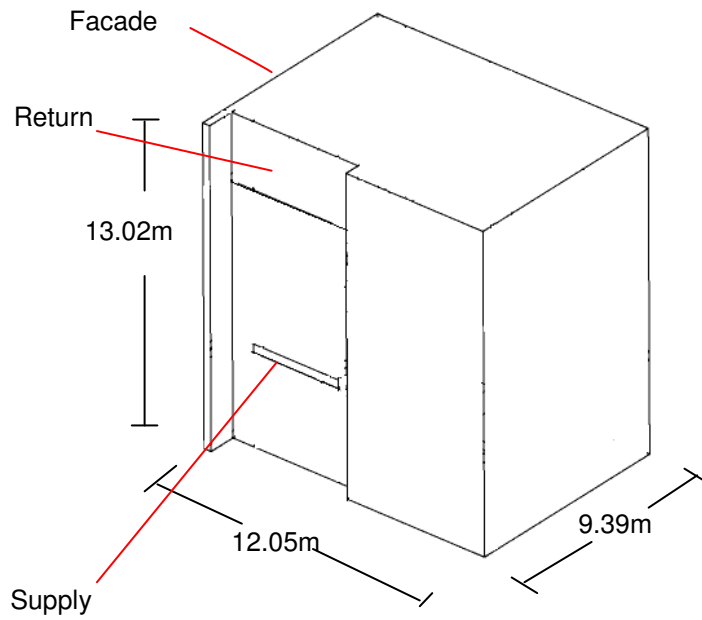


Figure 3.3 Schematic of detailed geometry of Concordia University atrium.

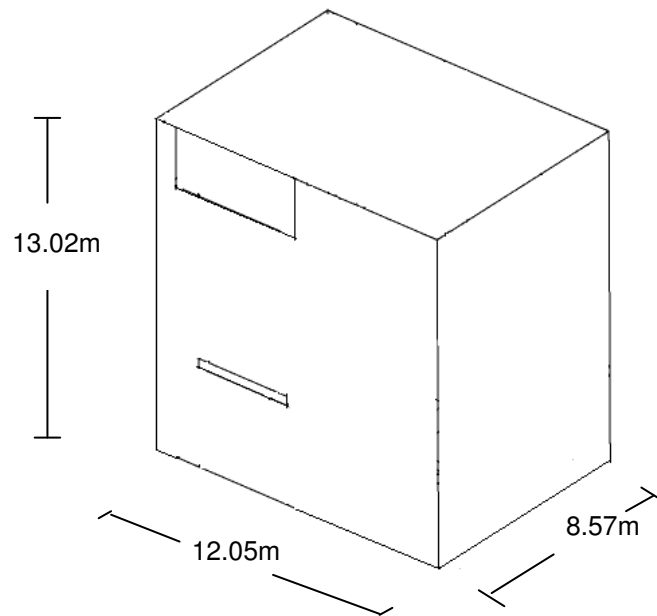
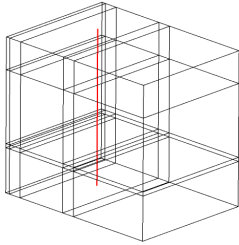
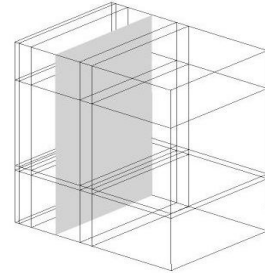


Figure 3.4 Schematic of simplified geometry of Concordia University atrium.

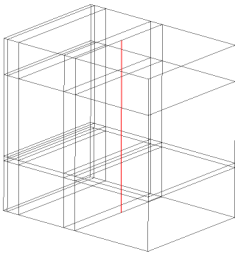
Location of Line 1



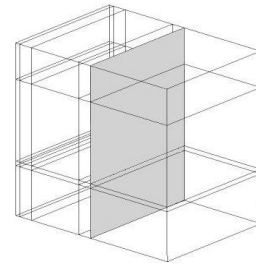
Location of Plane 1



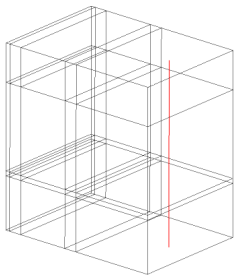
Location of Line 2



Location of Plane 2



Location of Line 3



Location of Plane 3

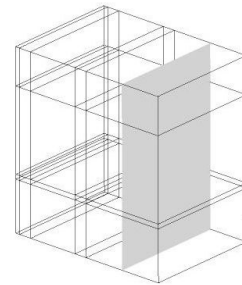


Figure 3.5 Locations of lines and planes for comparison of results for simplified and detailed geometries.

### 3.2.2 Boundary Conditions

*Façade:* The Façade was treated as a no slip wall with a specified temperature profile representative of the temperature measurements along the blinds. The temperature profile of the facade can be seen in Figure 3.6 The facade was also treated as a black body with an emissivity of one.

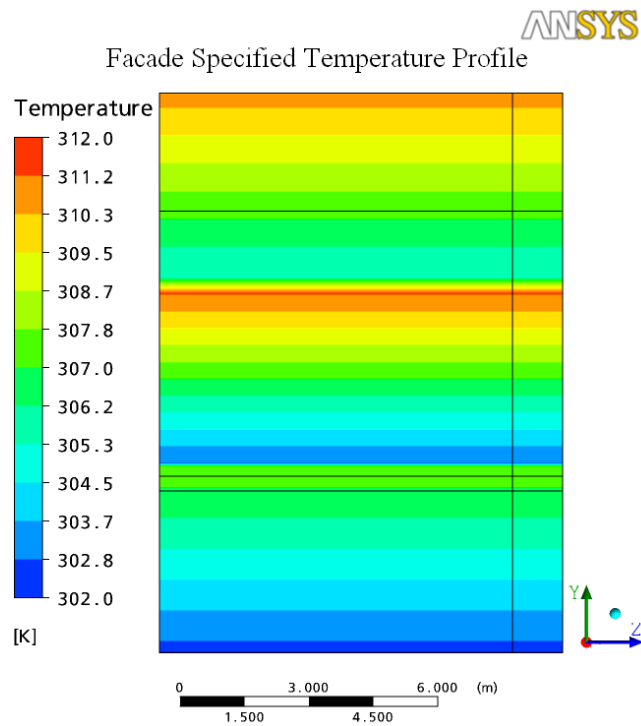


Figure 3.6 Temperature specified boundary condition for the facade.

*Floor and Walls:* The floor and walls were treated as non slip adiabatic surfaces with an emissivity of one.

*Supply:* The HVAC supply was set to provide cooled air at 17°C at 0.272 m/s into the atrium.

*Return:* The return was modeled as an opening with a relative pressure of 0 Pa and an exterior temperature of 25°C.

### 3.2.3 Turbulence Model

A turbulent natural convection study was conducted to test the performance of three turbulence models:  $\kappa$ - $\epsilon$ ,  $\kappa$ - $\omega$ , and SST to determine to best turbulence model to use for modelling flows in atria. Ampofo and Karayiannis [2003] provided experimental measurements for a differentially heated air filled cavity. The experimental set-up was modeled using ANSYS-CFX and the simulated results were compared to experimental measurements. The  $\kappa$ - $\omega$  model proved to be the most accurate of the three models tested and was determined to be the optimum turbulence model for problems involving turbulent natural convection. The details of this study can be seen in Appendix A.

### 3.2.4 Mesh

The mesh used in these simulations had the following nodal dimensions of 110 (L) x 100 (W) x 85 (H) which equates to a total of 935,000 nodes. A grid independence study was conducted to determine if predicted values were independent of the grid used. Three meshes were tested: 85x75x70 (446,250 nodes), 110x100x85 (935,000 nodes), and 150x140x120 (2,520,000 nodes). Near wall nodal spacing was also halved with each larger mesh to reduce discretization errors in those regions. The grid independence tests indicated that the 110x100x85 and 150x140x120 meshes produced results for velocities that differed insignificantly while the 85x75x70 mesh indicated values that deviated noticeably from the other two meshes. The 110x100x85 mesh was chosen as the primary mesh for both accuracy and computational efficiency.

### 3.2.5 Results

Overall the simplified geometry of the Concordia University atrium provided results that were quite similar to the results of the detailed geometry. Velocity and temperature profiles differed marginally in some areas due to the change in geometry. The qualitative trends for velocity and temperature distribution between the two geometries were comparable. The results can be seen by analyzing the temperature contour plots in Figures 3.7, 3.8, and 3.9; and the velocity profiles in Figures 3.10, 3.11, and 3.12.

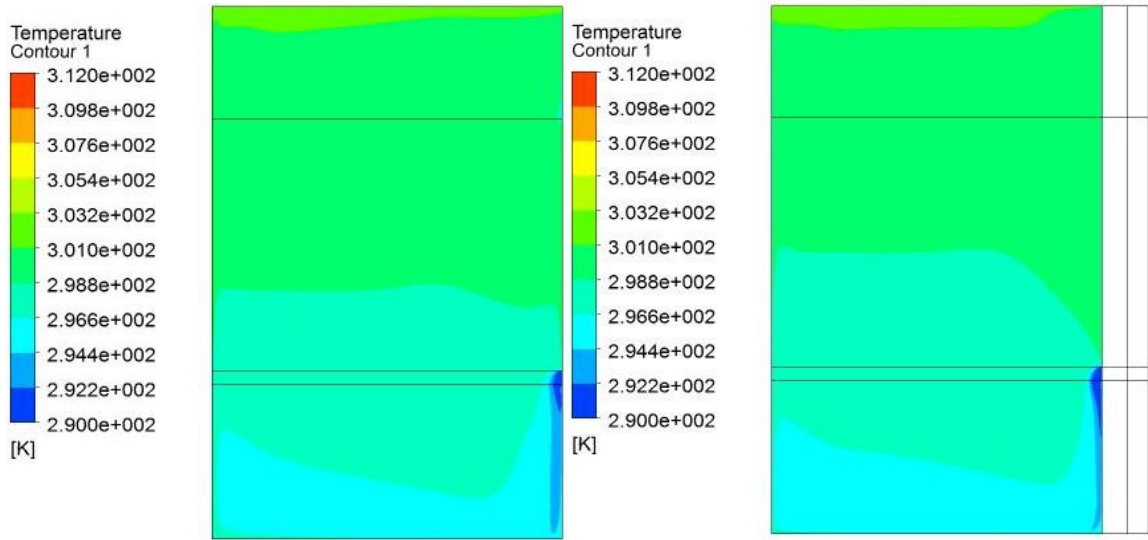


Figure 3.7 Temperature distribution comparison between simplified (left) and detailed (right) geometries at Plane 1.

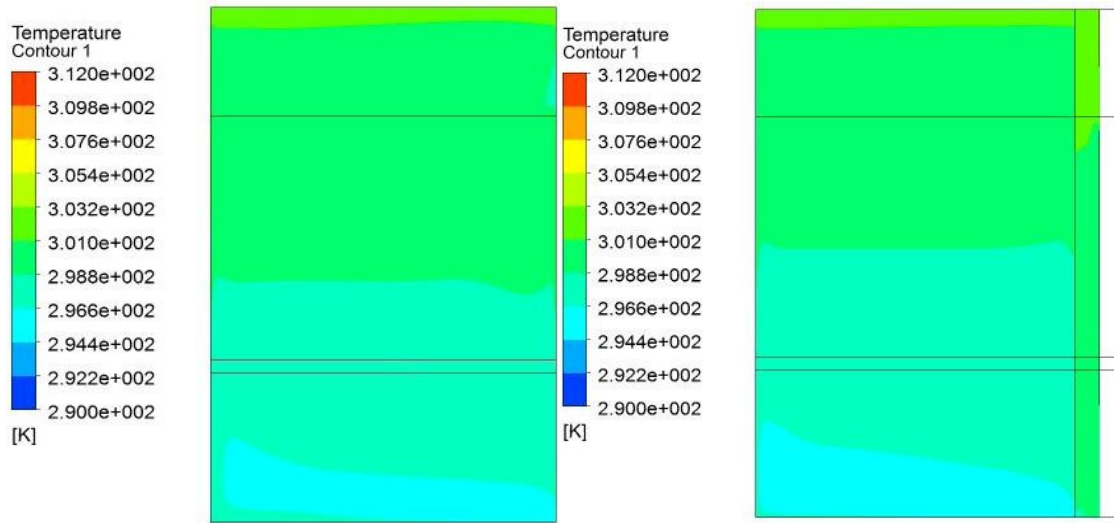


Figure 3.8 Temperature distribution comparison between simplified (left) and detailed (right) geometries at Plane 2.

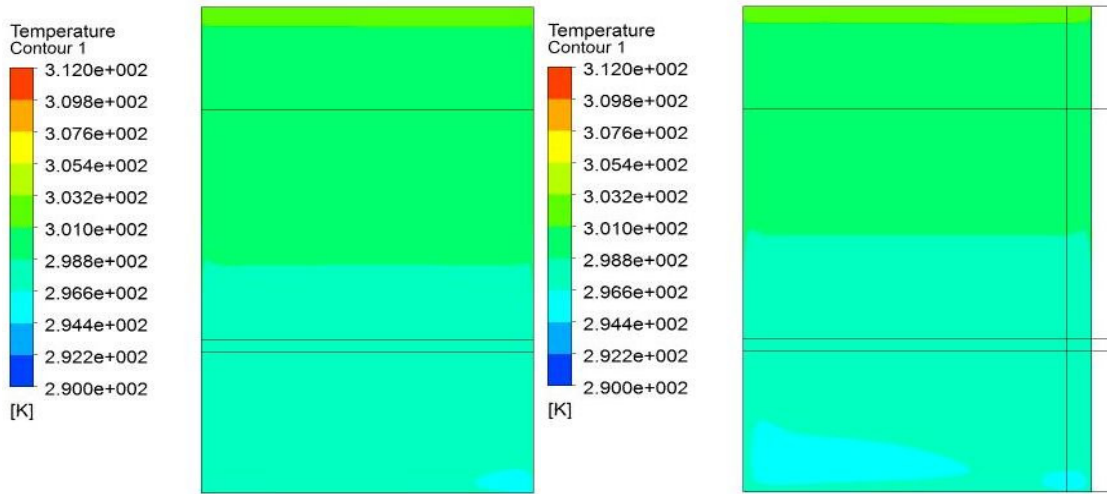


Figure 3.9 Temperature distribution comparison between simplified (left) and detailed (right) geometries at Plane 3.

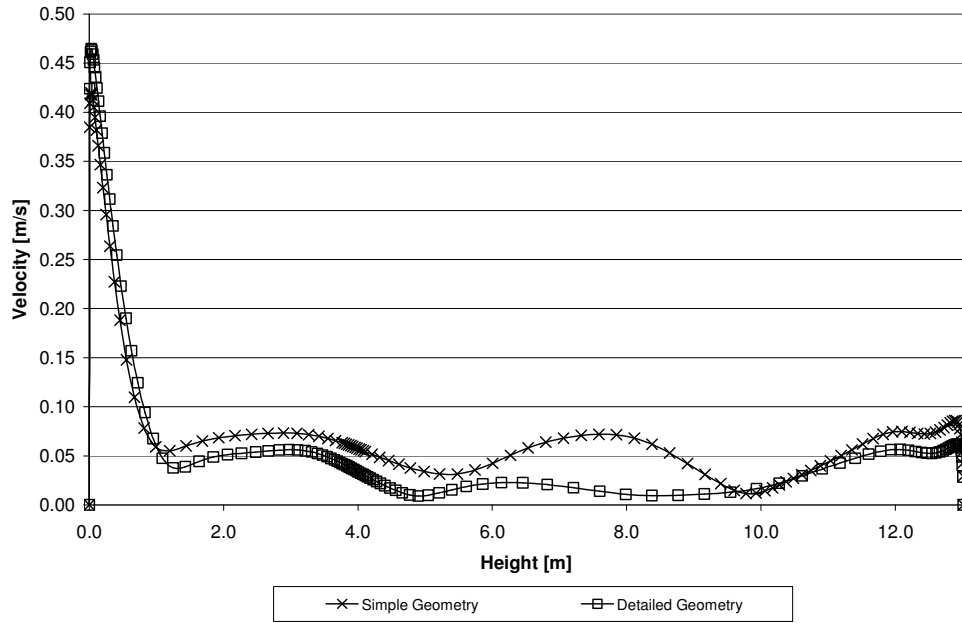


Figure 3.10 u-velocity distribution for simple and detailed geometries at Line 1.

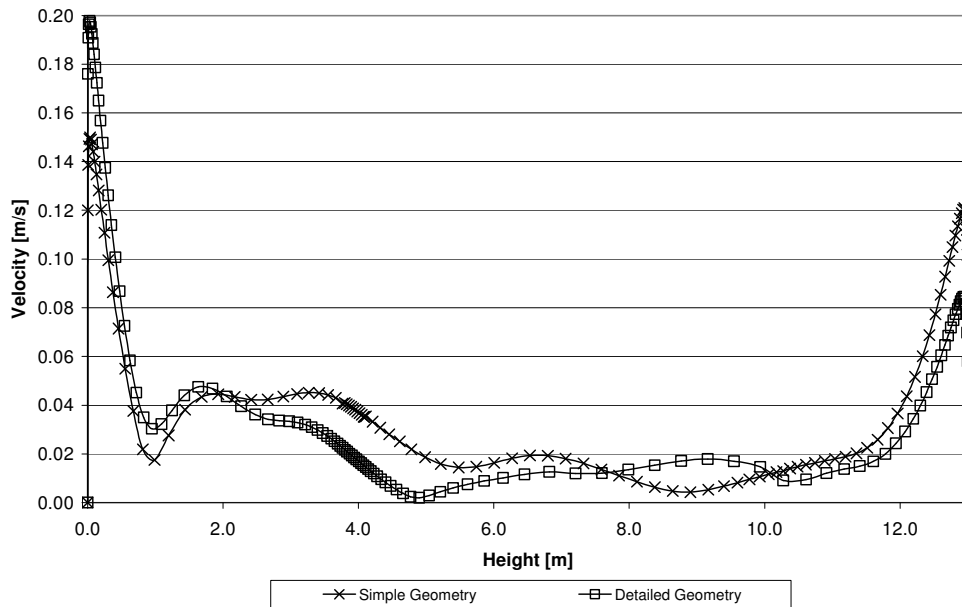


Figure 3.11 u-velocity distribution for simple and detailed geometries at Line 2.

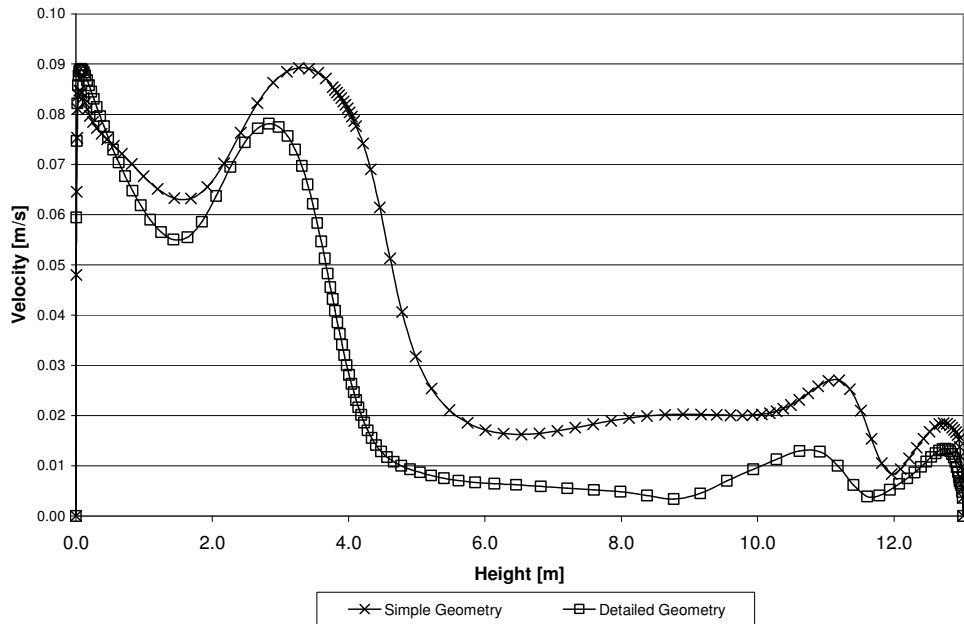


Figure 3.12 u-velocity distribution for simple and detailed geometries at Line 3.

### 3.2.6 Conclusions

According to the above figures, the simplification of the atrium has altered the air flow patterns and momentum causing slight differences in temperature and velocity predictions. Modifying the width of the detailed geometry while keeping the volume the same did affect the flow field, but overall trends particularly regarding temperature predictions were comparable to each other.

### 3.3 The Yokohama Atrium

The International Energy Association (IEA) ANNEX 26 Yokohama atrium was built in 1995 to better understand fluid flow and heat transfer within atrium geometries. This experimental atrium has been studied by a number of researchers across the world and has provided experimental data that would help to validate numerical models as applied to atrium geometries [Heiselberg et al., 1998]. The Yokohama atrium is a south facing atrium with dimensions of 7 m (L) x 4.3m (W) x 4.5m (H). The atrium has four glazed surfaces (south wall, east wall, west wall, and roof) and two insulated surfaces (floor and the north wall). The atrium was free from shading obstructions and was considered to be ideally positioned for optimum exposure to sunlight. The Yokohama atrium was tested to study three main cases: natural convection, natural ventilation and HVAC. For each case there were variations in boundary conditions such as: HVAC, solar intensity, emissivity of walls, emissivity of facade, outdoor temperature, and wind. The emissivity of the walls was tested experimentally by using black and white paint, and the emissivity of the facade was tested experimentally using different films and coatings. Researchers collected experimental measurements for numerous days covering many different case configurations. An image of the atrium is shown in Figure 3.13. The dimensions and placement of HVAC openings of the atrium can be seen in Figures 3.14 and 3.15.



Figure 3.13 An image of the Yokohama atrium.

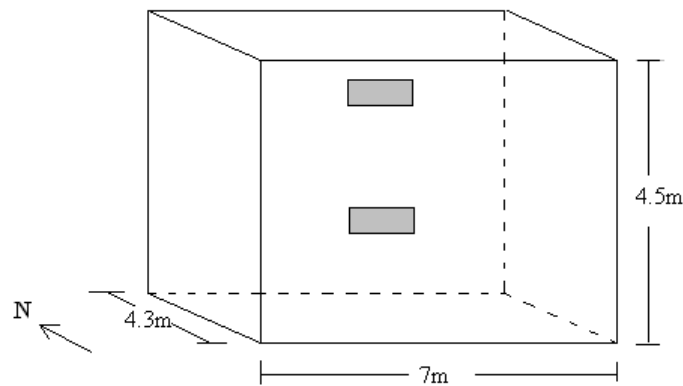


Figure 3.14 The Yokohama atrium geometry. Note that the HVAC openings (indicated by grey regions) are located on the North Wall. (The top opening is the supply inlet and the bottom opening is the exhaust.)

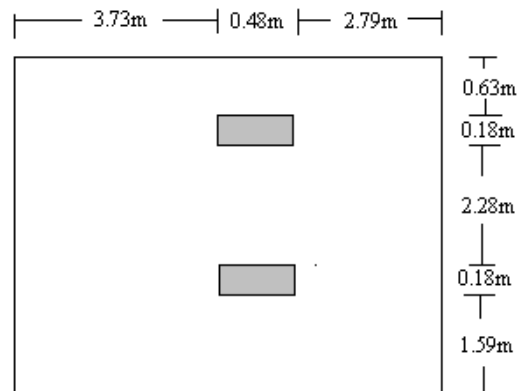


Figure 3.15 The Yokohama atrium north wall and positioning of openings.

### 3.3.1 Experimental Data

Researchers of the Yokohama atrium reported various temperature measurements inside and outside of the atrium. During the experiments the following was measured: 27 temperature points within the atrium space, 9 points along each wall/facade surface, the outdoor temperature, HVAC conditions (velocity, temperature), solar radiation, solar radiation after transmission through facade surface, and the temperature of the metal sashes. The measurements were time-integrated and logged hourly. Temperature measurements were recorded using copper-constantan thermocouples which were 200 $\mu\text{m}$  in diameter. The positions of the 3 measurement planes within the atrium and the positions of the 9 individual measurement points per plane are shown in Figures 3.16 and 3.17 respectively. A collection of three reports were used to provide the necessary data for this study: Heiselberg et al. [1998], Hiramatsu et al. [1994], and Kato et al. [1994].

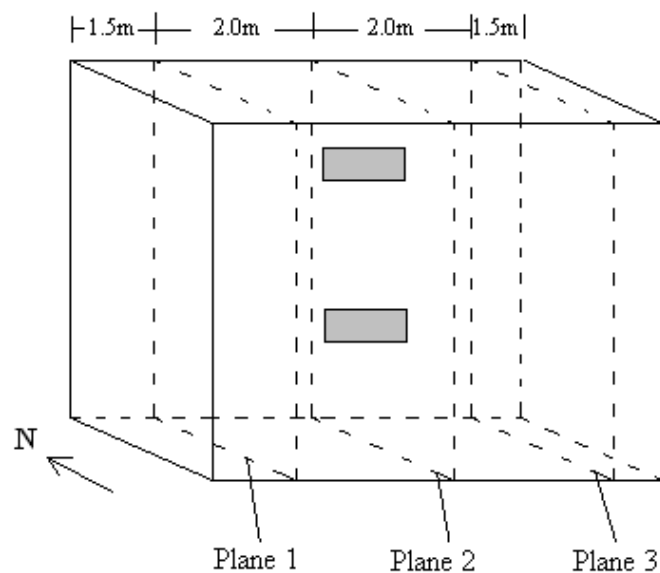


Figure 3.16 Positions of 3 measurement planes within the atrium.

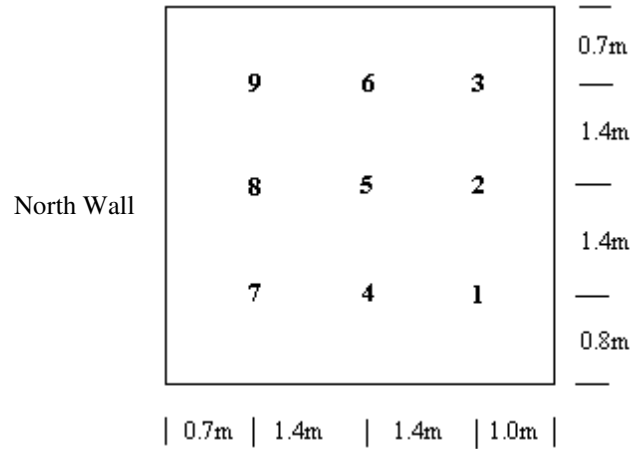


Figure 3.17 Positions of 9 temperature measurement points within Plane 1. The measurement points 10-18 (Plane 2) and 19-27 (Plane 3) follow similar positions as shown in Plane 1.

### 3.3.2 Previous Modeling Work

Researchers were able to utilize experimental data and validate their CFD predictions fairly well for a majority of the cases [Heiselberg et al., 1998]. Some of their conclusions suggest that boundary conditions for the metal frames and infiltration/exfiltration have a noticeable effect within the atrium and should not be neglected. The metal frames holding the glazing in position act as a significant source of heat and have a significant effect on the temperature distribution within the atrium. As a result, the effect of the metal frames was considered in the current modeling of the Yokohama atrium and is discussed in the boundary conditions section. Infiltration was also mentioned to be more prevalent in pressurized cases but correct modeling of

infiltration/exfiltration proved to be a challenge by most researchers and was typically neglected.

### 3.3.3 Cases Considered

In this study two cases were investigated for the Yokohama atrium: natural convection and HVAC. The natural convection case was experimented on February 2, 1994 and the HVAC case was experimented on April 4, 1994. Both cases were modeled and simulated under steady state analysis using 13:00 data. It was assumed that steady these cases could be simulated at steady state because the boundary conditions did not change significantly during this time frame. The commercial code ANSYS-CFX was used in the CFD simulations. The wall temperatures, HVAC conditions, and outdoor conditions were used to define boundary conditions for each simulation. Sensitivity to the boundary conditions for the HVAC case was studied by varying the inlet flow magnitude and direction and the solar heat flux. Table 3.1 presents a brief summary of the cases simulated.

Case No.	Description	Supply	Supply Vel. (m/s)	Wall Condition
1	Natural Convection	N/A	N/A	Temperature Specified
2	HVAC	Normal	1.4	Temperature Specified
3	HVAC	Normal	0.7	Temperature Specified
4	HVAC	Directed 1	1.4	Temperature Specified
5	HVAC	Directed 2	1.4	Temperature Specified
6	HVAC	Normal	1.4	Solar Heat Flux

Table 3.1 Summary of simulated cases.

### 3.3.4 Boundary Conditions

#### *North Wall and Floor*

The north wall and floor acted as the main sources of heat as a result of solar radiation passing through the facade and striking these surfaces. As such, higher temperatures within the atrium were found along the north wall and floor surfaces. The emissivity of the wall and facade surfaces were included as part of the boundary conditions. The natural convection case consisted of black north wall and floor surfaces while the HVAC case consisted of white north wall and floor surfaces. Emissivities of the black and white surfaces were 0.95 and 0.90 respectively. Table 3.1 is a summary of the thermophysical properties of the building envelope.

<b>Surface</b>	<b>Shortwave Absorptance Inside/Outside</b>	<b>Shortwave Transmittance</b>	<b>Long Wave Emissivity Inside/Outside</b>
Glass	0.19/0.33	0.37	0.30/0.84
Floor (black)	0.91/-	0	0.95/-
Floor (white)	0.20/-	0	0.90/-
Wall (black)	0.98/-	0	0.95/-
Wall (white)	0.20/-	0	0.90/-

Table 3.1 Thermophysical properties of envelope materials.

Temperature measurements at nine locations for each wall and the facade interior surface were provided by Hiramatsu [1994]. Due to the small temperature differences (i.e. temperature differences of 0.3 to 1°C) along each wall, temperature measurements for each surface were averaged and applied as a uniform average temperature in the simulations. Averaged temperatures were applied to all wall and facade surfaces. Table 3.2 and Table 3.3 indicate the temperature boundary conditions used for each case.

#### *Facade Surfaces*

The roof, east, west, and south facing surfaces were all glazed. The inner emissivity of the glass used during the time of these experiments was reported to be 0.3. The facade surface temperatures did not include the metal frames; the metal frames were considered as a separate boundary condition.

<b>Surface</b>	<b>Temperature [K]</b>
North Wall	329.52
Floor	329.26
South Façade	314.44
Roof Façade	311.34
East Façade	300.28
West Façade	303.05
Metal frames	322.82

Table 3.2 Temperature boundary conditions for the natural convection case.

Surface	Temperature [K]
North Wall	319.38
Floor	319.19
South Façade	316.81
Roof Façade	320.48
East Façade	307.42
West Façade	312.75
Metal frames	324.65

Table 3.3 Temperature boundary conditions for the air conditioned case.

### *Metal Frames*

Information about the geometry and the construction of the metal frames was missing from published reports. It was reported by Heiselberg et al. [1998] that the steel frame's overall surface area covered approximately 10% of the entire facade surface area. According to images of the atrium and the above approximation, the metal frames were approximated to have a width of 0.12m. Using this assumption and the layout of metal frames as seen in Figure 3.11, an expression was created in ANSYS-CFX to model the presence of the steel frames. The reported metal frame temperatures were then applied to these boundaries.

### *HVAC*

For the HVAC case, the supply and exhaust temperatures were provided as well as the supply's average velocity. No other information was provided by published reports about the HVAC system with respect to direction of air supply or use of supply diffusers (i.e. air supply profile). The supply velocity was reported to be 1.4 m/s and the direction of the supply air was assumed to be normal to the supply inlet. The temperature of the supply for the HVAC case was set to 298.15 K.

### *Constant Heat Flux from the Sun*

An alternative boundary condition was also considered in place of the temperature specified boundary condition for the north wall and floor surfaces. The solar radiation on the north wall and floor surfaces was modeled as constant solar heat fluxes. A constant heat flux absorbed by the north wall and floor was calculated using the applicable solar radiation data and solar position calculations. (See Appendix E for solar angle and solar radiation formulas.) Yokohama, Japan is located at a latitude of 35°27N and a longitude of 139°28E. Table 3.4 provides a summary of all solar angle quantities and solar radiation values for the north wall and floor surfaces.

Quantity of Interest	Value
Angle of Declination	5.6°
Local Standard Time Meridian	135°
Equation of Time	-3.1
Time Correction Factor	12.9
Local Solar Time	13.22°
Hour Angle	18.225°
Altitude Angle	56.2°
Azimuth Angle	213.7°
S incident	162 W/m <sup>2</sup>
S horizontal	134.3 W/m <sup>2</sup>
S tilted	90.7 W/m <sup>2</sup>

Table 3.4 Solar angles and radiation values for April 5, 1994 13:00.

### *Steady State Simulations*

Boundary conditions for the atrium were considered to be close to steady state since changes in heat flux from walls, sun, and outdoor conditions were gradual over time. Previous studies of steady state atrium simulations have produced successful results and have indicated that steady state solutions are accurate depending on the boundary conditions considered as well as the amount of thermal mass present. Steady state simulations were performed for the entire investigation of the Yokohama atrium. Other researchers simulating the Yokohama atrium have also used steady state analysis and have predicted fairly accurate results.

### 3.3.5 Turbulence Model

Previous work studying the performance of turbulence models using ANSYS-CFX under natural convection flows within closed cavities suggested that the  $k-\omega$  model provided the most accurate results. Turbulence model performance and selection criteria are described in detail in Appendix C. As a result of previous CFD benchmark validation studies, the  $k-\omega$  turbulence model has been selected as the most accurate choice for simulating air flow and heat transfer within atrium geometries.

### 3.3.6 Mesh

Three meshes were tested for grid independence using the natural convection case. Figure 3.18 displays the results for the grid independence test. The grid independence study tested the following meshes: 90x80x80 (576,000 nodes), 120x110x110 (1,452,000 nodes), and 200x180x180 (6,480,000 nodes). By examining the results in Figure 3.18, it can be seen the differences between the 90x80x80 and 120x110x110 meshes are evident while a comparison between the 120x110x110 and 200x180x180 meshes indicate results are quite close to each other. As a result of this grid independence test the 120x110x110 mesh was determined to be grid independent and was selected for use in the atrium simulations.

The HVAC case solution was particularly sensitive in areas such as the walls, supply and outlet; this required greater refinement near these areas to minimize grid sensitivity and to optimize convergence. The average  $y^+$  values were approximately 2.5 throughout the entire domain.

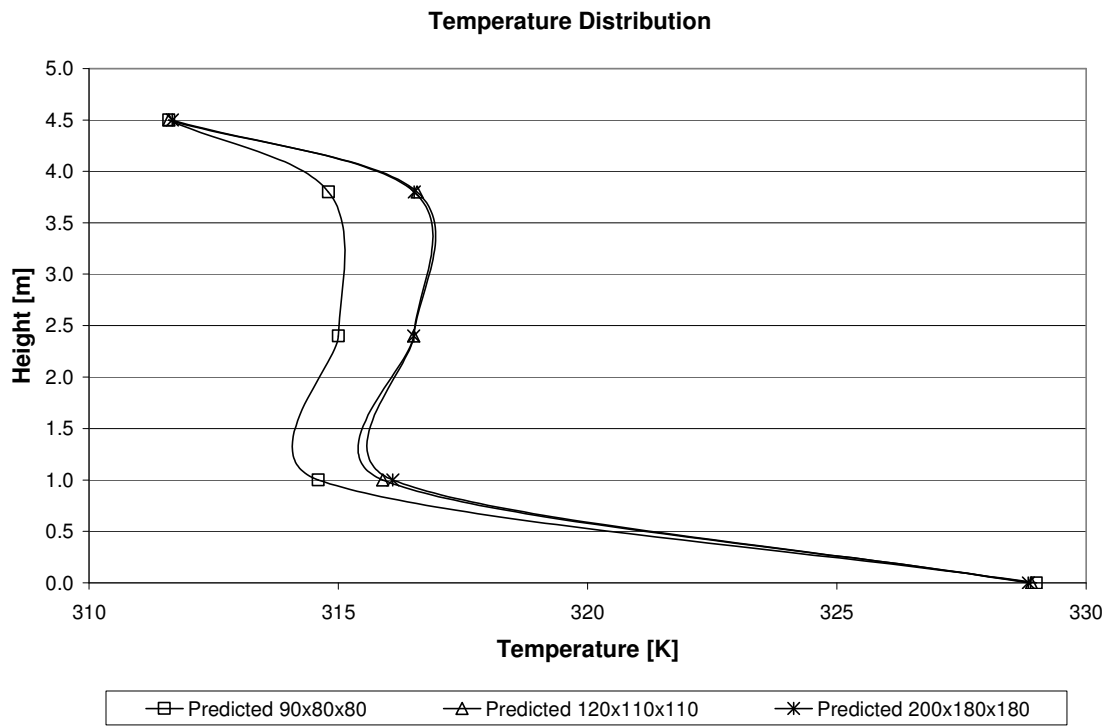


Figure 3.18 Grid independence study using natural convection case.

### 3.3.7 Results and Analysis

#### *Natural Convection Case*

A graph comparing measurements and simulated results for the natural convection case can be seen in Figure 3.19. Simulation results with and without the effects of the metal frames are shown. Both cases under predict the experimental data, however, the addition of the metal frames in the model allows for greater accuracy in the simulated solution. On average, the difference between the predictions (with the effects of the metal frames included) and the experimental is 1-2 K. For a temperature range of approximately 30 K seen in the simulation, the error is approximately 5%.

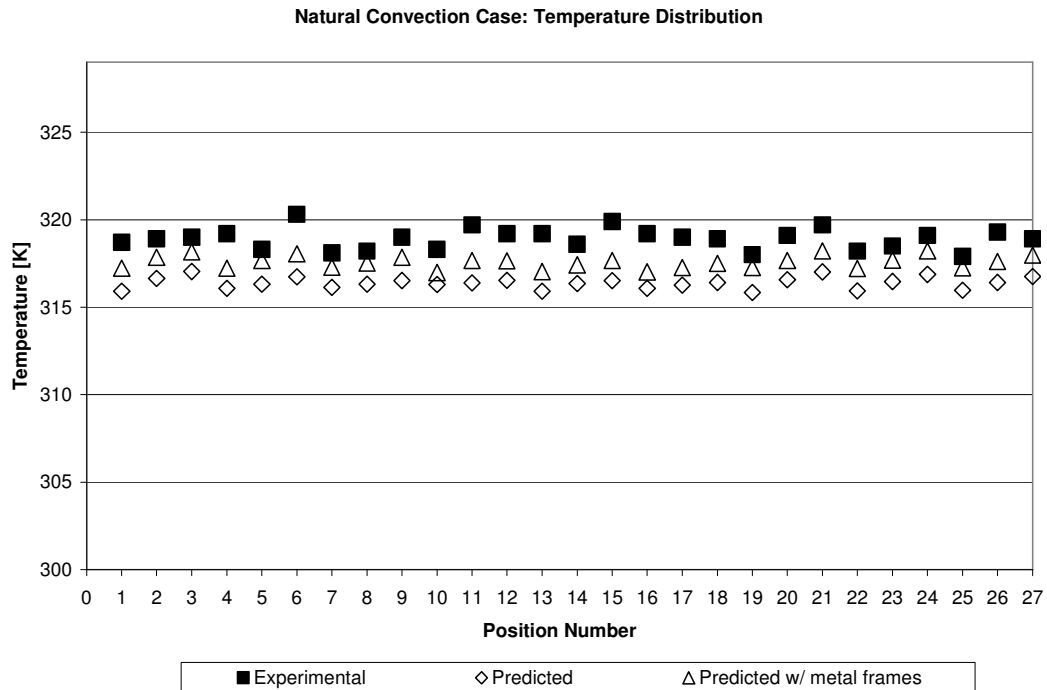


Figure 3.19 Plot of experimental and predicted results for natural convection case.

*HVAC Case*

In the HVAC case, the differences between experimental and predicted results (predicted with metal frames) range from 3-5 Kelvin depending on the location as demonstrated Figure 3.20. The addition of the metal frames had a similar effect to the overall predicted temperatures as the natural convection case and increased overall temperatures by approximately 1 Kelvin. There is a noticeable difference in trends between the experimental and simulated results. Often the experimental measurements have colder middle points (e.g. points 2, 8, 14, 20, 26) compared to the bottom points as can be seen in the figure. Predicted results suggest a slight upward stratification should exist and this trend should be common throughout all measurement planes.

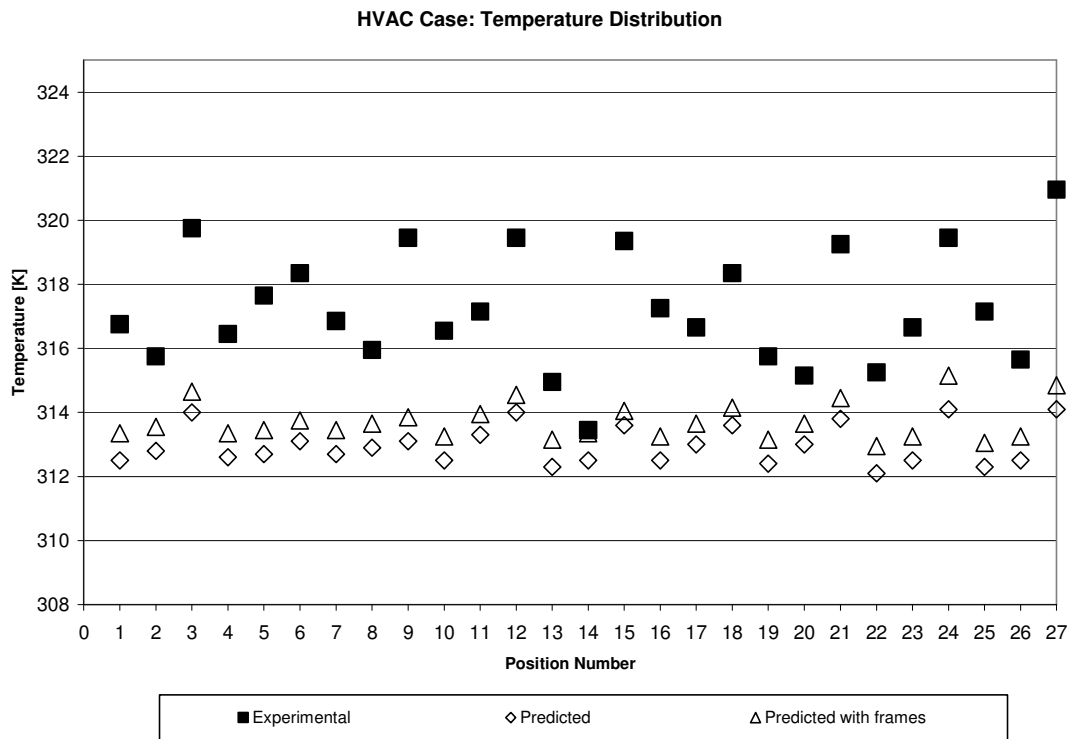


Figure 3.20 Experimental and predicted temperature values for HVAC case.

This discrepancy in results between experimental and predicted has indicated that this particular case may be affected by other factors such as uncertainty in: direction of air supply, mass flow of air supply, temperature of air supply, possible sources of infiltration/exfiltration and uncertainty in temperature measurements. It is mentioned by Heiselberg et al. [1998] that the thermocouples used were not shielded from solar radiation and measurements were not adjusted to account for temperature increases due to direct solar radiation. These uncertainties have not been significantly addressed in previous literature and have resulted in the current study to investigate further as to the root cause of these differences in results. It should be noted that researchers simulating HVAC cases have also reported similar results that were inaccurate by similar magnitudes [Heiselberg et al. 1998]. These researchers were also not able to produce the trends observed by experimental data.

Utilizing an energy balance of a thermocouple [Carvalho et al., 1990] and the limited information regarding the thermocouples used in this study, an approximation of the thermocouple error due to radiation was calculated and determined to be approximately 1.5 K for the HVAC case. However, due to the limited information of the thermocouples and the position of the metal frames this approximation cannot be applied to all temperature measurement points. Certain measurement points may have been shaded by the frames (i.e. solar radiation) while others may have not.

Sensitivity studies to boundary conditions were performed to determine their effects on predicted air temperatures. These studies included: changing the velocity of the air supply, changing the direction of the air supply, and changing the temperature

boundary conditions for the north wall and floor surfaces to constant solar heat fluxes. The first approach was to change the magnitude of the supply's velocity to 0.7 m/s (half of the velocity reported) while keeping the direction normal to the supply. Reducing the supply velocity would allow for less cooling of the atrium and would increase predicted temperatures. As demonstrated Figure 3.21, predicted results were approximately 1.5 Kelvin higher but trends continued to be predicted in a similar fashion as the original case and did not necessarily indicate improvement in accuracy. All predicted results continued to produce noticeably lower temperatures which indicate that the internal energy within the atrium was too low.

The second approach was to change the direction of the air supply by aiming the air supply towards one of the coldest measurement points (e.g. Points 13, 14). Keeping the magnitude of the velocity at 1.4m/s and the supply temperature at 298 Kelvin produced some changes in the flow pattern and temperatures. Figure 3.22 is a graph of the results for the HVAC case with the directed HVAC supply. Temperatures at positions 16 and 17 were significantly colder with other points remaining relatively the same. Slight stratification can still be observed with bottom temperature points around 313 Kelvin and upper temperature points close to 315 Kelvin. However, it can be seen by Figure 3.22 that predictions of experimental values have not improved significantly in accuracy and one can conclude that there isn't enough energy entering the atrium space.

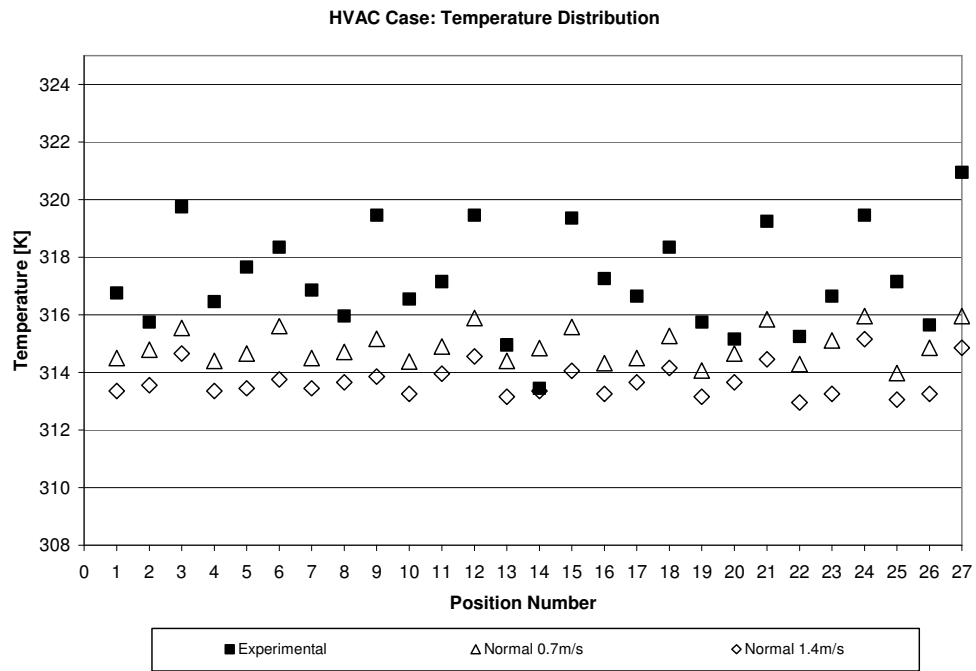


Figure 3.21 Temperature distribution plot for HVAC case when supply is halved.

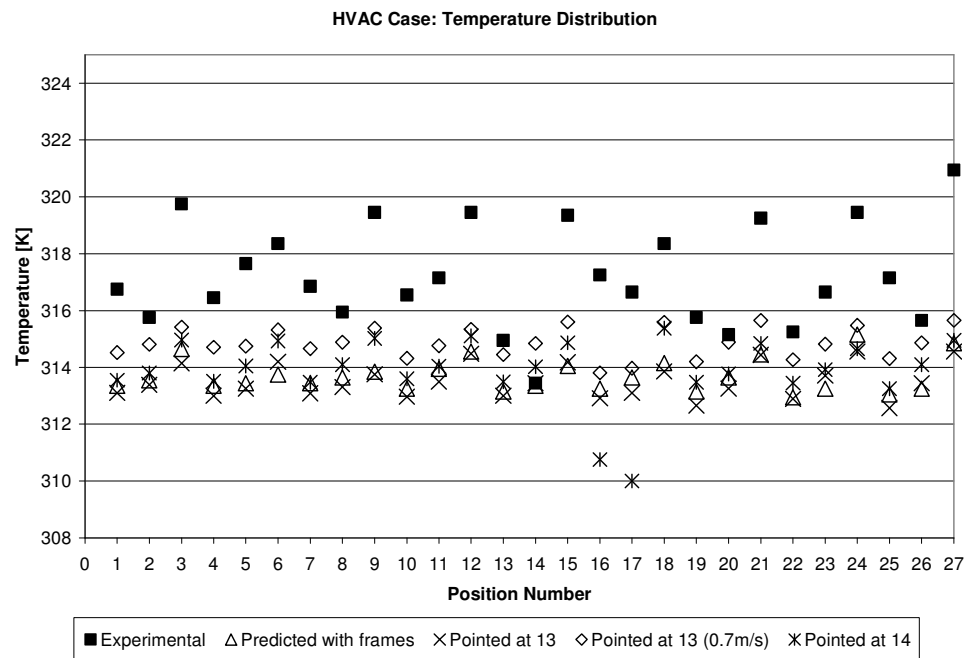


Figure 3.22 Temperature distribution plot for HVAC case with directed supply. Supply was aimed at Points 13 and 14.

The third approach was to eliminate the temperature boundary conditions for all surfaces, and replace them with a constant solar heat flux applied to the north wall and floor surfaces. As mentioned earlier in the boundary condition section of this study, solar angles and resulting solar radiation for April 5, 1994 13:00 were calculated. Heat fluxes for both the north wall and floor were calculated and inputted as boundary conditions.

The results using constant heat fluxes noticeably improved results as predicted temperatures were much closer to experimental measurements. Trends were in much better in agreement compared with experimental data and the difference in magnitude reduced to approximately 2-3 Kelvin depending on the position. Stratification is slightly more apparent and the peculiar trends for points 13 and 14 have also been predicted by the simulation. Figure 3.23 is a plot of the results for the simulation with constant solar heat fluxes for the north wall and floor. These results suggest that the amount of energy entering the atrium in the simulation case is now more equivalent with the experimental case. It was also investigated to see the effect of changing the altitude angle with respect to time (e.g. one hour ahead and one hour behind). Changing the altitude angle affected the total solar radiation incident on the north wall and floor and resulted in differing results. Results for these cases can also be seen in Figure 3.23. It can be said that accuracy with respect to changing the altitude angle does not improve, as the original altitude angle for 13:00 and associated solar radiation fluxes provided the best results.

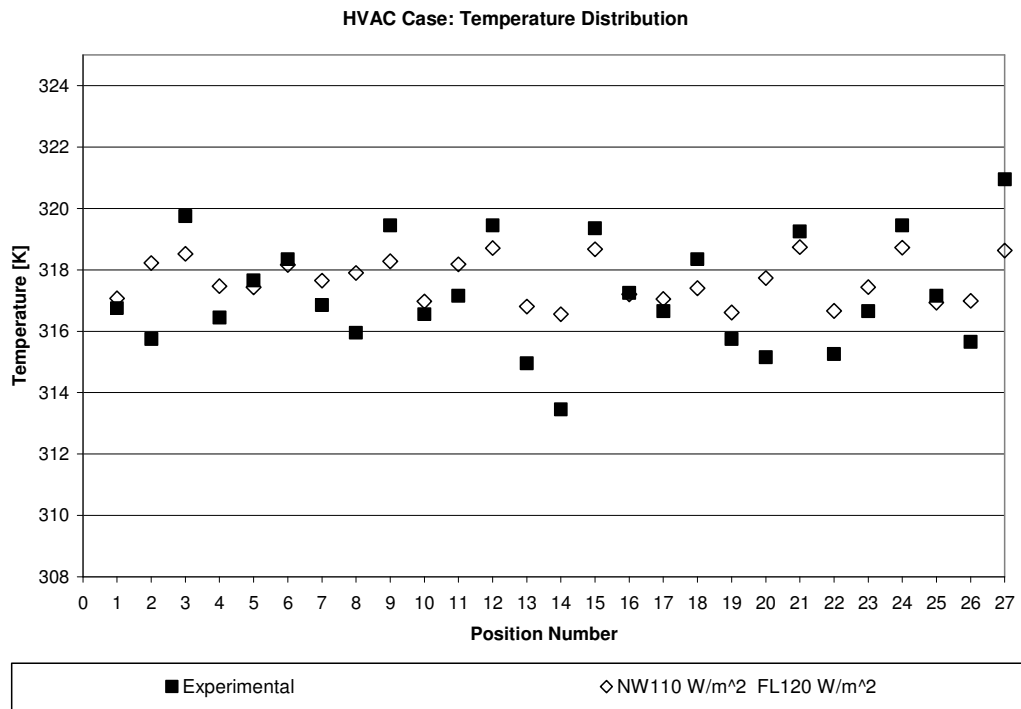
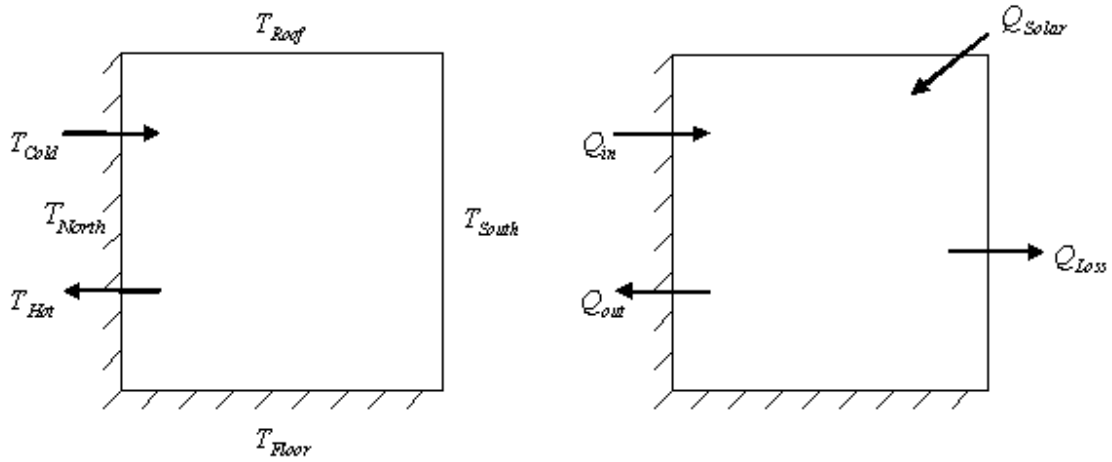


Figure 3.23 Temperature distribution plot for HVAC case using solar heat flux boundary conditions.

Upon further inspection, the temperatures of the north wall and floor between the temperature specified boundary condition and the constant solar heat fluxes cases were compared. There is approximately a 10-12 Kelvin difference between the temperature specified case and constant heat flux case for the North Wall/Floor surfaces. An energy balance described by Figure 3.24 and Table 3.5 indicate that there is a difference of approximately 2.2 kW of energy between the two cases. Figure 3.25 presents temperature contour plots at the midplane perpendicular to the South Facade. Figures 3.27 and Figure 3.28 are temperature contour plots at a plane parallel to the north wall ( $z = 2.1\text{m}$ ). As demonstrated by these contour plots there is much more energy in the constant solar heat flux case than the temperature specified case.



$$Q_{out} = Q_{in} + \sum Q_{Walls}$$

$$Q_{out} = Q_{in} + Q_{Solar} - Q_{Loss}$$

Figure 3.24 Comparison of temperature specified and constant solar heat flux boundary conditions.

Quantity	Temp Specified Case (kW)	Constant Heat Flux (kW)
Qout	-2.1	-3.6
Qin	-2.4	-3.1
$\Sigma Q$ walls or (Qsolar-Qloss)	4.5	6.7

Table 3.5 Comparison of energy balance within the atrium under different boundary conditions.

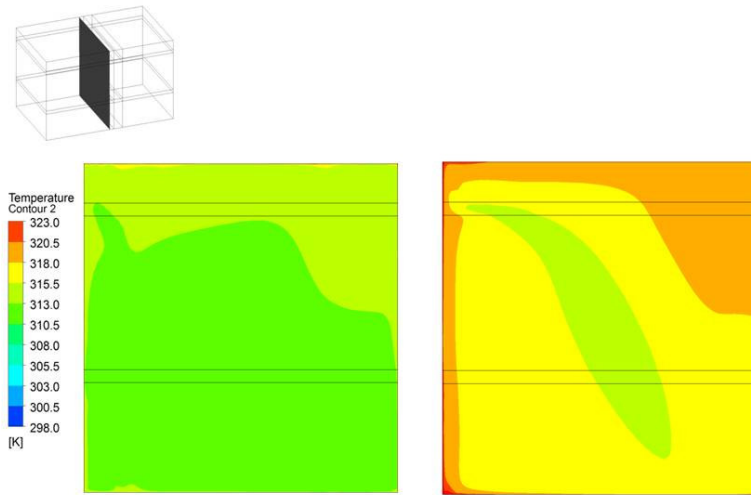


Figure 3.25 Temperature contour plots at centre plane perpendicular to south facade for: (Left) temperature specified boundary conditions and (Right) constant solar heat flux boundary condition for North Wall and Floor surfaces.

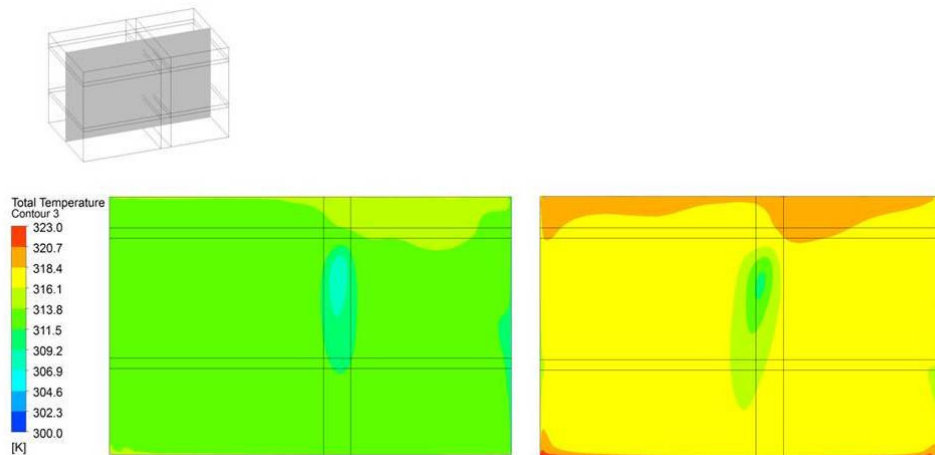


Figure 3.26 Temperature contour plots at the centre plane parallel to south facade for: (Left) temperature specified boundary conditions and (Right) constant solar heat flux boundary condition for North Wall and Floor surfaces.

### 3.3.8 Conclusions

The IEA Annex 26 Yokohama atrium study was one of the earliest experiments which provided data to better understand fluid flow and heat transfer in atrium geometries. This data was intended to provide a foundation for researchers to validate numerical codes such as CFD as applied to atria. In the current study the Yokohama atrium data was analyzed for two cases: natural convection and HVAC. Both of these cases were modeled and simulated; and predicted results were validated against experimental data.

The natural convection case provided fairly accurate results and accuracy further improved to an average error of 5% once the metal frames were included into the atrium model. The metal frames provided a moderate source of energy and affected the overall heat transfer in the interior atrium space.

The HVAC case proved to be more of a challenge, as initial predictions using temperature specified boundary conditions under predicted experimental results by about 3-5 Kelvin and qualitative experimental trends were not well followed by predicted results. It was observed that the initial model did not account for enough energy into the atrium space as temperatures were under predicted quite noticeably even though reported temperature boundary conditions were specified. Different approaches were first tested to determine the airflow's sensitivity to the air supply's velocity and direction. Some trends improved when changing the supply's direction and velocity but all results were still under predicted compared to experimental data. As a final attempt to improve the accuracy of predicted results, temperature boundary conditions for the north wall and

floor were replaced with constant heat fluxes representative of the solar gain. The solar gain was distributed realistically using solar angle and radiation calculations for Yokohama, Japan for the specified time and date. As a result of changing these boundary conditions, trends and results greatly improved and were much closer to experimental data. However, when comparing the north wall/floor temperatures of the temperature specified case and the constant heat flux case there was a difference of 10-12 Kelvin. This difference is quite significant and indicates there may be sources of error that need to be considered. Previous researchers simulating the Yokohama atrium HVAC case have also reported results indicating larger discrepancies between experimental and predicted temperatures [Heiselberg et al., 1998]. The following reasons should be considered as possible causes for the difference in results for the HVAC case:

- Temperature specified boundary conditions are averaged from experimental data points. By doing this, temperature gradients along facade surfaces and their effect on the atrium air flow are not appropriately accounted for. Temperature differences between the averaged temperatures and specific points are in the range of 1-2 Kelvin depending on the surface.
- Kato et al. [1994] reports that the supply air temperature could not be kept constant when the cooling load was at a maximum. (i.e. when the temperature of the room becomes very high) The cooling capacity of the cooling system was insufficient and could not provide steady state conditions during the hottest conditions. This unfortunate condition could have easily altered accuracy and consistency of experimental measurement data.

- The thermocouples used during experimental measurements were not shielded from solar radiation and may have easily caused higher temperature measurements. This point is mentioned as a source of error by Heiselberg et al. [1998].

Overall, the Yokohama atrium study provided a basis to test the accuracy of the commercial CFD code ANSYS-CFX as applied to the modeling and simulation of airflow and heat transfer within atrium geometries. Much like most CFD simulations, it is imperative that boundary conditions are modeled accurately to obtain accurate predicted results.

## **CHAPTER 4: Reference Atrium**

### 4.1 Objective of Reference Atrium

This section applies the results and knowledge gained from the previous sections to the analysis of a hypothetical reference atrium located in Toronto, Canada. The reference atrium is simulated for typical summer and winter days during solar noon with the objective of satisfying thermal comfort conditions while also optimizing HVAC energy usage. The effects of solar radiation, outdoor temperature, glazing system properties, thermal mass, occupant heat loads, and HVAC settings on the heat transfer and fluid flow in the atrium have been studied. The goal of this work is to study the heat transfer and fluid flow in a reference geometry and then assess the response to changes in relevant variables.

### 4.2 Design of Reference Atrium

#### Geometry

A typical atrium usually possesses the following characteristics: a large occupiable space with multiple storeys in height, one or more surfaces are glazed, and the space is ventilated through mechanical and/or passive systems. For the purpose of simplifying the analysis, the hypothetical reference atrium was modeled as a rectangular box and was defined to have the following dimensions: 15m (L) x 10m (W) x 10m (H). The atrium faces the south direction with its south face being the only glazed surface. The HVAC system is similar to the Concordia University atrium and has the supply inlet

and exhaust outlet on the east wall. The supply inlet has an area of  $2\text{m}^2$  and the exhaust outlet has an area of  $15\text{m}^2$ . The design of the reference atrium can be seen in Figure 4.1.

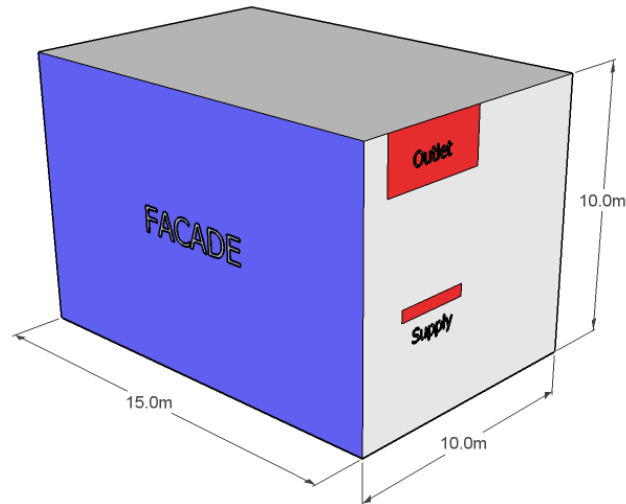


Figure 4.1 Geometry of the reference atrium.

### 4.3 Cases Considered

The following cases were simulated:

- Case S(i) - Summer day solar noon with single glazing.
- Case S(ii) - Summer day solar noon with double glazing.
- Case S(iii) - Summer day solar noon with double glazing and human occupant load.
- Case S(iv)- Summer day solar noon with double glazing with outlet positioned on opposite (west) wall.
- Case S(v) - Summer day solar noon with double glazing with changing facade emissivity values.
- Case W(i) - Winter day solar noon with single glazing.
- Case W(ii) - Winter day solar noon with double glazing.

- Case W(iii) - Winter day solar noon with double glazing and human occupant load.
- Case W(iv)- Winter day solar noon with double glazing and outlet positioned on opposite (west) wall.
- Case W(v) - Winter day solar noon with double glazing and changing facade emissivity values.

Boundary Conditions

The boundary conditions are summarized in Table 4.1 and are explained in detail below. The supply velocity is varied for all cases using values of 1m/s, 0.5m/s, and 0.25m/s.

Case	Glazing Type	Heat Transfer Coefficient (W/m <sup>2</sup> K)	Solar Heat Flux on Floor (W/m <sup>2</sup> )	Solar Heat Flux on North Wall (W/m <sup>2</sup> )	Outdoor Temp. (°C)	Outlet Wall	Supply Temp. (°C)	Façade Emissivity	People Load
S(i)	Single	5	170	n/a	28	East Wall	19	1	No
S(ii)	Double	3	100	n/a	28	East Wall	19	1	No
S(iii)	Double	3	100	n/a	28	East Wall	19	1	Yes
S(iv)	Double	3	100	n/a	28	West Wall	19	1	No
S(v)	Double	3	100	n/a	28	East Wall	19	Varied	No
W(i)	Single	5	70	350	-5	East Wall	19	1	No
W(ii)	Double	3	50	250	-5	East Wall	19	1	No
W(iii)	Double	3	50	250	-5	East Wall	19	1	Yes
W(iv)	Double	3	50	250	-5	West Wall	19	1	No
W(v)	Double	3	50	250	-5	East Wall	19	Varied	No

Table 4.1 Summary of boundary conditions.

### *Facade*

The glazing system used in the facade was altered between single and double glazing. Properties of glazed systems are discussed in Appendix C. The facade surface was modeled as a no slip surface with a heat transfer coefficient and outdoor temperature. The heat transfer coefficient was determined using U-factors for the specified glazing system. ASHRAE's handbook of fundamentals [2001] provides a comprehensive list of glazing system U-factor values for various glazing systems. The single glazing system's U-factor was defined to be 5 W/m<sup>2</sup>K and the double glazing system U-factor was defined to be 3 W/m<sup>2</sup>K.

### *Outdoor Temperature*

Typical outdoor summer and winter temperatures during solar noon observed in Toronto were found to be approximately 28°C and -5°C [Environment Canada, 2011]. These temperatures were applied to the exterior side of the facade for their respective case.

### *Supply*

The HVAC supply provided air at constant temperatures and speed. For the summer case supply air was provided at 19°C. For the winter case supply air was also provided at 19°C at 1 m/s. These temperatures have been derived based on the criteria of satisfying thermal comfort conditions and optimizing energy usage.

### *Return Outlet*

The outlet was treated as an opening with zero relative pressure and a temperature within the range of 24°C to 29°C. Selection of the outlet temperature was dependent on the results of each simulation. To prevent the inflow of fluid entering the atrium space, a bulk temperature near the outlet region had to be determined.

An outlet condition was also tested but did not produce converged and/or accurate results. A sensitivity analysis to determine the effects of outlet ducts was also investigated. The extension of the outlet duct did not produce any significant changes in the flow field but provided continued visualization of the flow exiting through the duct. The duct extension was included in the results.

### *Human Occupant Load*

The thermal heat load of a sedentary person was determined to be 100W with an average surface area of 1.7m<sup>2</sup> [ASHRAE, 2010]. For each occupant load case, a grid of occupants was uniformly spread across the reference atrium in the following formations: 3 by 3, 4 by 4, and 6 by 6. Each person occupied a floor area of 1.7m<sup>2</sup> (approximately equivalent to the average surface area of human body) and was modeled on the floor as an additional heat source on the floor. These cases were simulated to determine the impact of the additional thermal heat load on the conditions in the atrium.

### *Solar Radiation*

The solar radiation heat flux values have been calculated using Hottel's [1976] estimation for clear sky radiation. The calculation of these solar quantities can be seen in Appendix E. Clear sky solar radiation values incident on a horizontal and vertical south facing plane from sunrise to solar noon can be found in Tables 4.2 and 4.3 for typical summer and winter days in Toronto, Canada. These tables include solar radiation values before transmission through the facade, after transmission through a single glazed system, and after transmission through a double glazed system.

The sunlit area for summer and winter days differ due to the movement of the earth. As such, the north wall in the summer case does not receive any sunlight throughout the entire day because of the high solar altitude angle; whereas in winter the solar altitude angle is much lower and the north wall is sunlit. Figure 4.2 and 4.3 are diagrams of the reference atrium for summer and winter days at solar noon displaying the difference in sunlit areas.

Time	No Glazing (W/m <sup>2</sup> )		Single (W/m <sup>2</sup> )		Double (W/m <sup>2</sup> )	
	Horizontal	Vertical	Horizontal	Vertical	Horizontal	Vertical
8:00	459.6	691.7	222.8	335.3	109.5	164.8
8:30	543.0	668.4	259.3	319.2	124.0	152.7
9:00	620.7	631.0	314.0	319.2	163.4	166.2
9:30	691.1	582.4	382.7	322.5	214.1	180.4
10:00	752.6	526.0	434.6	303.8	256.8	179.5
10:30	803.7	465.9	498.1	288.7	307.7	178.3
11:00	843.5	407.6	544.2	263.0	358.8	173.4
11:30	871.1	358.3	577.0	237.4	408.2	167.9
12:00	886.1	327.4	602.3	222.6	453.9	167.7
12:19	888.8	321.4	604.2	218.5	455.2	164.6

Table 4.2 Solar radiation values for summer case (July 1) from sunrise to solar noon. Heat flux values are presented for no glazing, transmitted through single glazed system, and transmitted through double glazed system.

Time	No Glazing (W/m <sup>2</sup> )		Single (W/m <sup>2</sup> )		Double (W/m <sup>2</sup> )	
	Horizontal	Vertical	Horizontal	Vertical	Horizontal	Vertical
8:00	9.1	234.2	6.9	178.6	5.3	135.6
8:30	47.6	240.1	36.7	186.2	27.8	139.2
9:00	92.3	292.5	72.0	230.8	54.0	169.8
9:30	141.5	360.2	112.0	289.1	82.4	208.0
10:00	189.6	423.2	152.1	345.1	111.3	247.0
10:30	232.0	475.1	186.8	389.0	136.0	276.9
11:00	266.2	514.6	214.9	422.5	155.9	299.6
11:30	290.5	541.3	234.9	445.2	170.0	315.0
12:00	303.8	555.5	245.8	457.2	177.8	323.2
12:19	306.4	558.2	248.0	459.5	179.3	324.7

Table 4.3 Clear sky solar radiation values for winter case (January 1) from sunrise to solar noon. Heat flux values are presented for no glazing, transmitted through single glazed system, and transmitted through double glazed system.



Figure 4.2 Sunlit area of the reference atrium for Summer Case at solar noon.



Figure 4.3 Sunlit area of the reference atrium for Winter Case at solar noon.

### *Concrete Floor*

A significant amount of energy is absorbed by the concrete when it is heated by the sun. The high level of thermal mass within concrete causes the solar energy to be absorbed throughout the day and released as temperatures become cooler. The transient effect of thermal mass and solar radiation is studied and presented in section 4.4. Using the methodology described in section 4.4 and the solar radiation values calculated in the above tables, values for the effective heat flux entering the atrium space was determined for a range of times starting from sunset to solar noon. The heat flux value for solar noon was applied as a constant heat flux across the entire sunlit area.

### *Walls*

The North wall in the winter case was also sunlit and an effective heat flux was also calculated using the method described in section 4.4 and applied to the surface. Interior walls, made of gypsum and an air space, have limited thermal mass and do not absorb a significant portion of the incident energy. The non-sunlit walls were treated as no slip adiabatic surfaces.

## 4.4 Thermal Mass of Concrete

### Motivation

This section investigates the thermal mass effect of concrete. As sunlight transmits through the facade and strikes the concrete floor, the concrete gradually increases in temperature over time due to its high thermal mass. Materials with high levels of thermal mass take a longer period of time to reach steady state and can have a lagging effect on the overall energy balance of the system. The transient effect of concrete must be accounted for correctly when simulating atria. While the effect of the thermal mass of the concrete floor could be modeled directly by treating the problem as a transient conjugate heat transfer problem, the variation in the scales between the solid and the fluid can create stiffness which results in numerical challenges and high computational effort. This high computational effort would then make parametric studies less viable. As such, an alternative more computationally effective solution was sought. The following study investigates a method to model the transient effects of concrete by considering a heat transfer problem analogous to conduction in a semi infinite wall.

### Background

During initial simulations of the reference atrium, a constant heat flux was applied to the sunlit atrium floor to simulate the energy from the sun. The floor temperatures were predicted by the code to be in the range of 80°C to 85°C, which is quite excessive and would burn occupants if touched. Previous experimental results for sunlit floors within an atrium suggest floor/wall temperatures are within the range 40°C to 50 °C for

similar clear sky conditions as seen in Toronto Canada (See Yokohama Atrium study). As a result of these unrealistic floor temperatures, it was imperative to investigate the thermal mass effect of the concrete floor. The goal was to develop a boundary condition for the concrete floor that captures the effects of the floor's thermal mass. The effective boundary condition would consider the heat flux from the sun and resulting radiation, convection, and conduction heat losses at the concrete floor.

#### 4.4.1 Numerical Solution Validation

A one-dimensional code that models the effective heat flux entering the interior atrium space was developed and compared against the analytical solution for three boundary conditions: specified temperature, constant heat flux, and surface convection. The analytical solutions for specified temperature, constant heat flux and surface convection are listed in Equations 4.1, 4.2, and 4.3 respectively.

For each of the three boundary conditions, the code was used to compute a temperature profile of the semi-infinite wall made of concrete. The wall was tested under similar boundary conditions experienced by the Reference Atrium for a typical summer day. For Case 1, the initial and environmental temperatures used were 17°C and 22°C. For Case 2, a heat flux of 800 W/m<sup>2</sup> was assumed. For Case 3, the heat transfer coefficient used was 8 W/m<sup>2</sup>K with an environmental temperature of 40°C and an initial temperature of 17°C. The temperature profile for each case was then compared to its known analytical solution. Figure 4.4, 4.5, and 4.6 present the results of the numerical and analytical solutions.

As demonstrated by Figures 4.4, 4.5, and 4.6 the Fortran code used in the analysis of the semi-infinite wall problem produces very accurate results when compared to the analytical solutions for each case. These results indicate that the Fortran code used is correct and can be used as a method to estimate the surface temperature of the concrete.

Case 1: Constant Surface Temperature  $T(0, t) = T_s$

$$T(x, t) - T_s = (T_i - T_s) \operatorname{erf}\left(\frac{x}{\sqrt{4\alpha t}}\right) \quad \text{Equation 4.1}$$

Case 2: Constant Surface Heat Flux  $q_s'' = q_o''$

$$T(x, t) - T_i = \frac{2q_o''(\alpha / \pi)^{1/2}}{k} \exp\left(\frac{-x^2}{4\alpha t}\right) - \frac{q_o'' x}{k} \operatorname{erfc}\left(\frac{x}{\sqrt{4\alpha t}}\right) \quad \text{Equation 4.2}$$

Case 3: Surface Convection  $-k \frac{\partial T}{\partial x} \Big|_{x=0} = h[T_\infty - T(0, t)]$

$$T(x, t) - T_i = \operatorname{erfc}\left(\frac{x}{\sqrt{4\alpha t}}\right) - \left[ \exp\left(\frac{hx}{k} + \frac{h^2 \alpha t}{k^2}\right) \right] \left[ \operatorname{erfc}\left(\frac{x}{\sqrt{4\alpha t}} + \frac{h\sqrt{\alpha t}}{k}\right) \right] \quad \text{Equation 4.3}$$

Property	Value
Density, $\rho$	2400 kg/m <sup>3</sup>
Specific Heat, $C_p$	880 J/KgK
Conductivity, k	1.4 W/mK
Diffusivity, $\alpha$	6.67e-7 m <sup>2</sup> /s

Table 4.4 Properties of Concrete Used in Analysis.

**Temperature Specified Condition Semi Infinite Wall Problem**

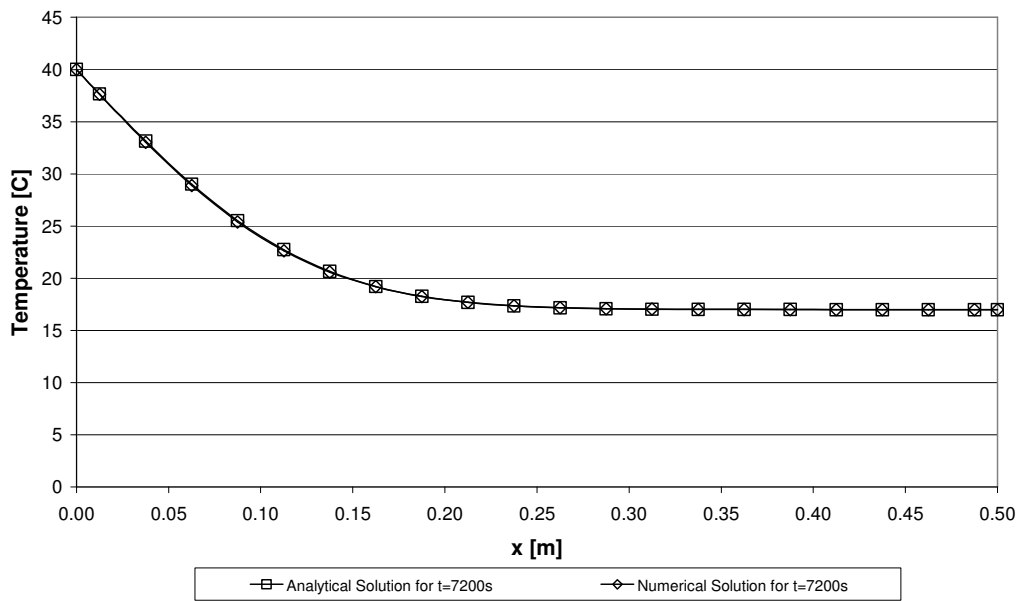


Figure 4.4 Temperature Profile for Temperature Specified Condition at t=7200s

### Constant Heat Flux Condition for Semi Infinite Wall Problem

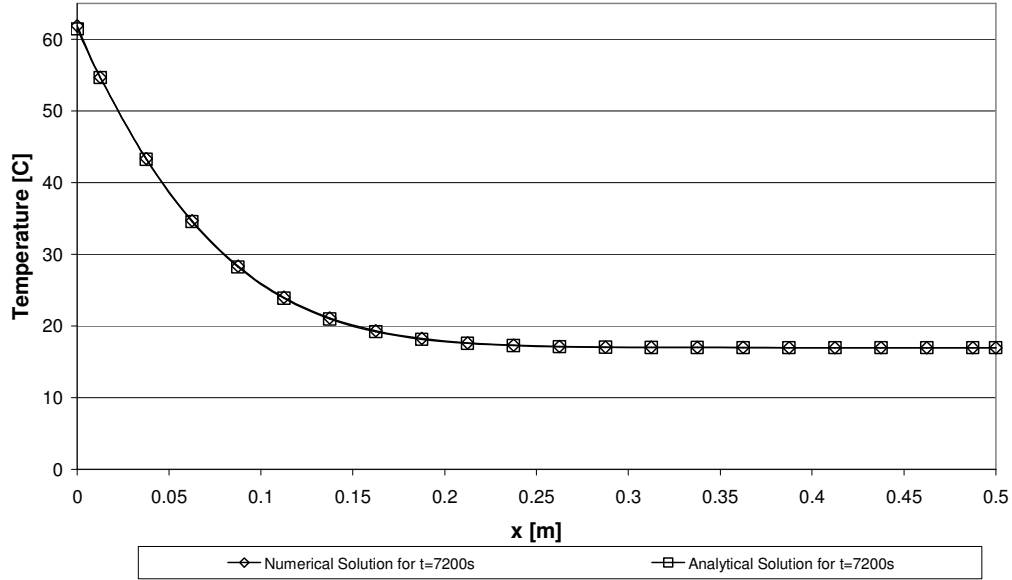


Figure 4.5 Temperature Profile for Constant Heat Flux Condition at t=7200s

### Surface Convection Semi Infinite Wall Problem

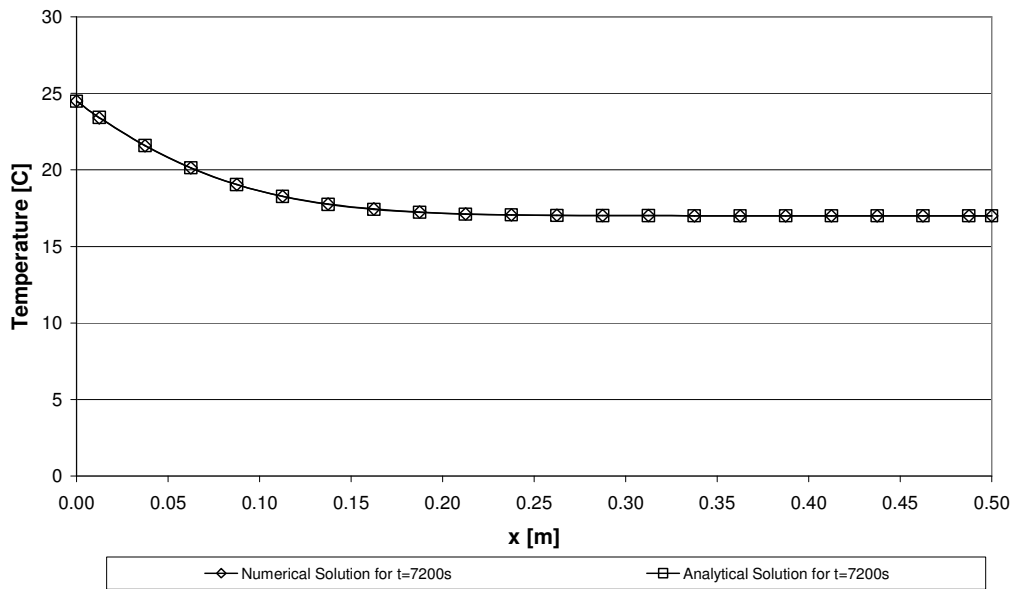


Figure 4.6 Temperature Profile for Surface Convection Condition at t=7200s

#### 4.4.2 Numerical Solution Application

This section investigates the modification of the one-dimensional code so that a realistic application of the solution can be made to the reference atrium. When the solar heat flux is applied to the concrete floor it is divided into three heat transfer processes: convection to the interior space, radiation to the interior space, and conduction through the concrete floor. The Fortran code was therefore modified to include the heat loss due to convection and radiation. Three cases were investigated: 1) convection losses with a constant heat flux, 2) convection and radiation losses with a constant heat flux, and 3) convection and radiation losses using a time varying heat flux.

##### Case A: Convection Losses

This section determines the temperature profile of the concrete floor using a constant heat flux while subject to convection heat losses only. The heat transfer coefficient was varied between  $8\text{W/m}^2\text{K}$  and  $10\text{W/m}^2\text{K}$  with an ambient environmental temperature of  $22^\circ\text{C}$ . The initial temperature of the concrete was varied using temperatures of  $13^\circ\text{C}$ ,  $15^\circ\text{C}$ , and  $17^\circ\text{C}$ . The constant solar heat flux value used in these simulations was  $800\text{W/m}^2$ .

Figure 4.7 provides a simple diagram of the analysis. It demonstrates the solar radiation hitting the concrete floor, the heat is then conducted through the concrete and convected into the surrounding environment. An energy balance was taken into account (Equations 4.4 & 4.5) and was solved for corresponding heat fluxes. Floor temperatures for times 1800s, 3600s, 5400s, 7200s, 9000s, 10800s, 12600s, and 14400s

were calculated. The initial floor temperature and heat transfer coefficients were varied to analyze the solutions sensitivity to these variables. Figure 4.8 provides a plot of the temperature profile with changing initial temperatures. Figure 4.9 provides a temperature profile with changing heat transfer coefficients.

$$q''_{cond} = q''_{solar} - q''_{conv} \quad \text{Equation F.4}$$

$$-k \frac{\partial T}{\partial x} \Big|_{x=0} = q''_{solar} - h(T_{Floor} - T_{\infty}) \quad \text{Equation F.5}$$

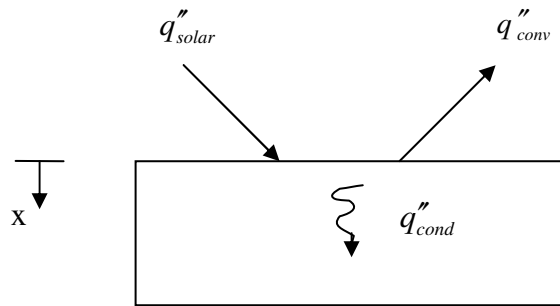


Figure 4.7 Diagram of solar heat flux hitting concrete floor, where a portion of the heat is lost due to surface convection and the remaining is lost through conduction.

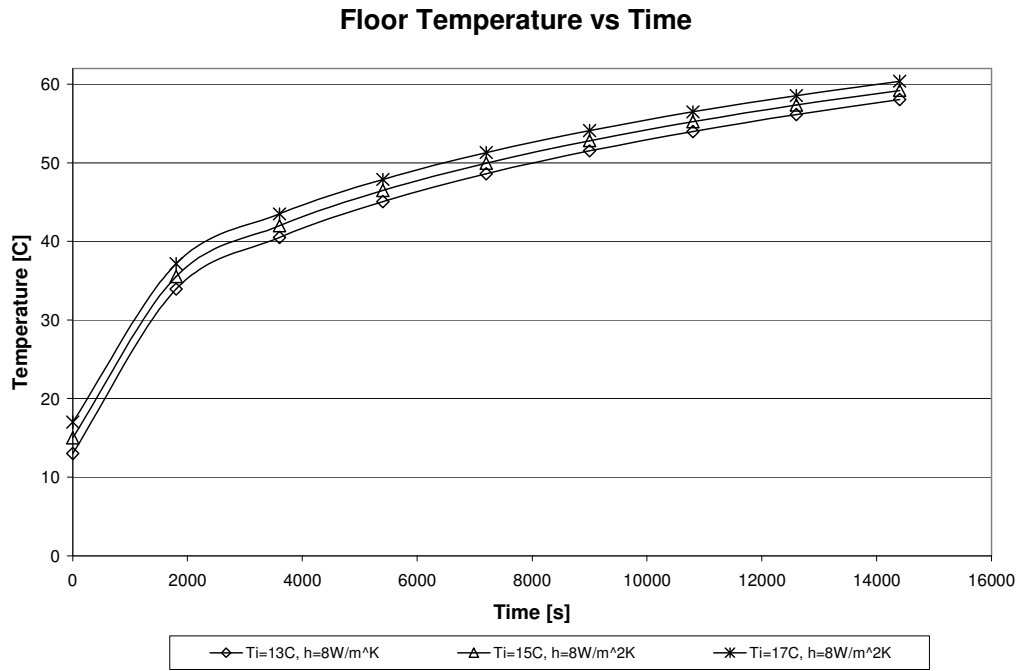


Figure 4.8 Plot of floor temperature versus time with varying initial temperatures.

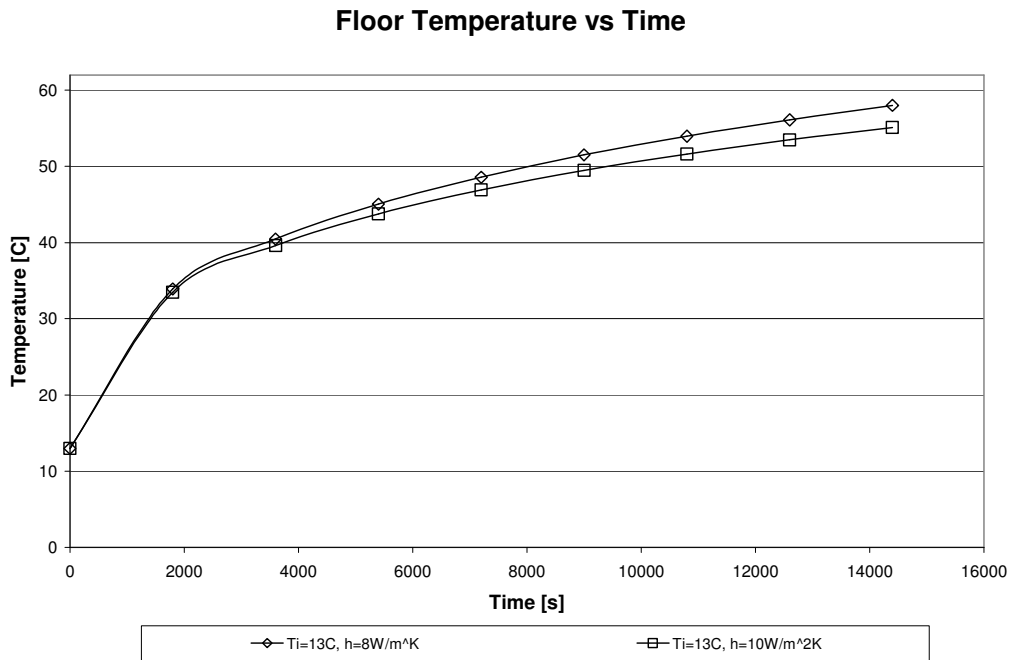


Figure 4.9 Plot of floor temperature versus time with varying heat transfer coefficients.

In Figure 4.8, it can be seen that the concrete warms up to temperatures in the 35 to 38 °C range after 1800s, then increases in temperature in a linear manner. The sensitivity to the initial concrete temperature does not seem to have a profound effect on the overall results, but instead approximately increases each point by the difference in initial temperatures. In Figure 4.9, the sensitivity to heat transfer coefficients doesn't seem to have an a major impact on overall temperatures. Temperatures slightly decrease with larger heat transfer coefficients as time increases.

#### Case B: Convection and Radiation Losses

This section determines the temperature profile of the concrete floor using a constant heat flux while subject to convection and radiation heat losses. Using the same boundary conditions as in Case A, the Fortran code was modified to consider radiation losses. It is assumed that the wall temperatures, not sunlit, within the application of an atrium are close to the ambient room temperature. The emissivities of the walls are close to one.

Figure 4.10 is a diagram of this analysis. It demonstrates the solar heat flux hitting the concrete floor; the heat is then conducted through the concrete, transferred through radiation to the surrounding walls and also convected into the ambient air. An energy balance is taken into to account (Equation 4.6 and 4.7) and is solved for corresponding heat fluxes. Floor temperatures for times 1800s, 3600s, 5400s, 7200s, 9000s, 10800s, 12600s, and 14400s were calculated. The initial floor temperature and

wall temperatures were varied to test the solution's sensitivity to these variables. The results of this analysis can be seen in Figure 4.11 and Figure 4.12.

$$q''_{cond} = q''_{solar} - q''_{conv} - q''_{Rad} \quad \text{Equation 4.6}$$

$$-k \frac{\partial T}{\partial x} \Big|_{x=0} = q''_{solar} - h(T_{Floor} - T_{\infty}) - \epsilon\sigma(T_{FloorOld}^4 - T_{WallAvg}^4)$$

Equation 4.7

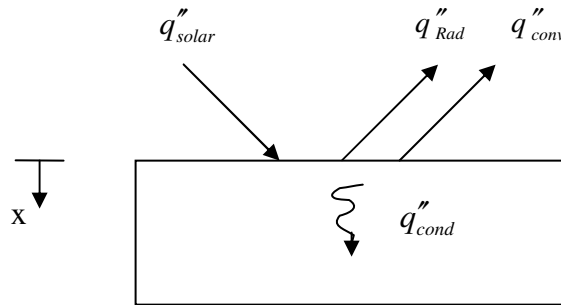


Figure 4.10 Diagram of solar heat flux hitting concrete floor, with some of the heat being lost due to surface convection and the remaining being lost through conduction.

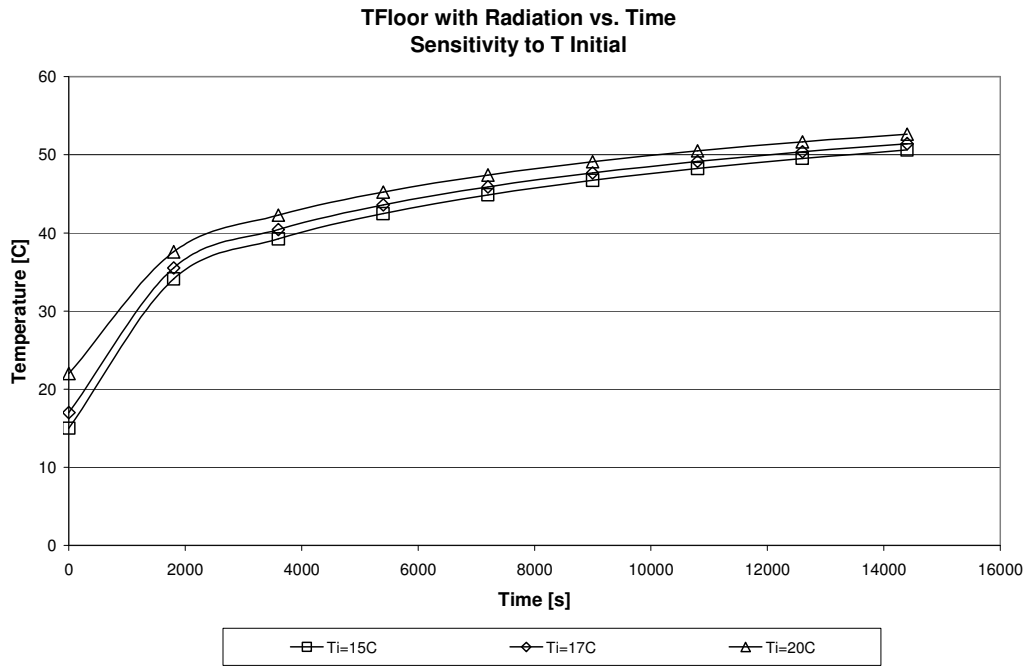


Figure 4.11 Floor temperature versus time with conduction, convection, and radiation losses. Sensitivity to the floor's initial temperature was also investigated.

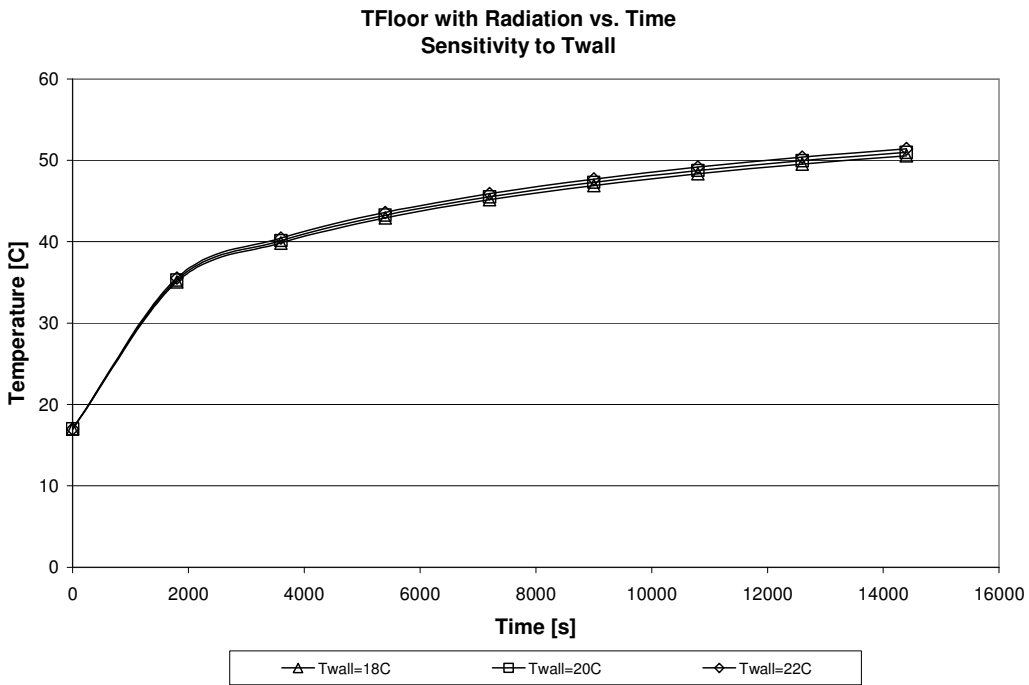


Figure 4.12 Floor temperature with conduction, convection, and radiation heat losses with sensitivity to surrounding wall temperatures.

In Figure 4.11, it can be seen the concrete increases from its initial temperature to a temperature in the 35°C to 38°C range after 1800s and progresses to increases in a linear manner. The effect of the floor's initial temperature is minimal as the changes in temperatures are proportional to the change in initial temperatures. In Figure 4.12, the solution's sensitivity to wall temperatures is insignificant for the range of temperatures tested however there is a slight increase in overall temperatures.

#### Case C: Variable Solar Heat Flux

This section investigates the effect of using a variable solar heat flux with convection and radiation losses. In applying this solution to the reference atrium, the time based movement of the sun and resulting heat flux must also be considered. The solar radiation changes due to the earth's movement with respect to the sun; it is most intense during solar noon when the sun is closest to the earth and least intense during sunset when the sun is furthest from the earth. Utilizing the equations in Appendix E, solar angles and solar radiation quantities can be calculated for the Reference Atrium for July 1. Also accounting for reflectivity of facade surfaces as mentioned in Appendix B, one can derive values for transmitted solar radiation values seen over a period of time from sunrise to solar noon.

Figure 4.13 presents the effective solar radiation on a horizontal surface over time. Table 4.5 presents values of calculated floor temperatures and corresponding heat fluxes. It can be seen that concrete floor temperatures increase from 22°C to 48°C over span of time starting from sunrise to solar noon (i.e. 8:30 to 12:20 on July 1) for Toronto,

Canada). Although these values are approximate, they have been calculated assuming wall temperatures (to account for radiation heat losses), a static heat transfer coefficient (to account for convective heat losses), and clear sky solar radiation. These results are a rough estimate of the temperatures and heat fluxes observed by the Reference Atrium. This process was repeated for a typical winter day in Toronto, Canada. Table 4.6 presents values of the concrete floor for January 1.

The effective energy entering the atrium space is the energy that is reflected and convected from the surface of the sunlit concrete. As such, the heat flux values for the radiation and convected components from sunrise to solar noon were averaged, summed, and applied to the reference atrium's sunlit floor. The averaging of the heat fluxes has been done to account for the changing sunlit area over time. The effective heat fluxes applied to the reference atrium's concrete floor are reported in Table 4.3.

Horizontal Solar Radiation vs. Time (Clear Sky)

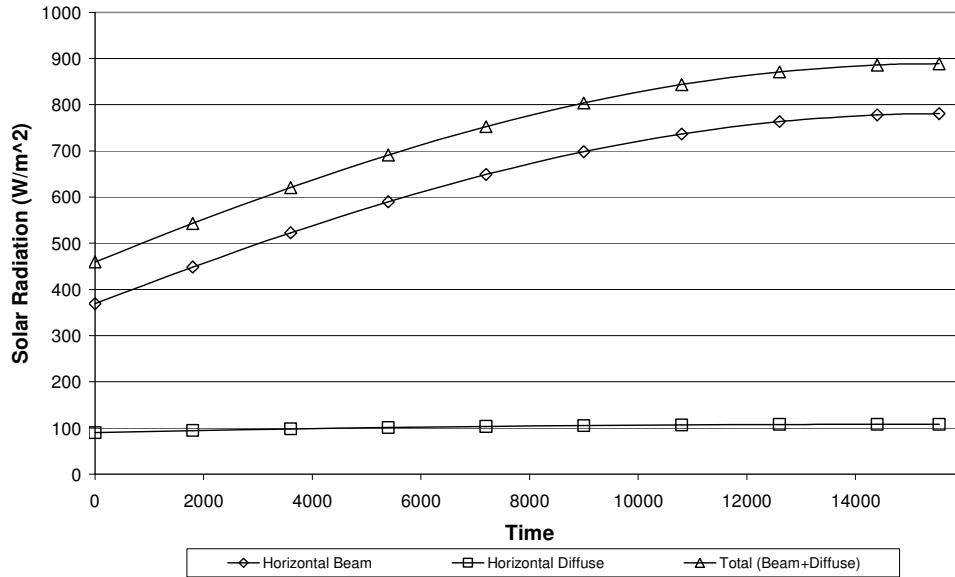


Figure 4.13 Horizontal surface radiation versus time for a clear summer day (July 1) in Toronto, Canada. The horizontal surface radiation is representative of the energy entering the atrium space.

Time (s)	T Floor (°C)	q" solar(t) (W/m <sup>2</sup> )	q"rad (W/m <sup>2</sup> )	q"conv (W/m <sup>2</sup> )	q"cond (W/m <sup>2</sup> )
0	22.0	0.0	0.0	0.0	0.0
1800	30.0	543.7	36.9	48.1	458.7
3600	35.2	619.3	70.5	79.3	469.4
5400	39.4	681.9	98.8	104.3	478.8
7200	42.9	731.6	123.6	125.5	482.5
9000	45.9	768.3	145.3	143.5	479.6
10800	48.4	792.1	163.8	158.3	470.0
12600	50.4	802.9	178.9	170.3	453.7
14400	51.9	800.7	190.5	179.3	431.0

Table 4.5 Values of concrete floor temperature and heat transfer occurring due to radiation, convection, and conduction for a typical summer day in Toronto, Ontario, Canada from sunrise to solar noon. (e.g. July 1)

Time (s)	T Floor (°C)	q"solar(t) (W/m <sup>2</sup> )	q"rad (W/m <sup>2</sup> )	q"conv (W/m <sup>2</sup> )	q"cond (W/m <sup>2</sup> )
0	17.0	0	0	0	0
1800	19.4	47.7	-26.8	-17.3	91.9
3600	21.0	90.7	-17.9	-6.8	115.4
5400	22.6	133.8	-8.5	4.1	138.2
7200	24.3	173.9	1.2	15.3	157.5
9000	25.8	208.0	10.7	25.9	171.3
10800	27.3	232.8	19.4	35.5	177.8
12600	28.4	245.1	26.6	43.3	175.2
14400	29.2	241.9	31.5	48.5	161.9

Table 4.6 Values of concrete floor temperature and heat transfer occurring due to radiation, convection, and conduction for a typical winter day in Toronto, Ontario, Canada from sunrise to solar noon. (e.g. January 1)

## 4.5 Turbulence Model

The k- $\omega$  turbulence model was used during these simulations. The k- $\omega$  turbulence model was selected based on the natural convection study seen in Appendix F and the performance demonstrated in the previous atria analyses in Chapter 3.

## 4.6 Mesh and Grid Independence

Three meshes were tested for grid independence: 100x75x75 (562,500 nodes) 150x100x100 (1,500,000 nodes), and 200x150x150 (4,500,000 nodes). Grid independence was tested using the summer case with single glazing comparing velocity along a line located in the middle of the reference atrium. The predicted velocity values differed marginally under the 150x100x100 and 200x150x150 meshes, while the 100x75x75 demonstrated greater deviation in velocity values compared to the remaining meshes. The 150x100x100 mesh was chosen for the remainder of simulations and can be seen in Figure 4.14. The grid independence study is illustrated in Figure 4.15.

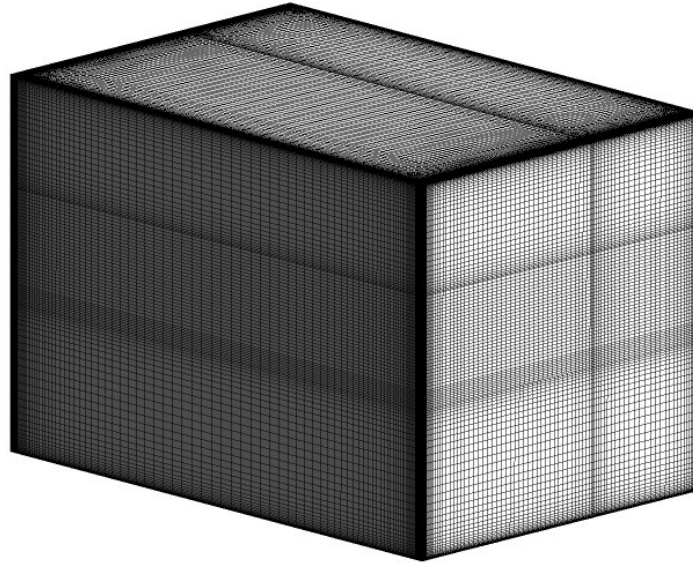


Figure 4.14 The 150x100x100 mesh which was used for all case simulations.

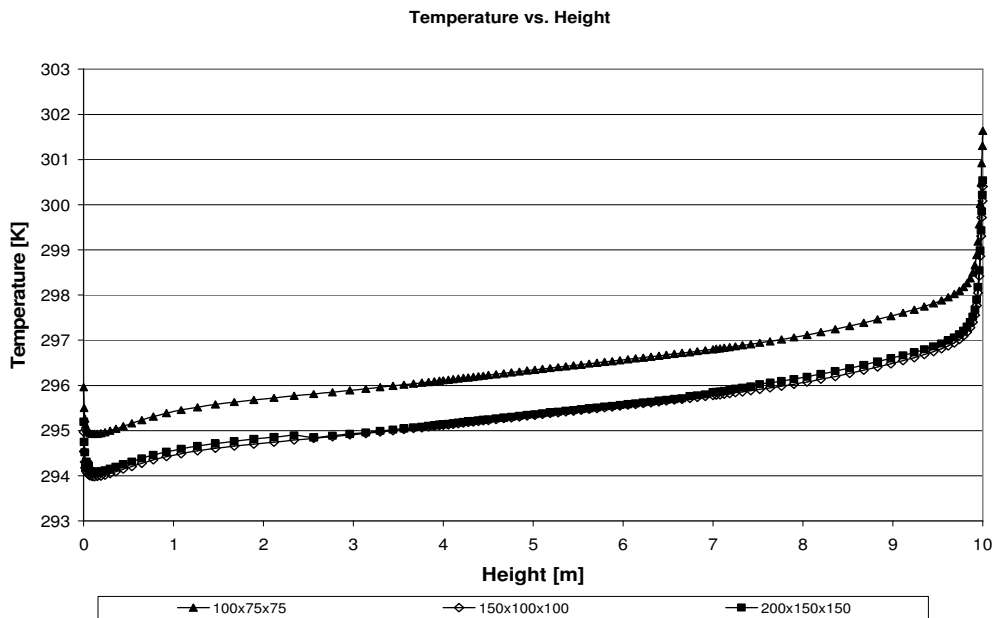


Figure 4.15 Grid independence study for velocities measured along a line at the centre of the atrium for summer case with single glazing with supply set to 19°C at 1m/s and heat flux on floor set to 170 W/m<sup>2</sup>.

## 4.7 Results

Figures 4.16, 4.17, 4.18, and 4.19 are the measurement planes and lines that have been used to demonstrate the range of temperatures seen within the base cases which are 1) summer case with double glazing and supply set to 19C at 0.5m/s and 2) winter case with double glazing and supply set to 19C at 0.5m/s. Figure 4.20 and 4.28 provide the results for the base cases for summer and winter respectively. The remaining cases have been reported using only the vertical plane parallel to the facade intersecting the midpoint of the supply inlet (i.e. vertical plane parallel to the facade 3.5m away). Summer cases are reported in Figures 4.21 to 4.28 and winter cases in Figures 4.30 to 4.37. The summer and winter cases for occupant load of 3by3 and 4by4 are reported in Appendix D. These particular cases did not provide any significant results and were reported in the appendix as a reference.

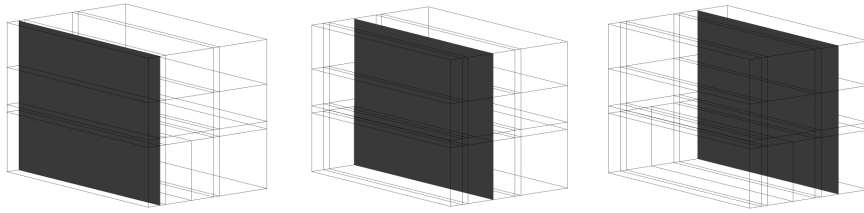


Figure 4.16 Vertical planes parallel to the facade at locations 1m, 3.5m, and 7.5m away from the facade.

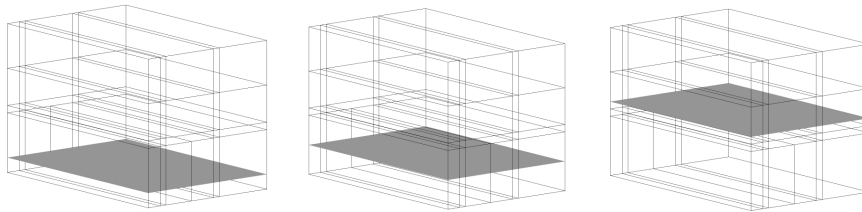


Figure 4.17 Horizontal planes at heights 1m from the floor, 2m from the floor, and 5m from the floor.

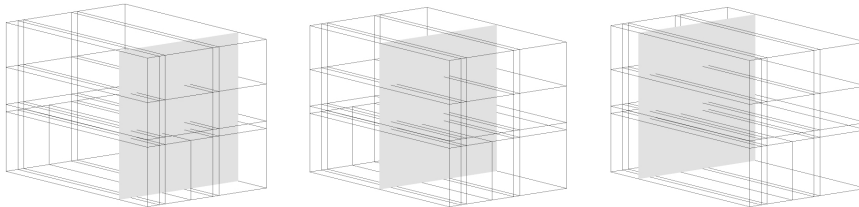


Figure 4.18 Vertical planes perpendicular to the facade at locations 3m, 7.5m, and 12m away from the east wall.

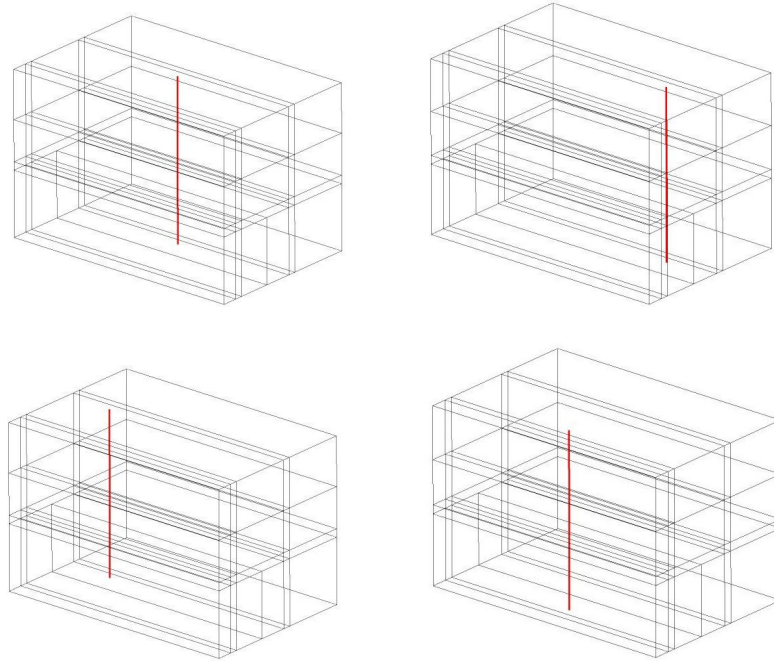


Figure 4.19 Location of lines used to measure temperatures for the base cases.

**(S) - Summer Cases**

*Baseline Case for Summer*

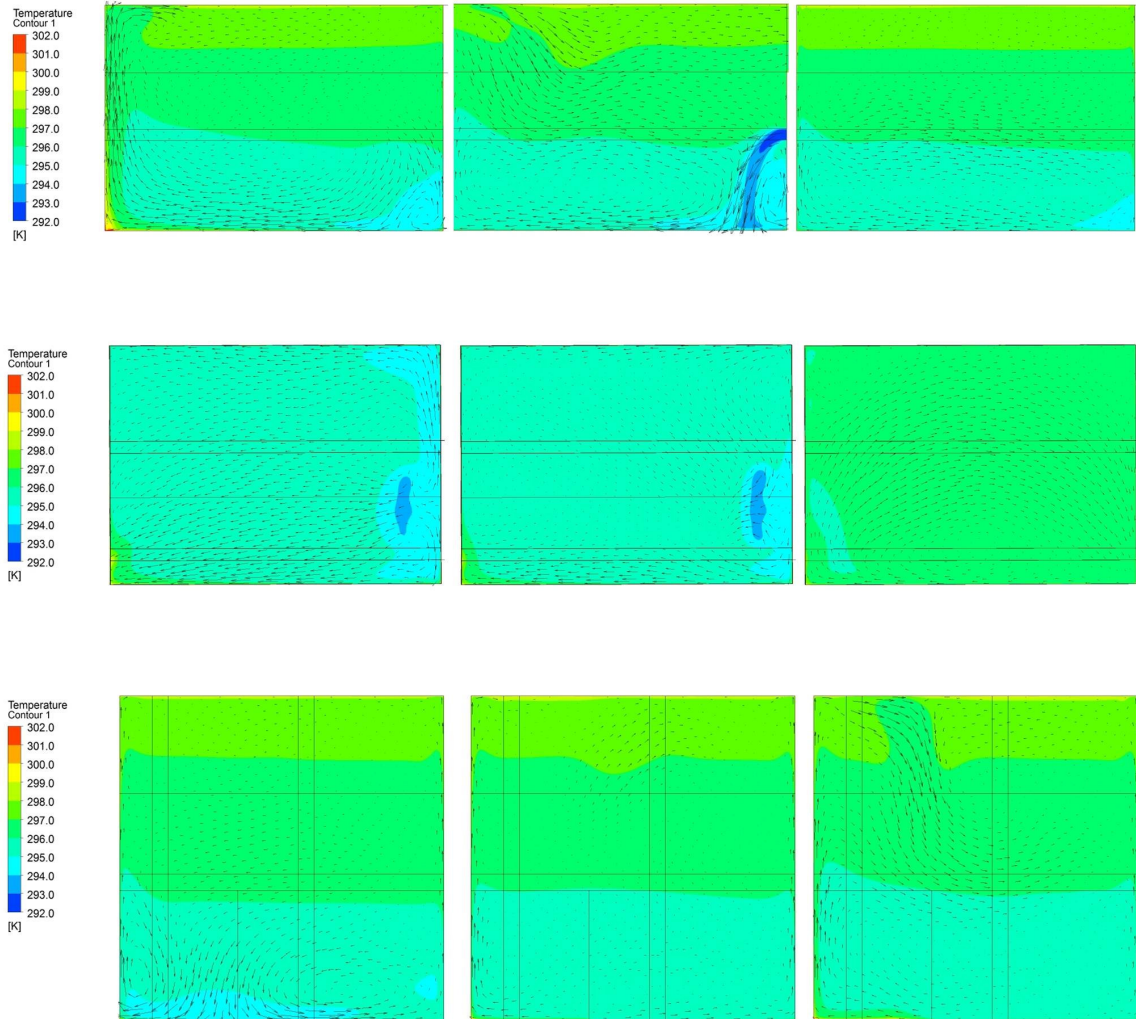


Figure 4.20 Temperature contour and velocity distribution plots for reference atrium with a double glazed facade on a typical summer day with supply set to 19°C at 0.5m/s. (First row) Vertical planes parallel to the facade at locations 1m, 3.5m, and 7.5m away from the facade. (Second Row) Horizontal planes at heights 1m from the floor, 2m from the floor, and 5m from the floor. (Third Row) Vertical planes perpendicular to the facade at locations 3m, 7.5m, and 12m away from the east wall.

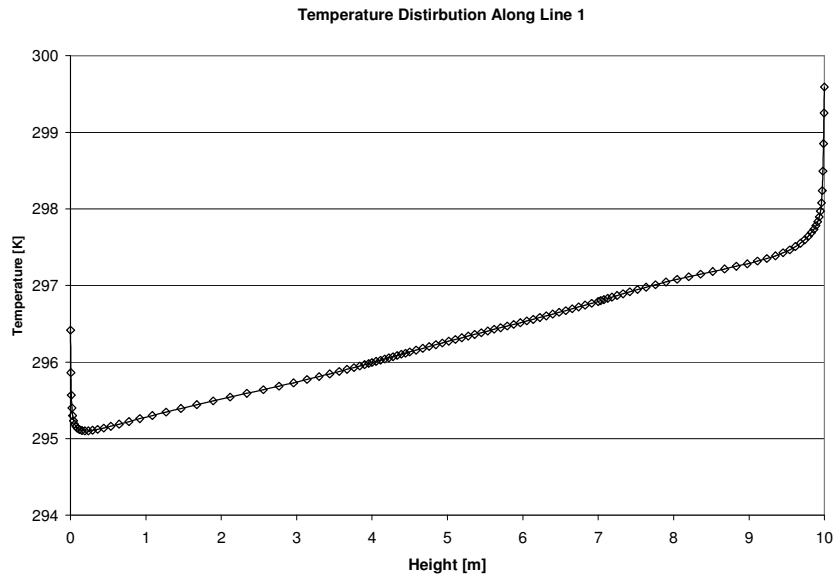


Figure 4.21 Temperature distribution for summer base case at Line 1.

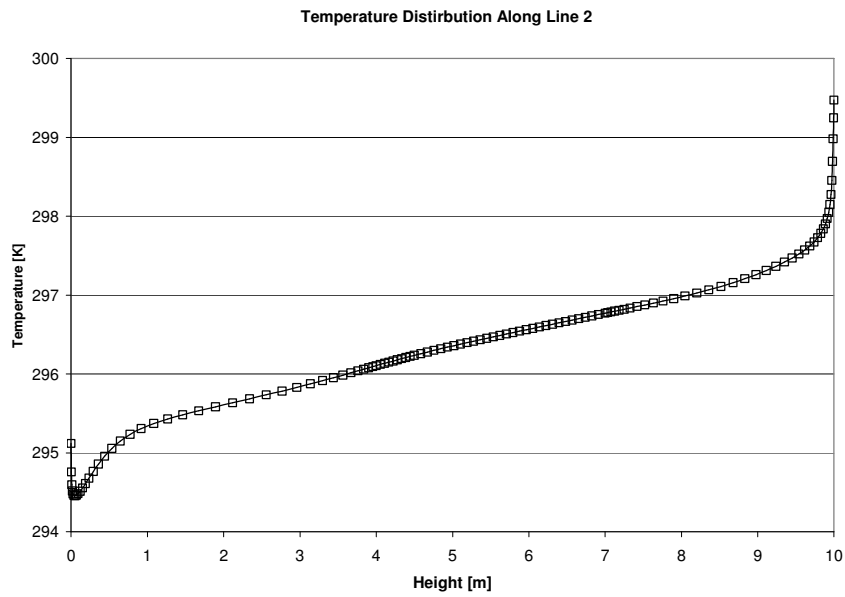


Figure 4.22 Temperature distribution for summer base case at Line 2.

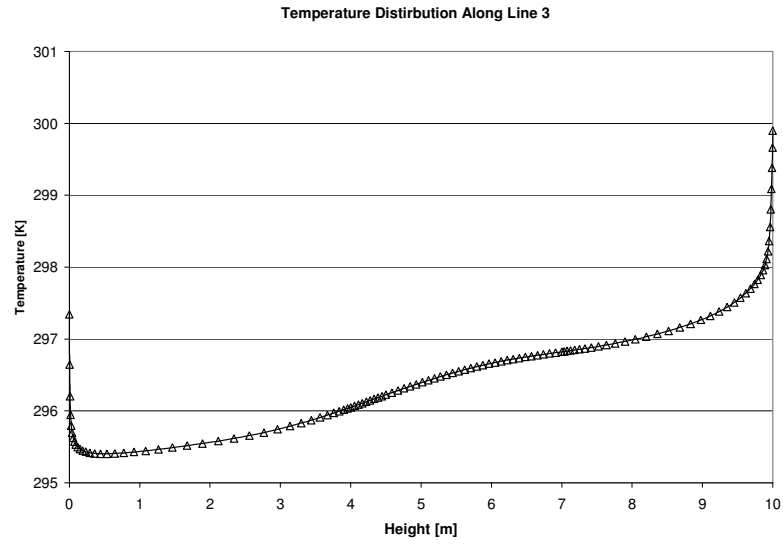


Figure 4.23 Temperature distribution for summer base case at Line 3.

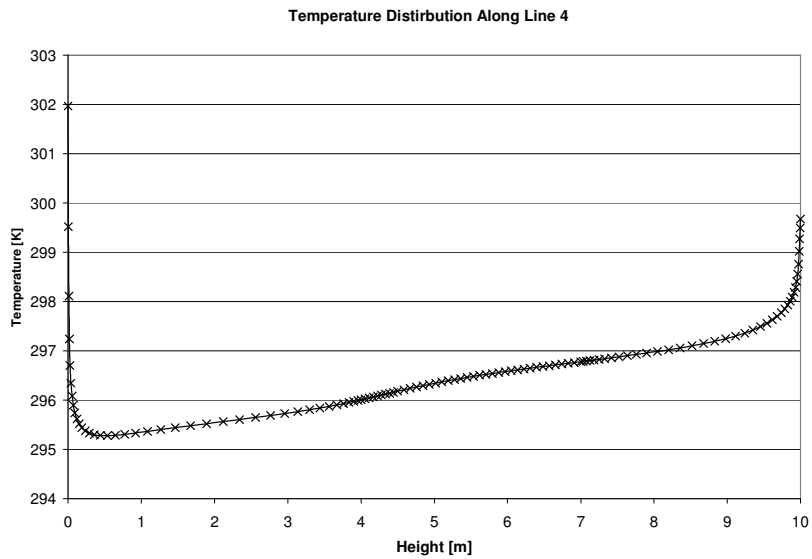


Figure 4.24 Temperature distribution for summer base case at Line 4

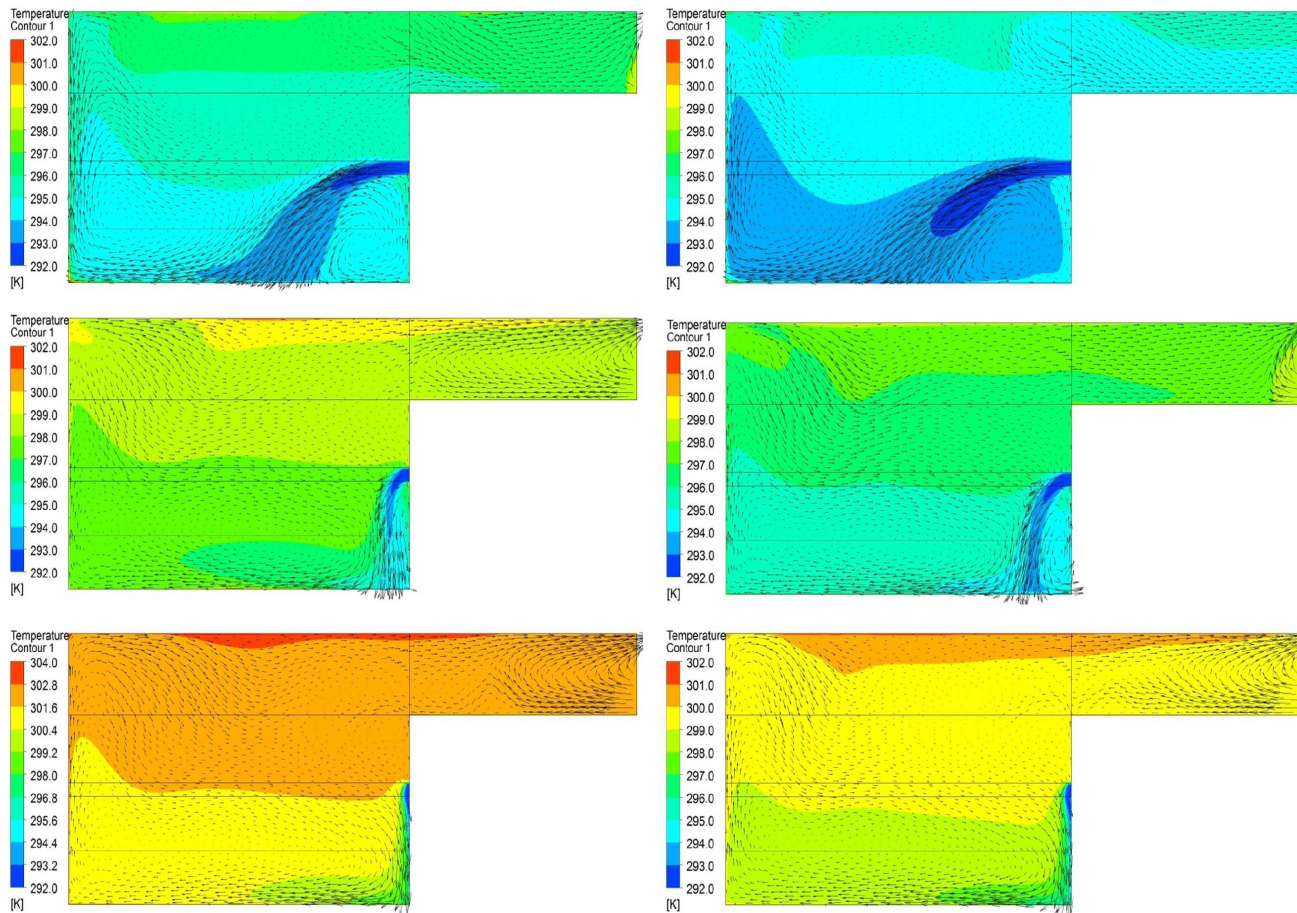


Figure 4.25 Temperature contour and velocity distribution plots for reference atrium at plane parallel to the facade intersecting the midpoint of the supply for summer case with (Left) single glazing and (Right) double glazing with: supply set to 19°C and outside temperature set to 28°C. (Top) Supply set to 1m/s. (Middle) Supply set to 0.5m/s. (Bottom) Supply set to 0.25m/s.

Case	Location	1m/s	0.5m/s	0.25 m/s
		Energy [W]	Energy [W]	Energy [W]
S(i) Single Glazed	Supply	-14750.0	-7452.0	-3828.0
	Outlet	4759.0	-1375.0	-3346.0
	Facade	729.8	-470.1	-2053.0
	Floor	9282.0	9282.0	9282.0
S(ii) Double Glazed	Supply	-14720.0	-7416.0	-3783.0
	Outlet	7482.0	1113.0	-1317.0
	Facade	1751.0	851.0	-382.5
	Floor	5460.0	5460.0	5460.0

Table 4.7 Energy values comparing S(i) single glazed and S(ii) double glazed cases.

Case	Location	Avg Temp [K]	Max Temp [K]	Stratification [K]	Avg. Temp at Floor [K]
S(i) 1m/s	Entire Atrium	296.1	321.2	0.9	295.8
	Occupied Space	296.5	321.2	-0.5	295.8
S(i) 0.5m/s	Entire Atrium	298.4	320.0	2.1	297.2
	Occupied Space	297.8	320.0	0.1	297.2
S(i) 0.25m/s	Entire Atrium	302.0	323.5	1.6	301.0
	Occupied Space	301.6	323.5	0.2	301.0
S(ii) 1m/s	Entire Atrium	294.9	310.9	0.7	294.6
	Occupied Space	295.1	310.9	-0.3	294.6
S(ii) 0.5m/s	Entire Atrium	297.0	312.3	1.8	295.8
	Occupied Space	296.3	312.3	-0.1	295.8
S(ii) 0.25m/s	Entire Atrium	299.7	314.4	1.6	298.6
	Occupied Space	299.1	314.4	0.2	298.6

Table 4.8 Interior temperature results comparing S(i) single glazed and S(ii) double glazed cases.

<b>Case</b>	<b>Avg. Floor Temp [K]</b>	<b>Avg. Wall Temp [K]</b>	<b>Avg. Façade Temp. [K]</b>
S(i) 1m/s	303.7	310.0	299.4
S(i) 0.5m/s	303.9	300.4	301.0
S(i) 0.25m/s	307.0	303.6	303.8
S(ii) 1m/s	300.0	296.5	297.7
S(ii) 0.5m/s	301.1	298.4	299.1
S(ii) 0.25m/s	302.9	300.8	301.2

Table 4.9 Surface temperature results comparing S(i) single glazed and S(ii) double glazed cases.

<b>Case</b>	<b>Max Velocity [m/s]</b>	<b>Avg Velocity [m/s]</b>
S(i) 1m/s	1.00	0.20
S(i) 0.5m/s	1.03	0.21
S(i) 0.25m/s	1.10	0.20
S(ii) 1m/s	1.00	0.18
S(ii) 0.5m/s	0.80	0.17
S(ii) 0.25m/s	0.80	0.18

Table 4.10 Velocity results comparing S(i) single glazed and S(ii) double glazed cases.

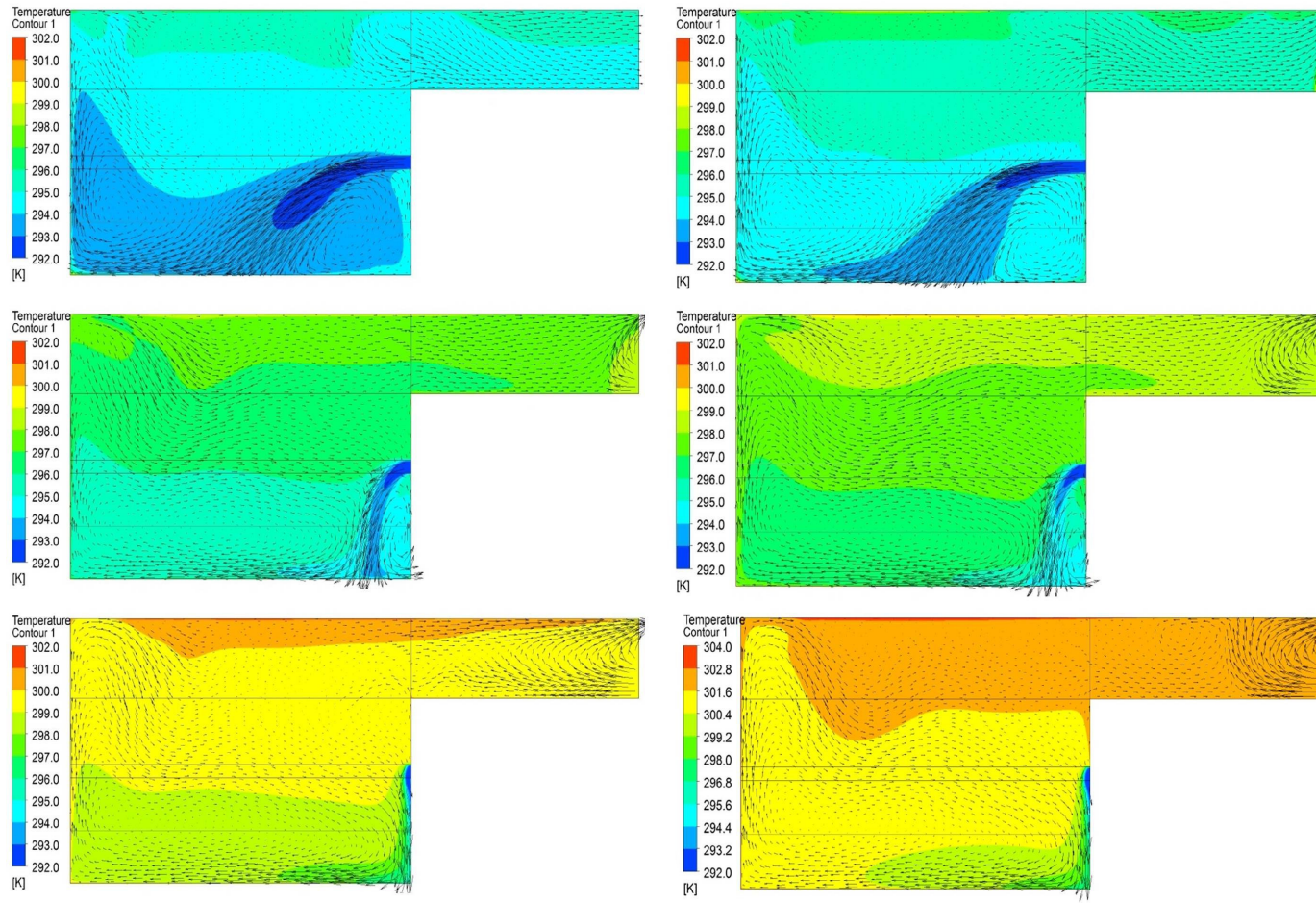


Figure 4.26 Temperature contour and velocity distribution plots for reference atrium at plane parallel to the facade intersecting the midpoint of the supply for summer case with (Left) double glazing without occupant load (Right) double glazing with occupant load 6by6 with: supply set to 19°C, heat flux on floor 100W/m<sup>2</sup>, and outside temperature set to 28°C. (Top) Supply set to 1m/s. (Middle) Supply set to 0.5m/s. (Bottom) Supply set to 0.25m/s.

Case	Location	1m/s	0.5m/s	0.25 m/s
		Energy [W]	Energy [W]	Energy [W]
S(ii) Double Glazed	Supply	-14720.0	-7416.0	-3783.0
	Outlet	7482.0	1113.0	-1317.0
	Facade	1751.0	851.0	-382.5
	Floor	5460.0	5460.0	5460.0
S(iii)c Double Glazed with 6by6	Supply	-14738.6	-7442.1	-3819.1
	Outlet	5728.1	-651.1	-2685.1
	Facade	1131.1	-280	-1854.2
	Floor	8378.3	8377.5	8378.1

Table 4.11 Energy values comparing S(ii)double glazed and S(iii)c double glazed with occupant load 6by6 cases.

Case	Location	Avg Temp [K]	Max Temp [K]	Stratification [K]	Avg. Temp at Floor [K]
S(ii) 1m/s	Entire Atrium	294.9	310.9	0.7	294.6
	Occupied Space	295.1	310.9	-0.3	294.6
S(ii) 0.5m/s	Entire Atrium	297.0	312.3	1.8	295.8
	Occupied Space	296.3	312.3	-0.1	295.8
S(ii) 0.25m/s	Entire Atrium	299.7	314.4	1.6	298.6
	Occupied Space	299.1	314.4	0.2	298.6
S(iii)c 1m/s	Entire Atrium	295.7	312.7	0.7	295.5
	Occupied Space	296.0	312.7	-0.4	295.5
S(iii)c 0.5m/s	Entire Atrium	298.0	316.1	1.8	296.8
	Occupied Space	297.4	316.1	0.0	296.8
S(iii)c 0.25m/s	Entire Atrium	301.8	318.6	1.7	300.6
	Occupied Space	301.1	318.6	0.2	300.6

Table 4.12 Interior temperature results comparing S(ii)double glazed and S(iii)c double glazed with occupant load 6by6 cases.

<b>Case</b>	<b>Avg. Floor Temp [K]</b>	<b>Avg. Wall Temp [K]</b>	<b>Avg. Façade Temp. [K]</b>
S(ii) 1m/s	300.0	296.5	297.7
S(ii) 0.5m/s	301.1	298.4	299.1
S(ii) 0.25m/s	302.9	300.8	301.2
S(iii)c 1m/s	301.3	297.6	298.6
S(iii)c 0.5m/s	302.2	299.7	300.2
S(iii)c 0.25m/s	305.1	303.1	302.9

Table 4.13 Surface temperature results comparing S(ii)double glazed and S(iii)c double glazed with occupant load 6by6 cases.

<b>Case</b>	<b>Max Velocity [m/s]</b>	<b>Avg Velocity [m/s]</b>
S(ii) 1m/s	1.00	0.18
S(ii) 0.5m/s	0.80	0.17
S(ii) 0.25m/s	0.80	0.18
S(iii)c 1m/s	1.07	0.20
S(iii)c 0.5m/s	0.78	0.20
S(iii)c 0.25m/s	1.12	0.20

Table 4.14 Velocity results comparing S(ii)double glazed and S(iii)c double glazed with occupant load 6by6 cases.

*Case S(iv) - Summer day using double glazed system with changing outlets*

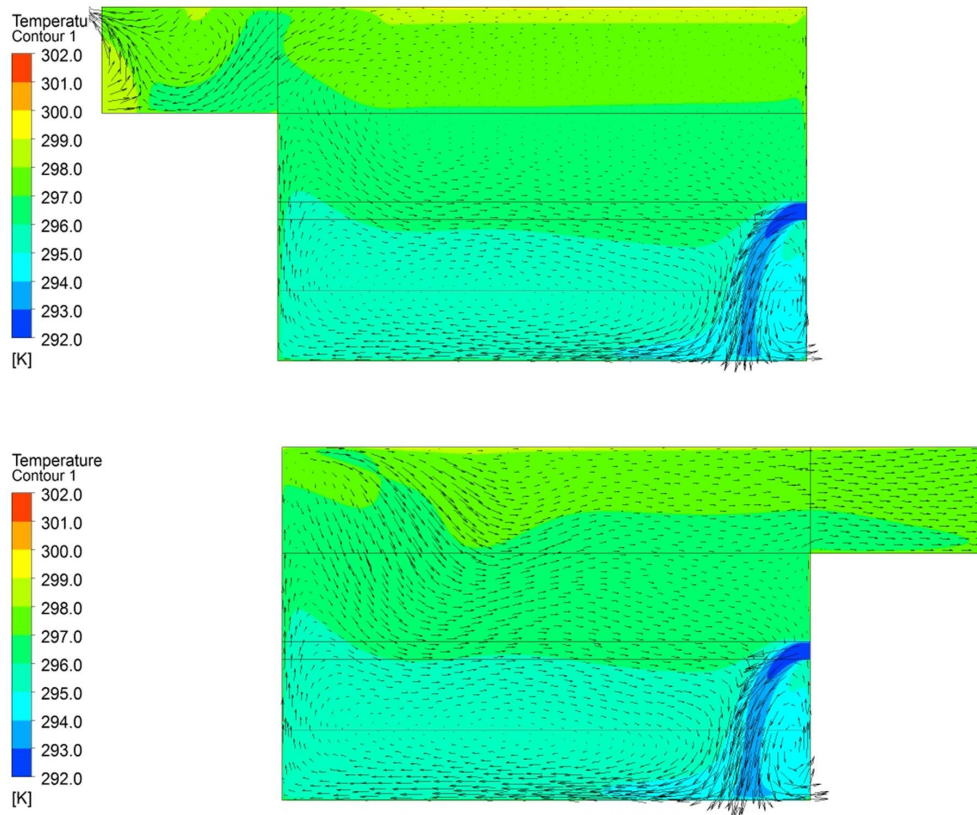


Figure 4.27 Temperature contour and velocity distribution plots for reference atrium at plane parallel to the facade intersecting the midpoint of the supply for summer case with double glazing with: supply set to 19°C at 0.5m/s, heat flux on floor 100W/m<sup>2</sup>, and outside temperature set to 28°C. (Top) Outlet placed on west wall. (Bottom) Outlet placed on east wall.

	<b>S(iv) West Wall Outlet</b>	<b>S(ii) East Wall Outlet</b>
<b>Location</b>	<b>Energy [W]</b>	<b>Energy [W]</b>
Supply	-7420.6	-7416.0
Outlet	1107.0	1113.0
Facade	842.0	851.0
Floor	5460.0	5460.0

Table 4.15 Energy quantities comparing summer cases S(iv) and S(ii).

<b>Case</b>	<b>Location</b>	<b>Avg. Temp [K]</b>	<b>Max Temp [K]</b>	<b>Stratification [K]</b>	<b>Avg. Temp Near Floor [K]</b>
S(iv) West Wall Outlet	Entire Atrium	297.4	312.5	2.4	296.0
	Occupied Space	296.5	312.5	-0.1	296.0
S(ii) East Wall Outlet	Entire Atrium	297.0	312.3	1.8	295.8
	Occupied Space	296.3	312.3	-0.1	295.8

Table 4.16 Interior temperatures comparing summer cases S(iv) and S(ii).

<b>Case</b>	<b>Avg. Floor Temp [K]</b>	<b>Avg. Wall Temp [K]</b>	<b>Avg. Façade Temp. [K]</b>
S(iv) West Wall Outlet	301.3	298.8	299.4
S(ii) East Wall Outlet	301.8	298.4	298.8

Table 4.17 Average and maximum wall temperatures comparing summer cases S(iv) and S(ii).

<b>Case</b>	<b>Max Velocity [m/s]</b>	<b>Avg. Velocity [m/s]</b>
S(iv) West Wall Outlet	0.90	0.18
S(ii) East Wall Outlet	0.80	0.17

Table 4.18 Average and maximum velocities comparing summer cases S(iv) and S(ii).

*Case S(v) - Summer day using double glazed system with changing facade emissivity*

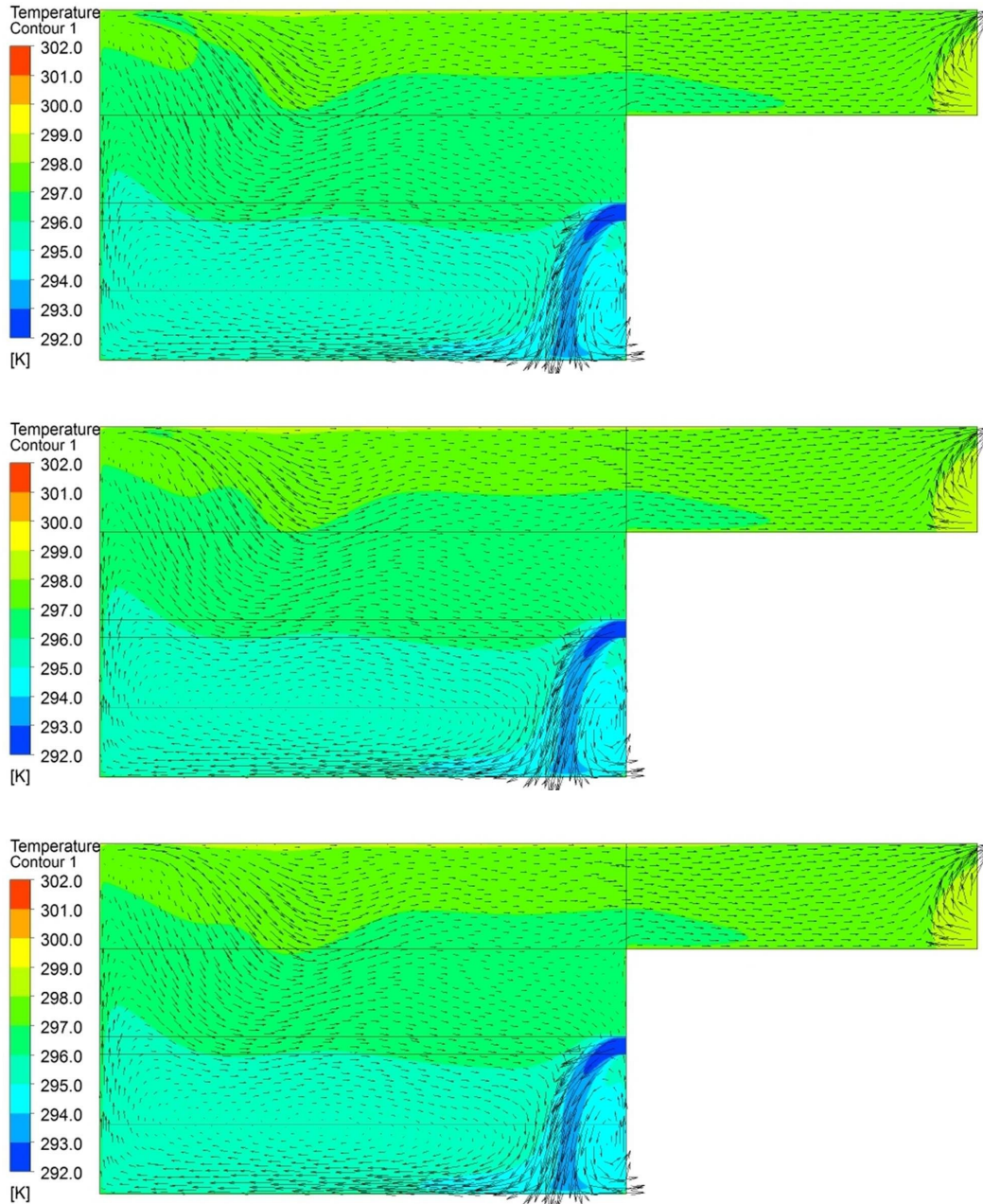


Figure 4.28 Temperature contour and velocity distribution plots for reference atrium at plane parallel to the facade intersecting the midpoint of the supply for summer case with double glazing with: supply set to 19°C at 0.5m/s, heat flux on floor 100W/m<sup>2</sup>, and outside temperature set to 28°C. (Top) Emissivity set to 1. (Middle) Emissivity set to 0.5. (Bottom) Emissivity set to 0.25.

Location	S(ii) $\epsilon=1$	S(v) $\epsilon=0.5$	S(v) $\epsilon=0.25$
	Energy [W]	Energy [W]	Energy [W]
Supply	-7416.0	-7416.9	-7417.8
Outlet	1113.0	1096.5	1074.1
Facade	851.0	913.9	970.3
Floor	5460.0	5460.0	5460.0

Table 4.19 Energy quantities for summer case S(v).

Case	Location	Avg. Temp [K]	Max Temp [K]	Stratification [K]	Avg. Temp Near Floor [K]
S(ii) $\epsilon=1$	Entire Atrium	297.0	312.3	1.8	295.8
	Occupied Space	296.3	312.3	-0.1	295.8
S(v) $\epsilon=0.5$	Entire Atrium	297.0	312.5	1.8	295.9
	Occupied Space	296.4	312.5	-0.1	295.9
S(v) $\epsilon=0.25$	Entire Atrium	297.0	312.8	1.8	295.9
	Occupied Space	296.4	312.8	-0.1	295.9

Table 4.20 Interior temperatures for summer case S(v).

Case	Avg. Floor Temp [K]	Avg. Wall Temp [K]	Avg. Façade Temp. [K]
S(ii) $\epsilon=1$	301.8	298.4	298.8
S(v) $\epsilon=0.5$	301.2	298.5	299.1
S(v) $\epsilon=0.25$	301.3	298.6	299.3

Table 4.21 Average and maximum wall temperatures for summer case S(v).

Case	Max Velocity [m/s]	Avg. Velocity [m/s]
S(ii) $\epsilon=1$	0.80	0.17
S(v) $\epsilon=0.5$	0.80	0.18
S(v) $\epsilon=0.25$	0.80	0.18

Table 4.22 Average and maximum velocities for summer case S(v).

## (W) - Winter Cases

### *Baseline Case for Winter*

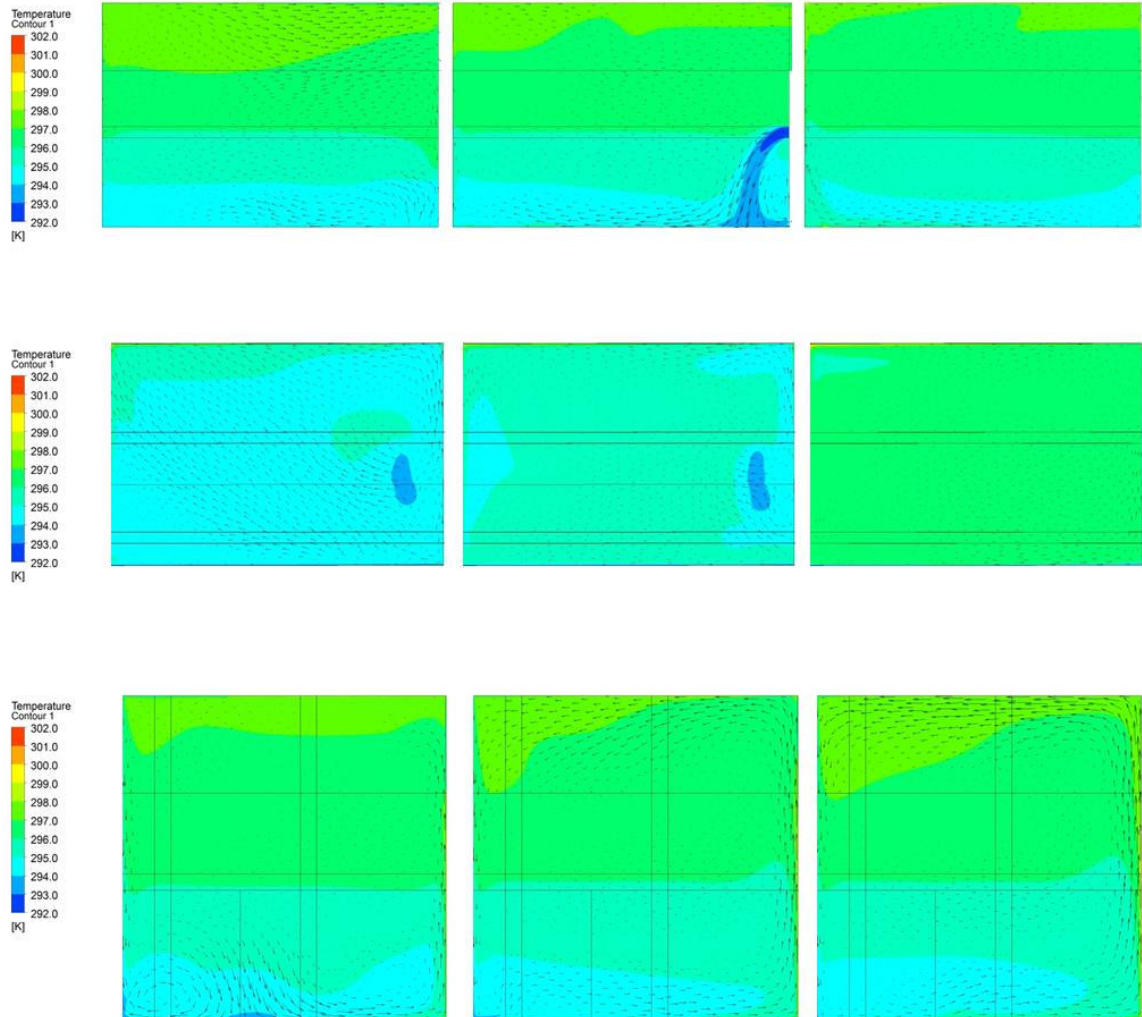


Figure 4.29 Temperature contour and velocity distribution plots for reference atrium with a double glazed facade on a typical winter day with supply set to 19°C at 0.5m/s, heat flux on floor 50W/m<sup>2</sup>, heat flux on north wall 300W/m<sup>2</sup>, and outside temperature set to -5°C. (First row) Vertical planes parallel to the facade at locations 1m, 3.5m, and 7.5m away from the facade. (Second Row) Horizontal planes at heights 1m from the floor, 2m from the floor, and 5m from the floor. (Third Row) Vertical planes perpendicular to the facade at locations 3m, 7.5m, and 12m away from the HVAC openings.

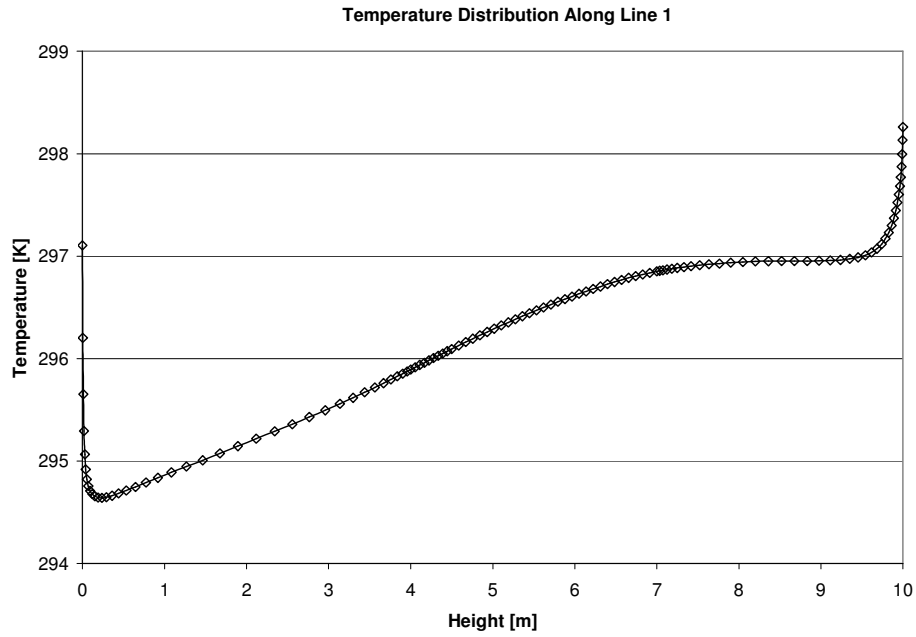


Figure 4.30 Temperature distribution along Line 1 for winter base case.

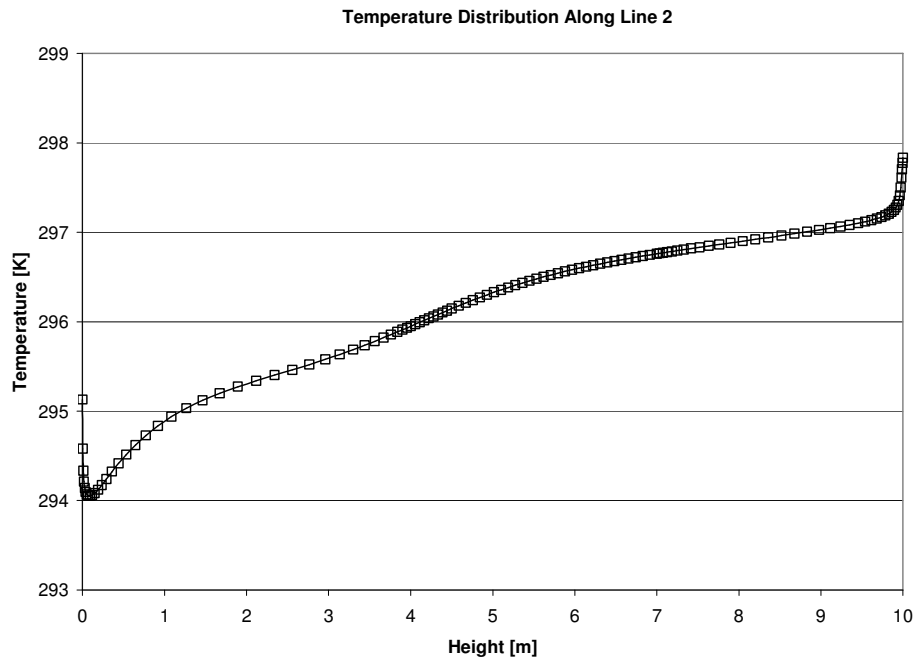


Figure 4.31 Temperature distribution along Line 2 for winter base case.

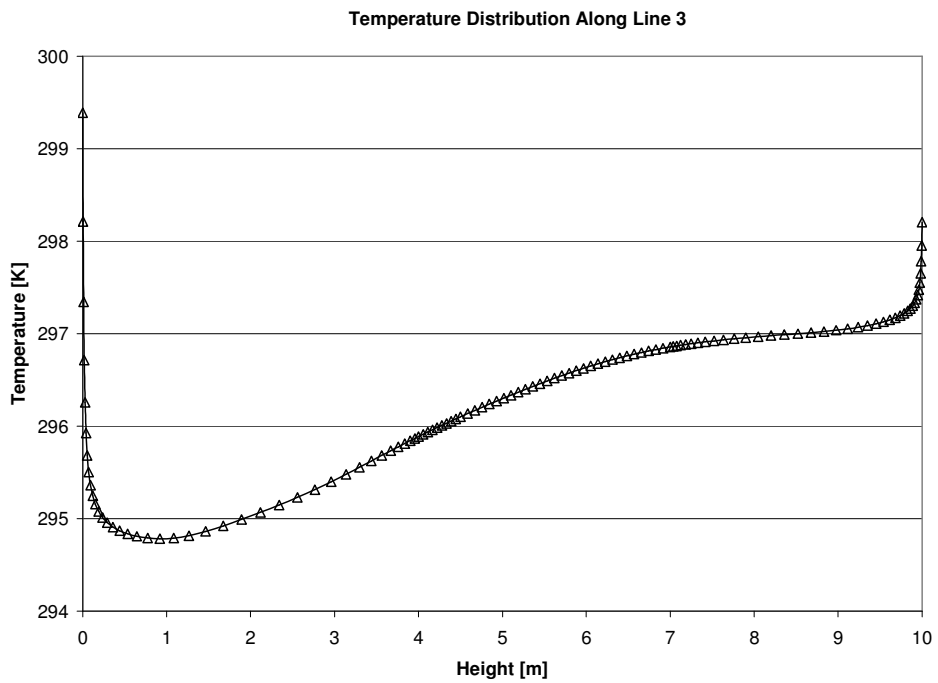


Figure 4.32 Temperature distribution along Line 3 for winter base case.

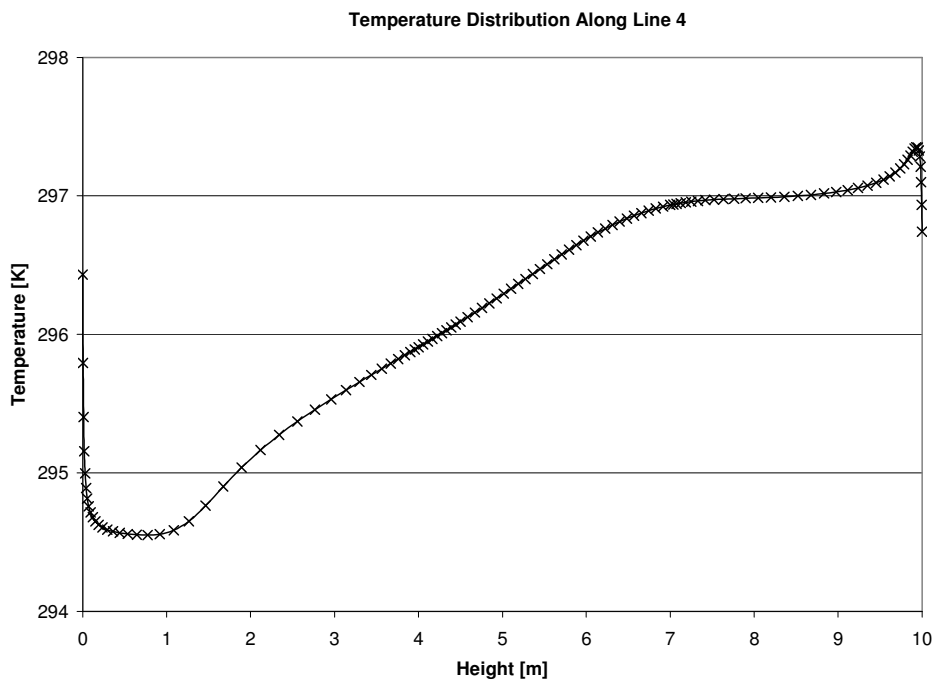


Figure 4.33 Temperature distribution along Line 4 for winter base case.

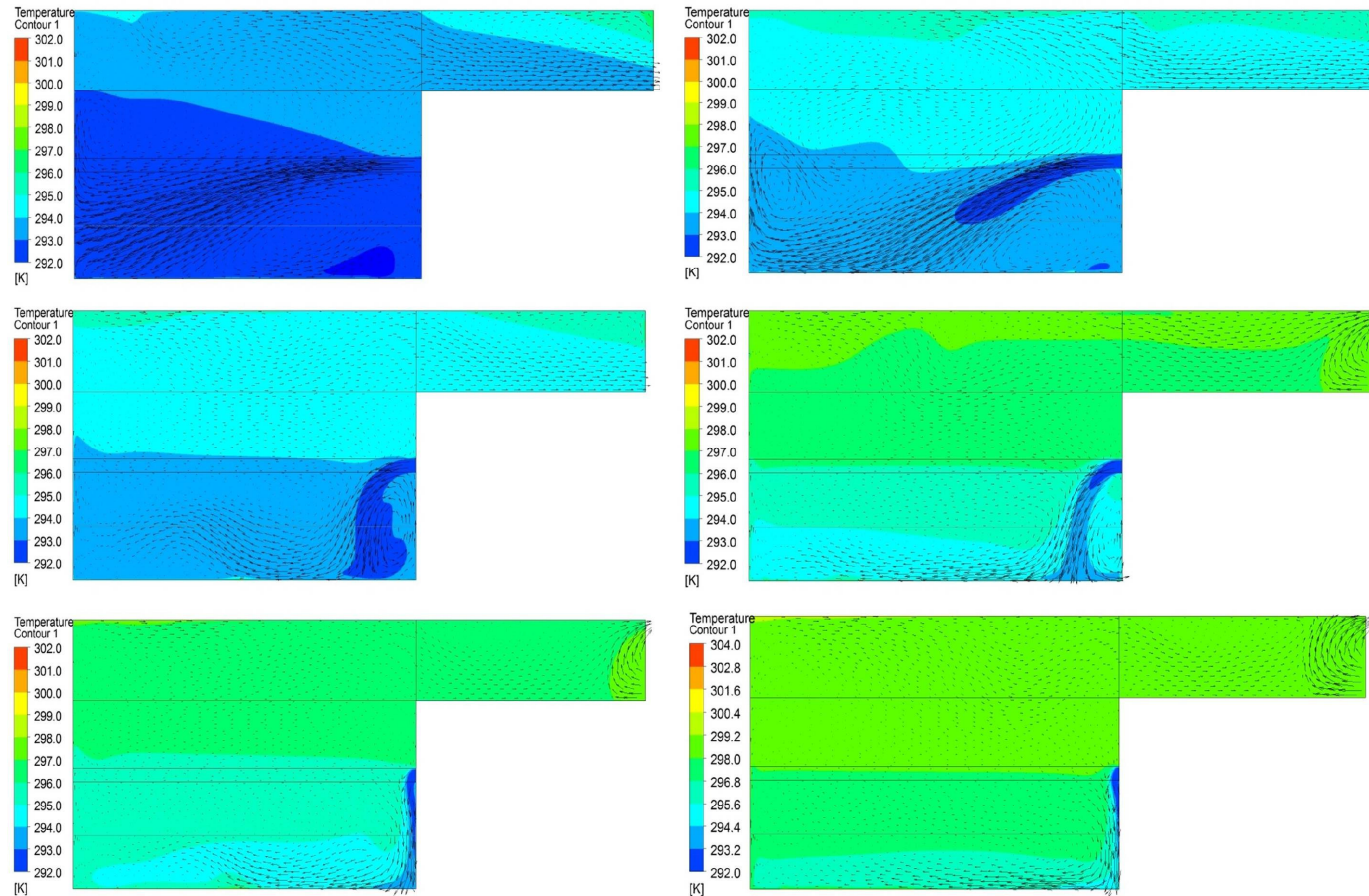


Figure 4.34 Temperature contour and velocity distribution plots for reference atrium at plane parallel to the facade intersecting the midpoint of the supply for winter case with (Left) single glazing (Right) double glazing with: supply set to 19°C and outside temperature set to -5°C. (Top) Supply set to 1m/s. (Middle) Supply set to 0.5m/s. (Bottom) Supply set to 0.25m/s.

Case	Location	1m/s	0.5m/s	0.25 m/s
		Energy [W]	Energy [W]	Energy [W]
W(i) Single Glazed	Supply	-14657.1	-7347.4	-3701.6
	Outlet	10959.1	4200.7	1250.4
	Facade	-12735.4	-13288.8	-14074.5
	Floor	7500.1	7500.1	7500.6
	North			
	Wall	8935.4	8935.4	8935.4
W(ii) Double Glazed	Supply	-14683.4	-7380.3	-3738.8
	Outlet	8301.1	1859.7	-850.1
	Facade	-9101.5	-9854.3	-10840.0
	Floor	3000.1	3000.5	2999.8
	North			
	Wall	12452.6	12452.6	12452.6

Table 4.23 Energy values comparing W(i)single glazed and W(ii) double glazed cases.

Case	Location	Avg Temp [K]	Max Temp [K]	Stratification [K]	Avg. Temp at Floor [K]
W(i) 1m/s	Entire Atrium	293.5	316.8	1.8	292.6
	Occupied Space	292.9	316.8	-0.1	292.6
W(i) 0.5m/s	Entire Atrium	294.5	319.5	1.6	293.4
	Occupied Space	293.9	319.5	0.1	293.4
W(i) 0.25m/s	Entire Atrium	296.3	321.8	1.7	295.0
	Occupied Space	295.4	321.8	0.3	295.0
W(ii) 1m/s	Entire Atrium	294.6	316.9	1.3	293.7
	Occupied Space	294.0	316.9	0.0	293.7
W(ii) 0.5m/s	Entire Atrium	296.7	318.8	2.0	295.1
	Occupied Space	295.4	318.8	0.3	295.1
W(ii) 0.25m/s	Entire Atrium	298.4	322.4	1.9	296.9
	Occupied Space	297.3	322.4	0.6	296.9

Table 4.24 Interior temperature results comparing W(i) single glazed and W(ii) double cases.

<b>Case</b>	<b>Avg. Floor Temp [K]</b>	<b>Avg, North Wall Temp. [K]</b>	<b>Avg. Wall Temp [K]</b>	<b>Avg. Façade Temp. [K]</b>
W(i) 1m/s	295.6	296.4	293.6	288.0
W(i) 0.5m/s	297.1	297.7	294.8	288.9
W(i) 0.25m/s	298.2	299.4	296.3	290.3
W(ii) 1m/s	296.4	299.4	295.5	290.8
W(ii) 0.5m/s	297.8	301.4	297.3	292.4
W(ii) 0.25m/s	299.4	303.2	298.9	293.9

Table 4.25 Surface temperature results comparing W(i)single glazed and W(ii) double glazed cases.

<b>Case</b>	<b>Max Velocity [m/s]</b>	<b>Avg Velocity [m/s]</b>
W(i) 1m/s	1.22	0.21
W(i) 0.5m/s	1.17	0.19
W(i) 0.25m/s	1.24	0.21
W(ii) 1m/s	1.17	0.18
W(ii) 0.5m/s	1.20	0.18
W(ii) 0.25m/s	1.16	0.19

Table 4.26 Velocity results comparing W(i)single glazed and W(ii) double glazed cases.

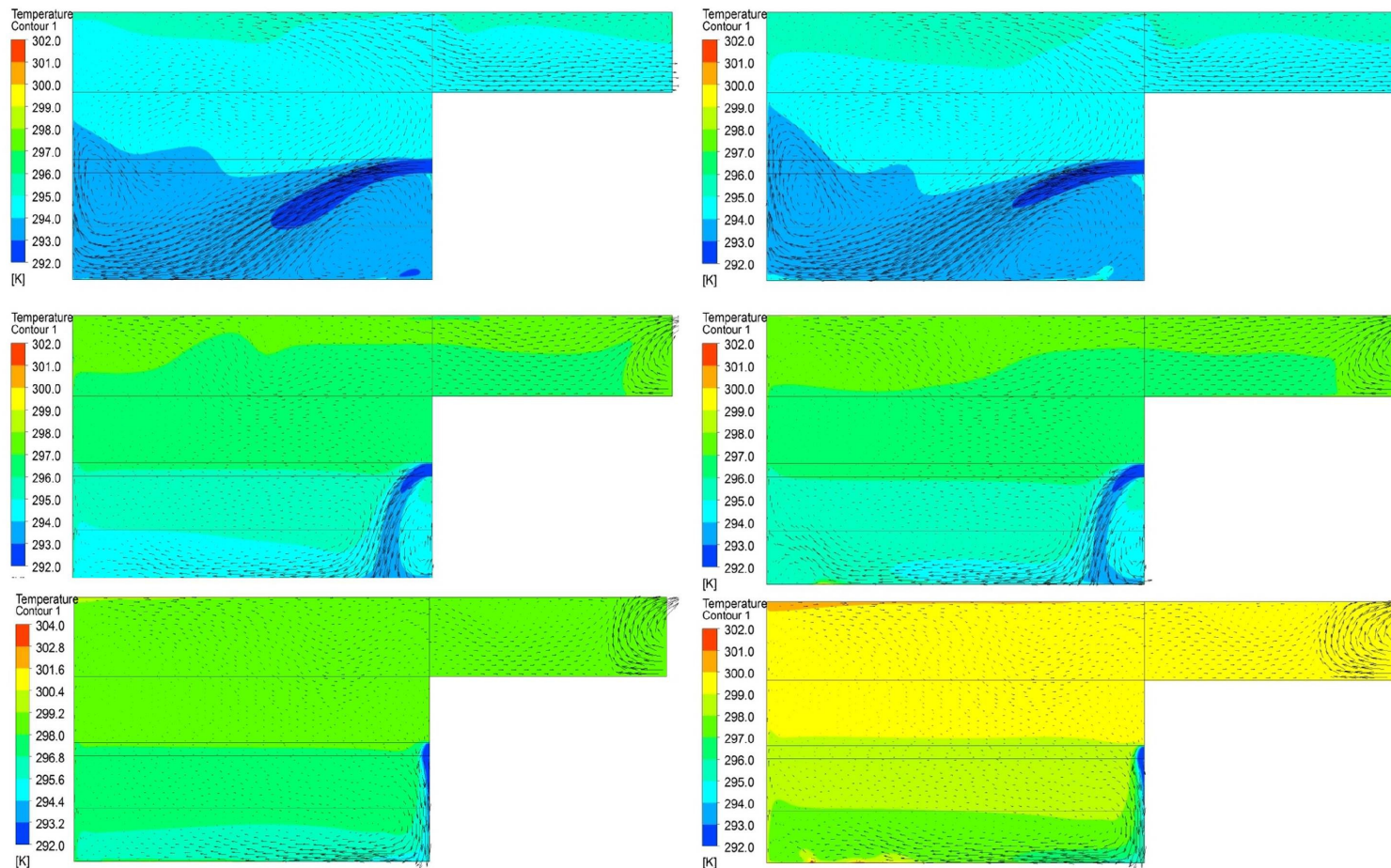


Figure 4.35 Temperature contour and velocity distribution plots for reference atrium at plane parallel to the facade intersecting the midpoint of the supply for winter case with (Left) double glazing without occupant load (Right) double glazing with occupant load 6by6 with: supply set to 19°C and outside temperature set to -5°C. (Top) Supply set to 1m/s. (Middle) Supply set to 0.5m/s. (Bottom) Supply set to 0.25m/s.

Case	Location	1m/s	0.5m/s	0.25 m/s
		Energy [W]	Energy [W]	Energy [W]
W(ii) Double Glazed	Supply	-14683.4	-7380.3	-3738.8
	Outlet	8301.1	1859.7	-850.1
	Facade	-9101.5	-9854.3	-10840.0
	Floor	3000.1	3000.5	2999.8
	North Wall	12452.6	12452.6	12452.6
W(iii)c Double Glazed 6by6	Supply	-14694.9	-7392.2	-3757.1
	Outlet	6955.8	659.5	-1895.3
	Facade	-11026.8	-12126.8	-13294.3
	Floor	6415.8	6415.8	6415.8
	North Wall	12452.6	12452.6	12452.6

Table 4.27 Energy values comparing W(ii) double glazed and W(ii) double glazed with people 6by6.

Case	Location	Avg Temp [K]	Max Temp [K]	Stratification [K]	Avg. Temp at Floor [K]
W(ii) 1m/s	Entire Atrium	294.6	316.9	1.3	293.7
	Occupied Space	294.0	316.9	0.0	293.7
W(ii) 0.5m/s	Entire Atrium	296.7	318.8	2.0	295.1
	Occupied Space	295.4	318.8	0.3	295.1
W(ii) 0.25m/s	Entire Atrium	298.4	322.4	1.9	296.9
	Occupied Space	297.3	322.4	0.6	296.9
W(iii)c 1m/s	Entire Atrium	294.8	317.0	1.1	294.1
	Occupied Space	294.3	317.0	0.0	294.1
W(iii)c 0.5m/s	Entire Atrium	296.8	319.2	1.9	295.3
	Occupied Space	295.6	319.2	0.3	295.3
W(iii)c 0.25m/s	Entire Atrium	299.3	322.2	1.9	297.7
	Occupied Space	298.1	322.2	0.6	297.7

Table 4.28 Interior temperature results comparing W(ii) double glazed and W(ii) double glazed with people 6by6.

<b>Case</b>	<b>Avg. Floor Temp [K]</b>	<b>Avg, North Wall Temp. [K]</b>	<b>Avg. Wall Temp [K]</b>	<b>Avg. Façade Temp. [K]</b>
W(ii) 1m/s	296.4	299.4	295.5	290.8
W(ii) 0.5m/s	297.8	301.4	297.3	292.4
W(ii) 0.25m/s	299.4	303.2	298.9	293.9
W(iii)c 1m/s	296.4	299.7	295.8	291.2
W(iii)c 0.5m/s	297.6	301.6	297.6	292.7
W(iii)c 0.25m/s	299.9	304	299.8	294.8

Table 4.29 Surface temperature results comparing W(ii) double glazed and W(ii) double glazed with people 6by6.

<b>Case</b>	<b>Max Velocity [m/s]</b>	<b>Avg Velocity [m/s]</b>
W(ii) 1m/s	1.17	0.18
W(ii) 0.5m/s	1.18	0.18
W(ii) 0.25m/s	1.16	0.19
W(iii)c 1m/s	1.17	0.18
W(iii)c 0.5m/s	1.17	0.19
W(iii)c 0.25m/s	1.17	0.19

Table 4.30 Velocity results comparing W(ii) double glazed and W(ii) double glazed with people 6by6.

*Case W(iv) - Winter day using double glazed system with changing outlet position*

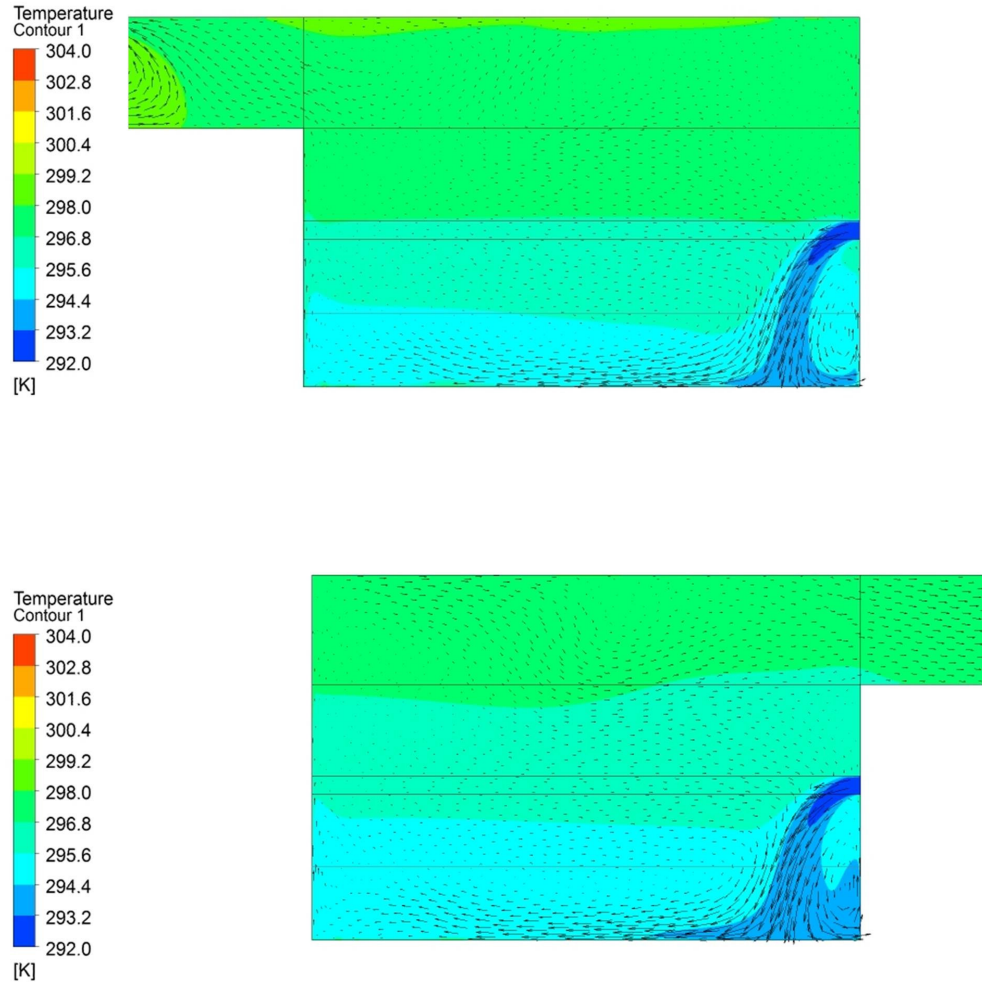


Figure 4.36 Temperature contour and velocity distribution plots for reference atrium at plane parallel to the facade intersecting the midpoint of the supply for winter case with double glazing with changing outlet positions: supply set to 19°C at 0.5m/s and outside temperature set to -5°C. (Top) Outlet positioned on west wall. (Bottom) Outlet positioned on east wall.

Location	W(iv) West Wall Outlet	W(ii) East Wall Outlet
	Energy [W]	Energy [W]
Supply	-7379.5	-7406.1
Outlet	1845.5	1859.7
Facade	-9845.5	-9854.3
Floor	3000.4	2999.9
North Wall	12452.6	12452.6

Table 4.31 Energy quantities comparing winter cases W(iv) and W(ii).

Case	Location	Avg. Temp [K]	Max Temp [K]	Stratification [K]	Avg. Temp Near Floor [K]
W(iv) West Wall Outlet	Entire Atrium Occupied	296.5	320.1	1.9	295.0
	Space	295.4	320.1	0.3	295.0
W(ii) East Wall Outlet	Entire Atrium Occupied	296.7	318.8	2.0	295.1
	Space	295.4	318.8	0.3	295.1

Table 4.32 Interior temperatures comparing winter cases W(iv) and W(ii).

Case	Avg. Floor Temp [K]	Avg. North Wall Temp. [K]	Avg. Wall Temp [K]	Avg. Façade Temp. [K]
W(iv) West Wall Outlet	297.8	301.8	297.9	291.9
W(ii) East Wall Outlet	298.3	302.1	298.2	291.4

Table 4.33 Average and maximum wall temperatures comparing winter cases W(iv) and W(ii).

Case	Max Velocity [m/s]	Avg. Velocity [m/s]
W(iv) West Wall Outlet	1.17	0.17
W(ii) East Wall Outlet	1.18	0.19

Table 4.34 Average and maximum velocities comparing winter cases W(iv) and W(ii).

*Case W(v) - Winter day using double glazed system with changing emissivity*

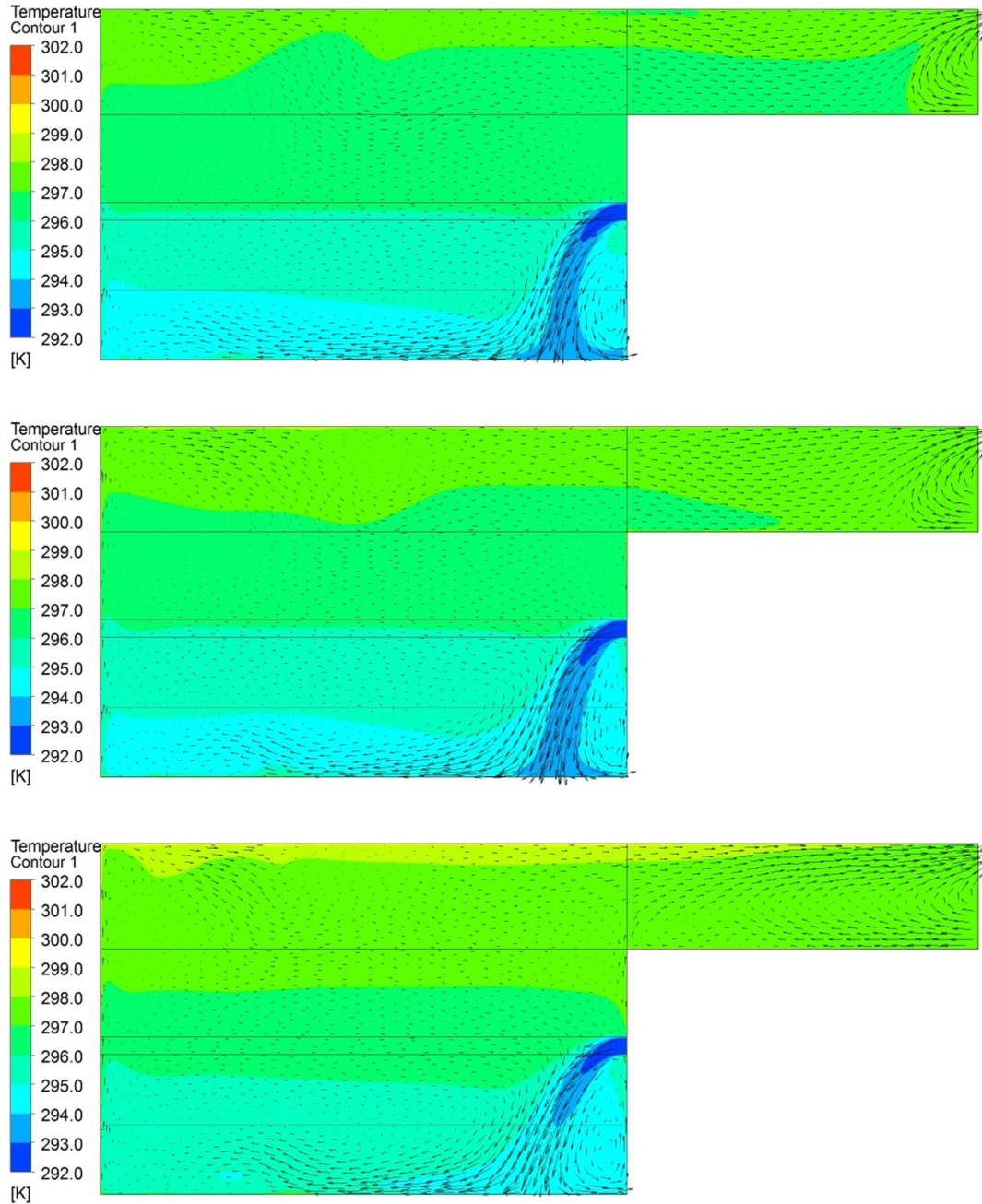


Figure 4.37 Temperature contour plots for reference atrium at plane parallel to the facade intersecting the midpoint of the supply for winter case with double glazing with changing facade emissivity: supply set to 19°C at 0.5m/s and outside temperature set to -5°C. (Top) Emissivity set 1. (Middle) Emissivity set to 0.5. (Bottom) Emissivity set to 0.25.

	<b>W(ii) <math>\epsilon=1</math></b>	<b>W(v) <math>\epsilon=0.5</math></b>	<b>W(v) <math>\epsilon=0.25</math></b>
<b>Location</b>	<b>Energy [W]</b>	<b>Energy [W]</b>	<b>Energy [W]</b>
Supply	-7379.5	-7406.1	-7434
Outlet	1515.3	1164.9	176.6
Facade	-9544.2	-9042	-8210.7
Floor	2999.9	2999.9	3000
North Wall	12452.6	12452.6	12452.6

Table 4.35 Energy quantities for winter case W(v).

<b>Case</b>	<b>Location</b>	<b>Avg. Temp [K]</b>	<b>Max Temp [K]</b>	<b>Stratification [K]</b>	<b>Avg. Temp Near Floor [K]</b>
W(ii) $\epsilon=1$	Entire Atrium	296.7	318.8	2.0	295.1
	Occupied Space	295.4	318.8	0.3	295.1
W(v) $\epsilon=0.5$	Entire Atrium	296.8	320.7	2.3	295.1
	Occupied Space	295.5	320.7	0.3	295.1
W(v) $\epsilon=0.25$	Entire Atrium	297.2	321.7	2.6	295.5
	Occupied Space	295.9	321.7	0.4	295.5

Table 4.36 Interior temperatures for winter case W(v).

<b>Case</b>	<b>Avg. Floor Temp [K]</b>	<b>Avg. North Wall Temp. [K]</b>	<b>Avg. Wall Temp [K]</b>	<b>Avg. Façade Temp. [K]</b>
W(ii) $\epsilon=1$	298.3	302.1	298.2	291.4
W(v) $\epsilon=0.5$	298.3	302.1	298.7	291.2
W(v) $\epsilon=0.25$	299.0	303.1	299.5	290.9

Table 4.37 Average and maximum wall temperatures for winter case W(v).

<b>Case</b>	<b>Max Velocity [m/s]</b>	<b>Avg. Velocity [m/s]</b>
W(ii) $\epsilon=1$	1.24	0.19
W(v) $\epsilon=0.5$	1.24	0.19
W(v) $\epsilon=0.25$	1.26	0.20

Table 4.38 Average and maximum velocities for winter case W(v).

## 4.7 Results Analysis (S) - Summer Cases

### *General Summer Case Notes*

From Figures 4.10 through 4.21, temperature stratification generally increases as the supply velocity decreases. As mentioned in the caption for Table 4.5 the stratification range for the entire atrium is measured between two horizontal planes: a near floor plane which is 0.2m above the floor and a near ceiling plane 0.2m below the ceiling; also the stratification in the occupied zone is measured between two horizontal planes: a near floor plane which is 0.2m above the floor and a horizontal plane 2m above the floor. Extreme temperatures at the floor and the ceiling are excluded from the measurements.

Flow near the outlet was greatly affected by the outlet temperature boundary condition. When the outlet temperature was below the bulk temperature near the outlet region, a noticeable amount of inflow caused mixing and cooler interior temperatures. Multiple iterations were required throughout case simulations to find outlet temperatures that would prevent inflow and unnecessary mixing. The effect of inflow based on outlet temperature was particularly evident in lower velocity cases.

### *S(Base Case) - Summer case with double glazing with supply set to 19°C at 0.5 m/s*

From Figure 4.9 (Top Row), the air from the inlet enters the atrium and travels along the floor towards the west wall, the flow then rises along the west wall due to buoyancy forces caused from the heated floor, the air then proceeds to the top and travels along the ceiling briefly before falling towards the middle of the atrium before flowing

through the outlet. There is an average temperature stratification of 1.8K from the top to the bottom of the atrium.

From Figure 4.9 (Middle Row) on the horizontal plane at height 1m from the floor, the supply air causes the flow across the entire plane to move towards the west wall. In the horizontal plane at height 5m from the floor, the air can be seen moving across the atrium from the west wall to the east wall and exiting through the outlet. Horizontal planes at heights 1m and 2m from the floor indicate an even temperature distribution temperature of 295.5K (22.5°C) which is within the thermal comfort zone.

From Figure 4.9 (Bottom Row), the flow near the glazing can be seen rising along the facade due to the heat flux from the floor; the air then falls towards the middle of the atrium.

#### *S(i) - Summer case with single glazing*

The single glazing case allowed for greater transmission of solar radiation compared to the double glazing case and as a result temperatures in the atrium are higher by approximately 1.4K. Stratification of the single glazed system is marginally higher compared to the double glazed case by 0.2K to 0.3K.

#### *S(ii) - Summer case with double glazing*

By comparing Figures 4.16 and 4.17, the double glazing cases were cooler compared to the single glazed cases by an average of 1.4K. Temperature stratification was slightly higher in the case where supply was set to 0.5m/s but remained the same as

the velocity was supply velocity was reduced to 0.25m/s. Average velocities were lower than the single glazed case by 0.02m/s.

*S(iii) - Summer case with double glazing and people*

From Figures 4.17 to 4.19, the addition of people becomes more apparent as more people are added. The occupied volume's temperature increases by 0.3K to 0.5K with each increase in occupant load. There is an increase in average velocity of 0.01m/s as more occupants are added into the atrium. The flow field generally behaves similar to the base case.

*S(iv) - Summer case with double glazing and west wall outlet*

As seen in Figure 4.20 and Table 4.25, the stratification in the case with the outlet positioned on the west wall is greater by 0.6K compared to the base case. Average wall and facade temperatures are higher by 0.4K to 0.6K in the west wall case. In the case with the outlet positioned on the west wall, the majority of air rising along the west wall exits through the west wall outlet whereas the air in the base case falls into towards the middle of the atrium and proceeds to exit through the east wall outlet.

*S(v) - Summer case with double glazing and changing glazing emissivity*

There was a slight increase of 0.5K in average wall temperature as the emissivity was changed from 1 to 0.5 and from 0.5 to 0.25. There were no significant changes in interior space temperatures.

## **(W) - Winter Cases**

### *General Winter Case Notes*

As indicated in Tables 4.32 and 4.36, heat losses through the facade become greater as the supply velocity decreases. Also, stratification generally increases as the supply velocity decreases. Maximum velocities for all cases away from the supply are found to be close to 1m/s and are located near the facade and north wall surfaces.

### *W(Base Case) - Winter case with double glazing with supply set to 19°C at 0.5m/s*

As illustrated in Figure 4.3, the winter cases were simulated with heat fluxes across the entire floor and a portion of the north wall. The heat fluxes were dependent on the type of glazing system modeled. For the single glazed system the heat fluxes on the floor and north wall were 70W/m<sup>2</sup> and 350 W/m<sup>2</sup> respectively. For the double glazed system the heat flux on the floor and north wall were 50W/m<sup>2</sup> and 250 W/m<sup>2</sup> respectively.

During the simulation of winter cases, cooling was required to achieve thermally comfortable conditions. Also the heat transfer coefficient of the glazing system had a significant impact on the heat losses through the façade. The single glazing system had a heat transfer coefficient of 5W/m<sup>2</sup> and the double glazing system had a heat transfer coefficient of 3W/m<sup>2</sup>.

From Table 4.37, there is a temperature stratification of approximately 2K for the entire atrium and 0.3K for the occupied space.

The flow in the winter base case is significantly different from the summer base case. From Figure 4.22 (Middle Row) on the plane horizontal to the floor at height 1m, the flow can be seen entering the atrium and traveling towards the North West corner of the atrium. From Figure 4.22 (Bottom Row), the flow can be seen traveling along the north wall with momentum caused by buoyancy forces. The air then travels to the top of the atrium and travels towards the cooler facade region; the flow then falls along the facade towards the floor.

The horizontal plane at height 1m from the floor indicates an average temperature distribution of 294.5K (21.5°C). The horizontal plane at height 2m from the floor indicates an average floor temperature of 295.5K (22.5°C). Both planes are within thermal comfort levels.

#### *W(i) - Winter case with single glazing*

As seen in Figure 4.27, the case with supply set to 1m/s does not satisfy thermal comfort conditions but was reported so that comparisons to other cases can be made using similar boundary conditions. This case in particular requires a higher supply temperature to be thermally comfortable. The higher U-factor in the single glazed case causes greater heat losses to the outdoor environment which is defined to be -5°C. Thermal comfort conditions are achieved in the lower velocity cases as well(i.e. 0.5m/s and 0.25m/s). The flow field behaves similar to the base case.

*W(ii) - Winter case with double glazing*

As seen in Figure 4.28, the double glazing cases prevent less heat transfer from the interior to the outdoor environment compared to the single glazed cases; as a result temperatures in the interior are much higher. The case with supply set to 1m/s satisfies thermal comfort conditions whereas the single glazed case with supply set to 1m/s did not. There is an increase of 0.1K to 0.4K in thermal stratification between the two cases as indicated in Tables 4.33 and 4.37. The flow field behaves similar to the winter base case.

*W(iii) - Winter case with double glazing and people*

The addition of people increases the temperatures of the interior space. Buoyancy effects caused by the human occupants can be seen in cases with lower velocities as illustrated in Figures 4.29, 4.30, and 4.31. Thermal stratification increases from 0.1K to 0.3K as supply velocity changes from 1m/s to 0.5m/s; and from 0.3K to 0.6K when the supply velocity changes from 0.5m/s to 0.25m/s. As more occupants are added interior temperatures increase but the range in stratification remains the same for the cases simulated. The flow field behaves similar to the base case.

*W(iv) - Winter case with double glazing and west wall outlet*

The range of thermal stratification are similar in magnitude, however, the heights of stratification bands seem to be different between the two cases as demonstrated in

Figure 4.32. The upper half of the atrium is slightly warmer in the west wall outlet case.

All other quantities are quite similar between the two cases.

*W(v) - Winter case with double glazing and changing emissivity*

As indicated in Table 4.57 and 4.58, as the emissivity increases the interior space and wall temperatures become warmer. From Figure 4.33, the change in thermal stratification is easily visible. The stratification increases from 2K to 2.3K as the emissivity changes from 1 to 0.5; and the stratification increases from 2.3K to 2.6K as the emissivity changes from 0.5 to 0.25. The effects of changing emissivity are more apparent in the winter case compared to the summer case. Low-emissivity coatings on glazing systems provide warmer interior temperatures.

<b>Case</b>	<b>Heat Flux (North Wall / Floor) [W/m<sup>2</sup>]</b>	<b>Supply Velocity [m/s]</b>	<b>Thermally Comfortable</b>
S(i) Single Glazed	- / 170	1	Yes
	- / 170	0.5	Yes
	- / 170	0.25	No
S(ii) Double Glazed	- / 100	1	Yes
	- / 100	0.5	Yes
	- / 100	0.25	No
S(iii)a Double Glazed 3by3	- / 100	1	Yes
	- / 100	0.5	Yes
	- / 100	0.25	No
S(iii)b Double Glazed 4by4	- / 100	1	Yes
	- / 100	0.5	Yes
	- / 100	0.25	No
S(iii)c Double Glazed 6by6	- / 100	1	Yes
	- / 100	0.5	Yes
	- / 100	0.25	No
S(iv) Double Glazed with Changing Outlets	- / 100	0.5	Yes
S(v) Double Glazed with Changing Emissivity	- / 100	0.5	Yes

Table 4.39 Thermal comfort results for simulated summer cases.

<b>Case</b>	<b>Heat Flux (North Wall / Floor) [W/m<sup>2</sup>]</b>	<b>Supply Velocity [m/s]</b>	<b>Thermally Comfortable</b>
W(i) Single Glazed	350 / 70	1	No
	350 / 70	0.5	Yes
	350 / 70	0.25	Yes
W(ii) Double Glazed	250 / 50	1	Yes
	250 / 50	0.5	Yes
	250 / 50	0.25	No
W(iii)a Double Glazed 3by3	250 / 50	1	Yes
	250 / 50	0.5	Yes
	250 / 50	0.25	Yes
W(iii)b Double Glazed 4by4	250 / 50	1	Yes
	250 / 50	0.5	Yes
	250 / 50	0.25	No
W(iii)c Double Glazed 6by6	250 / 50	1	Yes
	250 / 50	0.5	Yes
	250 / 50	0.25	No
W(iv) Double Glazed with Changing Outlets	250 / 50	0.5	Yes
W(v) Double Glazing with Changing Emissivity	250 / 50	0.5	Yes

Table 4.40 Thermal comfort results for simulated winter cases.

## 4.7 Conclusions

The following conclusions can be made from the results reported above:

- There is greater thermal stratification in single glazing cases versus double glazing cases, lower emissivity cases versus higher emissivity cases, and lower velocity cases.
- Human heat loads have a much larger effect when supply velocities are lower and are able to cause buoyancy effects in the flow field.
- The effect of changing the outlet position to the west wall causes a slight increase in thermal stratification for both summer and winter cases. The flow fields are also noticeably different and cause slight changes in the band thickness of stratification levels.
- Using the opening boundary condition in these simulations caused predictions to be highly dependent on the outlet temperature. Outlet temperature must match the bulk temperature near the outlet region in order to prevent fluid inflow. Fluid inflow can cause unexpected mixing, changes in interior temperatures, and changes in thermal stratification.
- Lowering the facade emissivity value increases the average volume temperatures and wall temperatures in the both summer and winter cases.
- Determining thermally comfortable conditions for any case require numerous iterations and sensitivity analysis of HVAC settings. (i.e. supply temperature and supply velocity)
- Thermal mass of concrete and other building materials must be considered when modeling buildings as they absorb and release significant amounts

of energy and effect overall predictions for temperatures. The effective energy entering the atrium space must be carefully considered and applied as a boundary condition.

- The glazing system must carefully be considered in the CFD analysis of buildings. The U-factor of glazing systems affects the overall heat transfer to and from the outside. Also, the glazing system controls the amount of sunlight that is absorbed, reflected, and transmitted. Solar radiation heat fluxes entering the atrium space are highly dependent on the date, time of day, and the amount that is transmitted through the glazing system.

The thermal performance of a hypothetical south facing atrium in Toronto, Canada has been simulated under a variety of cases and boundary condition configurations. The overall results of this study are in accordance with expectations and have further provided confidence that CFD is an effective tool in modeling thermal comfort, energy analysis, and the functionality of atria systems. Boundary conditions must be carefully considered and modeled correctly to ensure accurate results are predicted.

## **Chapter 5: Summary and Conclusions**

### **5.1 Summary**

The objective of this thesis was to explore the thermal comfort and HVAC conditions in a reference atrium for typical summer and winter days in Toronto, Ontario, Canada. The following results were achieved throughout this thesis.

A review of relevant research investigated the physical phenomena occurring within atria geometries, design considerations for energy efficiency and thermal comfort, HVAC and ventilation requirements, building simulation tools, and previous atria modeling work. Each section provided an in-depth look at the pertinent issues that should be considered when designing and analyzing atria structures from both design and functionality perspectives. From this review, it was concluded that there is limited application of CFD to the study of atria and there is further opportunity to better understand atria geometries and their potential to make these structures more energy efficient.

Validation of CFD predictions against experimental data was an important component of the current research. Turbulent natural convection was studied and it was determined that the  $k-\omega$  turbulence model provided the best comparison to experimental results of the two-equation turbulence models considered. The radiation heat transfer model was also validated by comparison to exact analytical solutions. Validations against data for actual atria were performed by simulating the heat transfer and fluid flow in the Concordia atrium and an experimental atrium located in Yokohama, Japan. The Concordia University atrium was instrumented by researchers at Concordia and

experimental measurements for temperature were recorded for a set of days. Rundle [2009] studied and simulated one of the cases using CFD and was able to achieve accurate results. The geometry in his work considered the indentation of walls near the HVAC supply. This thesis revisited Rundle's work and simulated the same case but using a simplified geometry that did not include the indentation near walls. Instead, the geometry was simplified into a rectangular box while maintaining the same volume as the complex geometry. The simplified geometry was simulated using the same boundary conditions as Rundle [2009]. The results between the two simulation cases were very close to each other with some differentiation caused due to the slight change in geometry. Two cases for the Yokohama atrium were simulated in this thesis: 1) natural convection case and 2) HVAC case. Using the experimental temperature measurements as boundary conditions, the atrium was modeled, simulated, and compared against experimental data for measurement points inside the atrium. The results of the natural convection case provided results within an average error of  $1^{\circ}\text{C}$  while the HVAC case provided results with an average error of  $3.3^{\circ}\text{C}$ . The difference in temperatures in the HVAC case was further investigated through various sensitivity analyses to supply direction, supply velocity, and solar heat flux. Changing the supply direction and velocity provided marginally improved results; however, qualitative trends near the supply were still not similar to experimental trends. Interchanging the temperature measurements, representative of the solar energy emitted by the walls, with a constant solar heat flux improved temperature predictions and decreased the average error to  $1.5^{\circ}\text{C}$ . Qualitative trends also slightly improved with the use of the constant heat flux boundary condition.

The discrepancies in the HVAC case can be attributed to the uninvestigated effects of solar shading and heating of thermocouples and inconsistency of the HVAC supply temperature [Heiselberg et al., 1998]. Both of these sources of error in the HVAC case may have caused unwanted errors within the experimental data.

In the final chapter, this thesis investigates a hypothetical reference atrium located in Toronto, Ontario, Canada. The reference atrium is a closed rectangular volume with the dimensions 15m (L) x 10 (W) x 10 (H); the atrium is south facing, with the south face being glazed, and the supply inlet and outlet positioned on the east wall. The reference atrium was simulated for a number of cases under typical summer and winter conditions. With the aim of satisfying thermal comfort conditions and optimizing the HVAC energy consumption, the study investigated the atrium's sensitivity to supply velocity, outlet temperature, outlet position, human occupancy, thermal mass, glazing system, and glazing emissivity. The simulations provided realistic results for a number of boundary condition configurations and cases. The research also uncovers an issue that was previously unaddressed in the analysis of atria geometries namely: the application of thermal mass in concrete and building envelopes. A significant amount of energy from the sun is absorbed and released by the concrete floor and must be accounted for appropriately. A methodology for assessing the temperature distribution of a concrete floor subject to solar heat flux is developed and described in Appendix D. Ideally, this method accounts for the portion of the incoming solar radiation that is absorbed by the concrete, convected by the air at the concrete surface, and emitted by the concrete. Carefully accounting for the thermal mass and effective heat flux which enters the

interior space is a very important step in atria energy analysis. If the thermal mass effect of the concrete floor is ignored, floor temperatures are excessively high and provide an unrealistic boundary condition which in turn provides excessively high interior temperatures.

## 5.2 Conclusions

This thesis sought out to uncover new facts and understanding about the heat transfer and fluid flow atria. This thesis provided a fundamental analysis of atria components and atria modeling work up to date. Through numerous validation studies and modeling of a reference atrium the following recommendations can be made with respect to atria and atria modeling:

- CFD is an exceptional building simulation tool in evaluating designs of atria. Although the use of CFD can be computationally intense, very detailed information regarding thermal comfort and energy consumption can be determined; in turn the atria designs can be modified easily to be more thermally comfortable and/or energy efficient.
- CFD requires well defined and accurate boundary conditions to produce reliable and accurate results. Boundary condition options unique to the CFD code being used should be tested for sensitivity. Numerous iterations are required to determine optimal HVAC conditions from both thermal comfort and energy efficiency perspectives.

- Using ANSYS-CFX, the  $k-\omega$  turbulence model performs particularly well in buoyancy problems when compared to other two-equation turbulence models such as  $k-\varepsilon$  and SST.
- The effective amount of solar radiation transmitting through the glazing must be accurately accounted for. Incoming solar radiation is greatly reflected depending on the angle of incidence.
- The thermal mass of the building envelope should be considered when simulating atria. Materials such as concrete can absorb a large amount of energy and have the potential to significantly alter the temperature of the interior space. When defining the effective heat flux which enters the atrium space, the thermal mass of the concrete must be considered. A method has been proposed in the current research for approximating the effect of thermal mass.
- The glazing system used can greatly impact heat transfer to and from the outside environment. Multi-layered glazing systems can provide much more insulation and less heat transfer to the exterior because of their overall lower heat transfer coefficients.
- The emissivity values of glazing systems can also provide much warmer interior temperatures. The low-emissivity coatings reflect longwave energy from interior walls back into the atrium space which allows for warmer interior temperatures. This is valuable in winter cases where a significant amount of energy can be lost through the glazing system.

### 5.3 Recommendations for Future Work

The following recommendations for future work of the study of fluid flow and heat transfer in atria geometries can be made:

- *Transient Simulations* - Although greater computational power is required, transient simulations would capture the true effect of changing solar heat fluxes and the effect of thermal mass. As a comparison exercise, it may be of interest to see the transient response of concrete and its effect on interior temperatures throughout the course of a day.
- *Natural Ventilation* - One of the main advantages of atria geometries is its potential for natural ventilation which can be used to both cool and ventilate the building. Simulating a natural ventilation case and testing its sensitivity to boundary conditions will reveal the pertinent factors about natural ventilation in atria designs.
- *Orientation* - The orientation of the atria is important to its performance and functionality. Ideally a south facing atrium provides the most potential to harness the sun's energy but changing the orientation may have both positive and negative effects.
- *Different Climates of Locations* - The climate and weather conditions will have a strong effect on atria performance, keeping a consistent design and simulating atria in different climates may provide interesting results.

## REFERENCES

- Allocca, C., Chen, Q., and L.R. Glicksman. (2003). Design analysis of single-sided natural ventilation. Energy and Buildings, 35. 785-795.
- Ampofo, F. and T.G. Karayiannis. (2003). Experimental benchmark data for turbulent natural convection in an air filled square cavity. International Journal of Heat and Mass Transfer. 46. 3551-3572.
- ANSYS CFX. “CEL Functions”. *ANSYS CFX Reference Guide*. 2006
- ANSYS CFX. “Comparison of the Radiation Models”. *ANSYS CFX Reference Guide*. 2006
- ANSYS CFX. “Discrete Transfer Model”. *ANSYS CFX Reference Guide*. 2006
- ANSYS CFX. “Guidelines for Mesh Generation”. *ANSYS CFX Reference Guide*. 2006
- ANSYS CFX. “Hybrid and Conservative Variables”. *ANSYS CFX Reference Guide*. 2006
- ANSYS CFX. “Lists of Symbols”. *ANSYS CFX Reference Guide*. 2006
- ANSYS CFX. “Mathematical Formulation”. *ANSYS CFX Reference Guide*. 2006
- ANSYS CFX. “Model Selection and Application”. *ANSYS CFX Reference Guide*. 2006
- ANSYS CFX. “Near Wall Treatment”. *ANSYS CFX Reference Guide*. 2006
- ANSYS CFX. “Numerical Errors”. *ANSYS CFX Reference Guide*. 2006
- ANSYS CFX. “Radiation Modeling”. *ANSYS CFX Reference Guide*. 2006
- ANSYS CFX. “Radiation Transport”. *ANSYS CFX Reference Guide*. 2006
- ANSYS CFX. “The k- $\epsilon$  Model”. *ANSYS CFX Reference Guide*. 2006
- ANSYS CFX. “Two Equation Turbulence Models”. *ANSYS CFX Reference Guide*. 2006
- ANSYS CFX. “Wall Heat Transfer”. *ANSYS CFX-Solver Modeling Guide*. 2006
- ASHRAE, (2005), ASHRAE Handbook-Fundamentals(SI), Atlanta: American Society of Heating, Refrigerating and Air-Conditioning Engineers, Inc.: Atlanta
- ASHRAE. (2003). Ventilation for Acceptable Air Quality. ASHRAE Standard 62.

- ASHRAE. (2004). Thermal environment conditions for Human Occupancy. ASHRAE Standard 55.
- Barakos, G. & E. Mitsoulis. (1994). Natural convection in a square cavity revisited: laminar and turbulent models with wall functions. International Journal for Numerical Methods in Fluids. 18. 695-719
- Breesch, H., Bossaer, A. & A. Janssens. (2005). Passive cooling in a low-energy office building. Solar Energy.79. 682-696.
- de Vahl Davis, G. & I.P. Jones (1983). Natural convection in a square cavity: a comparison exercise. International Journal for Numerical Methods in Fluids. 3(3). 227-248.
- Gocer, O., Tavit, A., and E. Ozkan. (2006). Thermal performance simulation of an atrium building. Proceedings of eSim 2006 Building Performance Simulation Conference.
- Heiselberg, P., Murakami, S., & C.A. Roulet. (1998). Experimental atrium. Ventilation of Large Spaces in Buildings. 217-237.
- Henkes, R.A. & C.J. Hoogendoorn. (1995). Comparison exercise for computations of turbulent natural convection in enclosures. Numerical Heat Transfer, Part B. 28. 59-78.
- Hiramatsu, T. (1994). Yokohama Atrium data. Received through email communication with Dr. Kato of Tokyo University. Communication date April 2010.
- Hiramatsu, T., Harada, T., Kato,S., Murakami, S., and H. Yoshino. (1996). Study of thermal environment in experimental real-scale atrium. 5th International Conference on Air Distribution in Rooms.
- Holford, J.M. & G.R. Hunt. (2003). Fundamental atrium design for natural ventilation. Building and Environment. 38. 409-426.
- Horan, J.M. and D.P. Finn. (2005). CFD reliability issues in analysis of naturally ventilated buildings. International Conference on “Passive and Low Energy Cooling for the Built Environment.
- Kato, S. (1994). Demonstration of Tools on Case Study Buildings. Received through email communication with Dr. Kato of Tokyo University. Communication date April 2010.

- Kato, S., Murakami, S., Shoya, S., Hanyu, F., and J. Zeng. (1995) CFD analysis of flow and temperature fields in atrium with ceiling height of 130 M. ASHRAE Transactions. 101.
- Laouadi, A. & M.R. Atif. (1999). Comparison between computed and field measured thermal parameters in an atrium building. Building and Environment. 34. 129-138.
- Laouadi, A. and M.R. Atif. (1999). Comparison between computed and field measured thermal parameters in atrium building. Building and Environment. 34. 129-138.
- Lau, J. and J.L. Niu. (2003). Measurement and CFD simulation of the temperature stratification in an atrium using a floor level air supply method. Indoor and Build Environment. 12. 265-280.
- Lin, Z. & S. Deng. A study on thermal comfort in sleeping environments in the subtropics. Building and Environment. 43. 70-80.
- Liu, P., Lin, H., and J. Chou. (2009) Evaluation of buoyancy-driven ventilation in atrium buildings using computational fluid dynamics and reduced-scale air model. Building and Environment. 19. 1-10.
- Mehta, M. (2005). Natural ventilation analyses of an office building with open atrium. Ninth International Conference for International Building Performance Simulation Association.
- Mora, L., Gadgil, A.J., & E. Wurtz. (2003). Comparing zonal and CFD model predictions of isothermal indoor airflows to experimental data. Indoor Air. 13. 77-85.
- Mouriki, E., Karava, P., Athienitis, A., Park, K., and Stathopoulos, T. (2007). Full-scale study of a hybrid ventilation system. Solar Buildings Research Network.
- Mouriki, E., Karava, P., Athienitis, A., Park, K., and T. Stathopoulos. (2008). Full-scale study of an atrium integrated with a hybrid ventilation system. Proceedings of the 3rd Solar Buildings Research Network Conference.
- Murakami, S. (1992). Prediction, analysis and design for indoor climate in large enclosures. Proceedings of Room Vent September 1992.
- Olesen, B.W. (2004). International standards for the indoor environment. Indoor Air 14. 18-26

- Oosthuizen, P.H. and M. Lightstone. (2009). Numerical analysis of the flow and temperature distributions in an atrium. Computational Methods for Energy and Environment.
- Ozeki, Y., Kato, S., and S. Murakami. (1996). Numerical analysis on flow and temperature fields in experimental real scale atrium. 5th International Conference on Air Distribution in Rooms.
- Penot, F. & A. N'Dame (1992). Successive bifurcations of natural convection in a vertical enclosure heated from the side. Heat Transfer, Third UK National Conference Incorporating First European Conference on Thermal Sciences, Birmingham, UK. 1. 507-513.
- Rundle, C. (2010). Validation of Modeling for Atria.
- Saxon, R. (1983). Atrium Buildings: Development and Design.
- Schild, P.G., Tjelflaat, P.O., and D. Aiulfi. (1995). Guidelines for CFD modeling of atria. ASHRAE Transactions.101(2). 1311-1332.
- Sharif, M.A.R. & W. Liu. (2003). Numerical Study of Turbulent Natural Convection in a Side-heated Square Cavity at Various Angles of Inclination. Numerical Heat Transfer, Part A, 43. 693-716.
- Simonetti, M., Fracastoro, G.V., and M. Perino. (2007). CFD transient analysis of night cooling strategy applied to school building. The 6th International Conference on Indoor Air Quality, Ventilation & Energy Conservation in Buildings.
- Tian, Y.S. & T.G. Karayiannis. (2000). Low turbulence natural convection in an air filled square cavity, Part I: Thermal and fluid flow fields, International Journal of Heat Mass Transfer 43. 849-866.
- Voeltzel, A., Carrie, F., and G. Guarracino. (2001). Thermal and ventilation modeling of large highly-glazed spaces. Energy and Buildings. 33.121-132.
- Walsh, P.C. and W.H. Leong. (2004). Effectiveness of several turbulence models in natural convection. International Journal of Numerical Methods for Heat & Fluid Flow, 14(5). 633-648.
- Wen J.X., Liu, F. & S. Lo. (2000). Performance Comparison of a Buoyancy-Modified Turbulence Model with Three LRN Turbulence Models for a Square Cavity. Numerical Heat Transfer Part B-Fundamentals. 39. 257-276.

## **Appendix A: Turbulence Models in CFX**

This section describes the two-equation turbulence models used in ANSYS-CFX. Two-equation models often provide a good balance between computational time and accuracy; and are often utilized as effective turbulence models for solving fluid flow and heat transfer problems. The following two-equation models are further explained below in detail: k- $\epsilon$ , k- $\omega$ , and Shear Stress Transport.

### **k- $\epsilon$ Turbulence Model**

The k- $\epsilon$  turbulence model utilizes two transport equations to close the Reynolds Averaged Navier Stokes (RANS) equations: k equation (representing the kinetic energy within the flow) and  $\epsilon$  (representing the energy dissipation within the flow). The transport equations for kinetic energy and dissipation are presented in equations A.1 and A.2 respectively.

$$\frac{\partial(\rho k)}{\partial t} + \nabla \cdot (\rho U k) = \nabla \cdot \left[ \left( \mu + \frac{\mu_t}{\sigma_k} \right) \nabla k \right] + P_k - \rho \epsilon \quad (\text{Equation A.1})$$

$$\frac{\partial(\rho \epsilon)}{\partial t} + \nabla \cdot (\rho U \epsilon) = \nabla \cdot \left[ \left( \mu + \frac{\mu_t}{\sigma_\epsilon} \right) \nabla \epsilon \right] + \frac{\epsilon}{k} (C_{\epsilon 1} P_k - C_{\epsilon 2} \rho \epsilon) \quad (\text{Equation A.2})$$

As demonstrated by Launder and Spalding [1973] the eddy viscosity is represented by the relationship shown in equation A.3.

$$\mu_t = C_\mu \rho \frac{k^2}{\epsilon} \quad (\text{Equation A.3})$$

The constants in the above equations have the following values as defined by Launder & Spalding [1973].

$$C_\mu = 0.09$$

$$C_{\varepsilon 1} = 1.44$$

$$C_{\varepsilon 2} = 1.92$$

$$\sigma_k = 1$$

$$\sigma_\varepsilon = 1.3$$

The term  $P_k$  is a production term represented by equation A.4.  $P_{kb}$  represents the production of turbulent kinetic energy due to buoyancy.

$$P_k = \mu_t \nabla U \cdot (\nabla U + \nabla U^T) - \frac{2}{3} \nabla \cdot U (3\mu_t \nabla \cdot U + \rho k) + P_{kb} \quad (\text{Equation A.4})$$

### *Near Wall Treatment*

For turbulent flows near walls, two-equation turbulence models must be modified to account for the boundary layer. Although Launder & Spalding [1973] suggest two methods, low Reynolds modeling and wall functions, ANSYS-CFX only provides a scalable wall function for the k- $\varepsilon$  model. The scalable wall function uses the following velocity scale shown in A.5.

$$u^* = C_\mu^{1/4} k^{1/2} \quad (\text{Equation A.5})$$

The scalable wall function is based on the log-law of the wall for velocity and the value of  $y^*$  is limited to 11.06. Equation A.6 is an expression used to determine the value of  $y^*$ .

$$y^* = \max\left(\frac{\rho u^* \Delta y}{\mu}, 11.06\right) \quad (\text{Equation A.6})$$

These values are then used to solve for the wall stress and friction velocity as shown in equations A.7 and A.8.

$$u_\tau = \frac{U_t}{\frac{1}{\kappa} \ln(y^*) + C} \quad (\text{Equation A.7})$$

$$\tau_\omega = \rho u^* u_\tau \quad (\text{Equation A.8})$$

### *Model Issues*

The k-ε turbulence model in ANSYS-CFX models free stream turbulent flows well, however, its modeling issues arise when modeling flow separation or flow along curved surfaces. The scalable wall function associated with the k-ε turbulence model also has issues modeling flows with low Reynolds numbers. For example, buoyancy cavity flows.

### k- $\omega$ Turbulence Model

The k- $\omega$  turbulence model developed by Wilcox [1993] is similar to the k- $\epsilon$  model by using two transport equations to close the RANS equations: k (representing the kinetic energy in the flow) and  $\omega$  (representing the turbulent frequency). The transport equations for kinetic energy and frequency are shown in equations A.9 and A.10:

$$\frac{\partial(\rho k)}{\partial t} + \nabla \cdot (\rho U k) = \nabla \cdot \left[ \left( \mu + \frac{\mu_t}{\sigma_k} \right) \nabla k \right] + P_k - \beta' \rho k \omega \quad (\text{Equation A.9})$$

$$\frac{\partial(\rho \omega)}{\partial t} + \nabla \cdot (\rho U \omega) = \nabla \cdot \left[ \left( \mu + \frac{\mu_t}{\sigma_\omega} \right) \nabla \omega \right] + \alpha \frac{\omega}{k} (P_k) - \beta \rho \omega^2 \quad (\text{Equation A.10})$$

The eddy viscosity relationship under the k- $\omega$  turbulence model is shown in equation A.11.

$$\mu_t = \rho \frac{k}{\omega} \quad (\text{Equation A.11})$$

The Wilcox k- $\omega$  turbulence model uses the same equation for the  $P_k$  term as the k- $\epsilon$  model. The constants in the k- $\omega$  are presented below:

$$\beta' = 0.09$$

$$\alpha = 5/9$$

$$\beta = 0.075$$

$$\sigma_k = 2$$

$$\sigma_\omega = 2$$

### *Near Wall Treatment*

In ANSYS-CFX, the near wall treatment of the k- $\omega$  turbulence model is an automatic wall treatment. This is a combination of a low Reynolds number model and a wall function. ANSYS CFX [2010] uses equations A.12, A.13, A.14 and A.15 to define the automatic wall treatment. The automatic wall treatment has been derived from an analytical solution for  $\omega$  in the viscous sub layer region [ANSYS, 2010].

$$u_{\tau} = \sqrt{\nu \left| \frac{\Delta U}{\Delta y} \right|} \quad (\text{Equation A.12})$$

$$\omega_l = \frac{1}{a_1 \kappa} \frac{u_{\tau}^2}{y^+} \quad (\text{Equation A.13})$$

$$\omega_s = \frac{6\nu}{\beta(\Delta y)^2} \quad (\text{Equation A.14})$$

$$\omega_{\omega} = \omega_s \sqrt{1 + \frac{\omega_l}{\omega_s}} \quad (\text{Equation A.15})$$

### *Model Issues*

The k- $\omega$  turbulence model is effective in modeling low Reynolds number flows, however, the model has a distinct dependency on the free stream conditions and is insensitive to curved surfaces and rotating flows. Also the model is not particularly effective when adverse pressure gradients are apparent in the flow.

### Shear Stress Transport (SST) Turbulence Model

The Shear Stress Transport turbulence model combines the k-ε and k-ω turbulence models using a blending function. The SST model utilizes the k-ω model near the wall and blends a transformed k-ε model as the edge of the boundary layer is approached. The transformed k-ε transport equations are modified to resemble k-ω equations and are shown in equations A.16 and A.17.

$$\frac{\partial(\rho k)}{\partial t} + \nabla \cdot (\rho U k) = \nabla \cdot \left[ \left( \mu + \frac{\mu_t}{\sigma_k} \right) \nabla k \right] + P_k - \beta' \rho k \omega \quad (\text{Equation A.16})$$

$$\frac{\partial(\rho \omega)}{\partial t} + \nabla \cdot (\rho U \omega) = \nabla \cdot \left[ \left( \mu + \frac{\mu_t}{\sigma_{\omega 2}} \right) \nabla \omega \right] + \frac{2\rho \nabla k \nabla \omega}{\sigma_{\omega 2} \omega} + \alpha_2 \frac{\omega}{k} (P_k) - \beta_2 \rho \omega^2$$

(Equation A.17)

$$\beta' = 0.09$$

$$\alpha_1 = 5/9$$

$$\beta_1 = 0.075$$

$$\sigma_{k1} = 2$$

$$\sigma_{\omega 1} = 2$$

$$\alpha_2 = 0.44$$

$$\beta_2 = 0.0828$$

$$\sigma_{k2} = 1$$

$$\sigma_{\omega 2} = 1/0.0856$$

The k-ω is multiplied by a blending function  $F_1$  the transformed k-ε equation is multiplied by  $(1-F_1)$ , and the resulting equations for k and ω are combined to produce

equations A.18 and A.19. The blending function  $F_1$  is presented in equations A.20, A.21  
A.22.

$$\frac{\partial(\rho k)}{\partial t} + \nabla \cdot (\rho U k) = \nabla \cdot \left[ \left( \mu + \frac{\mu_t}{1} \right) \nabla k \right] + P_k - \beta' \rho k \omega \quad (\text{Equation 3.18})$$

$$\frac{\partial(\rho \omega)}{\partial t} + \nabla \cdot (\rho U \omega) = \nabla \cdot \left[ \left( \mu + \frac{\mu_t}{\sigma_{\omega 3}} \right) \nabla \omega \right] + (1 - F_1) \frac{2\rho \nabla k \nabla \omega}{\sigma_{\omega 2} \omega} + \alpha_3 \frac{\omega}{k} (P_k) - \beta_3 \rho \omega^2$$

(Equation A.19)

$$F_1 = \tanh(\arg_1^4) \quad (\text{Equation A.20})$$

$$\arg_1 = \min \left( \max \left( \frac{\sqrt{k}}{0.09 \omega y}, \frac{500 \nu}{y^2 \omega} \right), \frac{4 \rho k}{CD_{kw} \sigma_{\omega 2} y^2} \right) \quad (\text{Equation A.21})$$

$$CD_{kw} = \max \left( 2 \rho \frac{1}{\sigma_{\omega 2} \omega} \nabla k \nabla \omega, 1.0 \times 10^{-10} \right) \quad (\text{Equation A.22})$$

The SST turbulence limits the value of the eddy viscosity to better account for the transport of turbulent shear stress. Equation A.23 shows the original definition of the eddy viscosity and equation A.24 shows the modified definition.

$$\nu_t = \frac{\mu_t}{\rho} \quad (\text{Equation A.23})$$

$$\nu_t = \frac{a_1 k}{\max(a_1 \omega, SF_2)} \quad (\text{Equation A.24})$$

The quantity  $S$  is an invariant measure of the strain rate and  $a_1$  is the Bradshaw constant. The second blending function limits the reduction of the eddy viscosity to the boundary layer and is defined in equations A.25 to A.26.

$$F_2 = \tanh(\arg_2^2) \quad (\text{Equation A.25})$$

$$\arg_2 = \max\left(\frac{2\sqrt{k}}{0.09\omega y}, \frac{500\nu}{y^2\omega}\right) \quad (\text{Equation A.26})$$

### *Near Wall Treatment*

The SST turbulence model utilizes the same automatic wall treatment used by the  $k-\omega$  turbulence model.

### *Model Issues*

The SST model accounts for the transport of the turbulent shear stress and gives accurate predictions of flow separation and flows under adverse pressure gradients. However, it is unclear where the SST model's blending function occurs and can potentially cause unexpected changes to the predicted results.

## **APPENDIX B: PROPERTIES OF GLAZED SURFACES**

### Motivation

This section was developed to better understand how glazed surfaces interact with solar radiation. It is important to understand the behavior of these glazing systems so that they can be modeled effectively and accurately account for the amount of solar radiation entering an interior space.

### Sunlight Composition

Sunlight can be divided into 3 wavelength regions (approximate values): 7% is ultraviolet (0-0.38  $\mu\text{m}$ ), 47% is visible (0.38-0.78  $\mu\text{m}$ ), and 46% is infrared (0.78 $\mu\text{m}$  and greater) [Duffie & Beckman, 1980]. Shortwave radiation ideally has a wavelength range of 0.3 to 3.0  $\mu\text{m}$ , while longwave radiation has wavelengths greater than 3.0  $\mu\text{m}$ .

Longwave radiation can be classified as radiation emitted from surfaces that are close to room temperature.

Solar radiation consists of two components: beam radiation and diffuse radiation. Beam radiation is the direct solar radiation that is not scattered or disturbed by atmospheric particles. Diffuse radiation is solar radiation that has been scattered due to atmospheric particles. Shorter wavelengths of sunlight get scattered by atmospheric particles because their magnitude in size is comparable to those of the atmospheric particles (i.e. blue light), while longer wavelengths are much larger and are unaffected by the atmosphere's particles (i.e. red light). Ground reflection is also a component that should also be considered when calculating the overall solar heat gain of a glazing

system. The ground's reflectivity of solar radiation may account for up to 20% of the overall solar radiation incident on a surface depending on the reflectivity of the surface; especially in cases where the ground is covered by snow.

### Properties of Glazing Materials

When solar radiation strikes the surface of a glass, some of it is absorbed, reflected and transmitted. Percentages of transmission, absorption, and reflection are dependent on the thermophysical and geometric properties of the glazed surface. A typical single pane of glass absorbs approximately 12%, reflects 8% and transmits 80% of the solar radiation striking the surface [McQuiston et al., 2002]. Figure B.1 illustrates the breakdown of solar radiation falling on a clear plate of glass. ASHRAE Handbook of Fundamentals [2009] provides a list of thermal properties for a number of different types of glazing including properties for different incident angles. It should be noted that manufacturers often provide glazing property information only for the case when the sunlight is perpendicular. The properties of glazing systems can also change depending on the number of layers of glass and the types of coatings applied. Double layer and triple layer glazing can reduce the transmission of solar radiation to 50% to 60%.

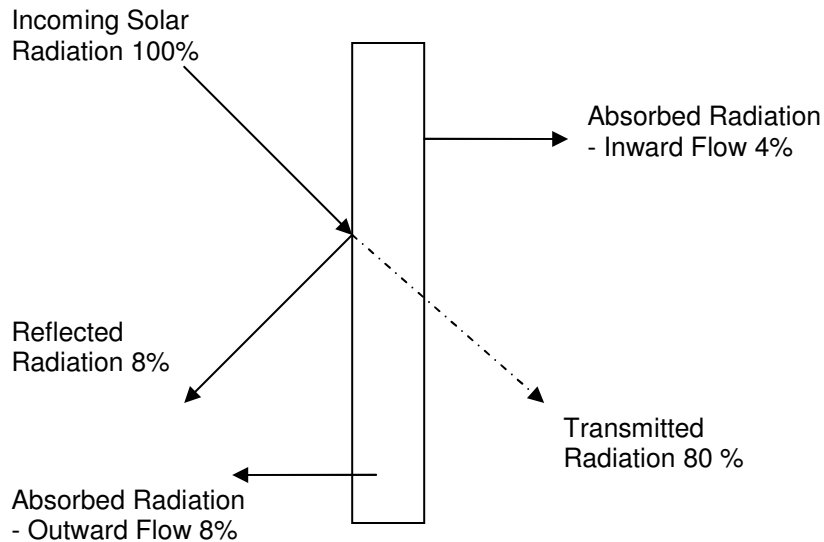


Figure B.1 Breakdown of solar radiation striking a clear pane of glass.

### *Transmission*

Short wave radiation (i.e. solar radiation) transmits through a typical untreated pane of glass within the range of 80-90% [ASHRAE, 2009]. The rest of the solar radiation is either reflected back into the atmosphere or absorbed by the glass. Glass is generally opaque to longwave radiation [Duffie & Beckman, 1980]. Long wave radiation from objects heated by the sun's shortwave radiation (i.e. sunlit thermal mass objects) are absorbed by glazed surfaces and are not transmitted through. Instead, the longwave radiation causes the surface temperature of the glass to increase and create a potential for heat transfer to the outside through conduction.

### *Reflectivity*

The reflectivity of the glass is dependent on the angle of incidence as well as its physical properties. The reflectivity of glass significantly increases when the incident angle becomes larger than  $40^\circ$  [ASHRAE, 2009]. ASHRAE's Handbook of Fundamentals provides a comprehensive list of various glazing systems and provides their glazing properties for various incident angles.

### *Absorptivity*

The sunlight that is neither transmitted or reflected through the glass is absorbed. Under the grey body assumption emissivity and absorptivity have equal values. Long wave radiation from heated interior objects is absorbed by the glass and causes a potential for heat loss to the exterior when outdoor temperatures are colder than the interior. These heat losses can be mitigated through the use of low emissivity coatings.

### Solar Heat Gain Coefficients

The Solar Heat Gain Coefficient (SHGC) is a coefficient used to define the overall solar heat gain of a glazing system. The SHGC considers the transmitted radiation through the glass, the inward flowing portion of the absorbed radiation, and inward flowing portion of the heat absorbed by the window frame and combines them to provide an overall solar heat gain coefficient. It does not consider the conduction heat transfer caused due to temperature differences between the inside and outside environments. Values of SHGC as well as the other thermal properties of the glazing are

also dependent on the sun's angles of incidence. ASHRAE Handbook of Fundamentals provides a thorough table of glazing properties for a variety of glazing systems.

### U-Factors

The U-factors of glazing systems represent the overall heat transfer coefficient of the glazing system; and they can be found in ASHRAE's Handbook of Fundamentals. The U-factors are particularly convenient when calculating heat transfer quantities to and from the outdoor environment.

### Low Emissivity Glass

Low emissivity glass is glass that is coated with a low emissivity coating which is usually made from fine metal oxides. The low emissivity coatings are designed to reflect particular wavelengths but remain transparent to others. They reflect longwave radiation and help to create a window with a low U-factor and high solar heat gain coefficient. During hot summer days longwave radiation from the environment is kept from entering the interior space and is reflected back out towards the atmosphere. During cold winter days longwave radiation emitted from heated interior surfaces is reflected back into the interior space. As a result the interior space is cooler during the summer days and warmer during the winter days when compared to untreated glass.

Low emissivity coatings can be placed on either side of the glazing surface depending on the climate of the building. In cooler climates, the interior space aims to keep warm and the low emissivity coating should be placed on the inside surface of the

glazing to reflect longwave radiation back to the interior space (minimizing the glazed surface from heating up and losing its heat to the exterior). In warmer climates, the low emissivity coatings should be placed on the outside of the glazed surface to reflect longwave radiation from the outdoor environment and prevent overheating of the facade surface.

### Coatings and Tinting

Reflective coatings are coatings placed on glass to reflect incoming solar radiation. Many buildings with windows and glazed surfaces often require reflective coatings to limit the amount of sunlight coming in so that spaces are occupiable to conduct work. There are a wide range of reflective coatings that limit specific wavelengths of sunlight so that occupants can enjoy the view to the exterior environment without exposure to harmful UV rays, high intensity visible light, and glare. Many buildings incorporate tinted glass and other reflectivity coatings to ensure that office spaces are occupiable and functional during days when solar radiation is excessively high.

### Multi-layered Glazing Systems

Double and triple layered glazing systems have significantly different properties compared to single glazed systems. Double and triple glazed systems can reduce solar transmission down to 50% due to its multiple layers and can provide greater insulation

for the interior space. The space between glazed layers acts as a thermal buffer zone where air or argon gas can be used as an insulator.

## **APPENDIX C: RADIATION VALIDATION PROBLEM**

### Motivation

This section presents a validation study of the CFD code ANSYS-CFX for radiation problems involving glazed surfaces.

### Description

A simple problem has been set up where solar radiation is transmitted through a glazed surface and strikes an opaque wall. The transmitted solar radiation is modeled as a constant heat flux with a value of  $100 \text{ W/m}^2$ . An outdoor temperature, exterior of the glazed surface, was chosen to be  $20^\circ\text{C}$  with a standard (no wind) heat transfer coefficient of  $5 \text{ W/m}^2\text{K}$ . Exterior and interior surface temperatures of the glazed surface and the wall temperature are not known. Emissivities of both the glass and the wall were initially selected to be unity. The glass has a thickness of  $0.05 \text{ m}$  with a thermal conductivity of  $1.4 \text{ W/mK}$ . The thickness of the air volume is  $2 \text{ meters}$ . A schematic of the problem is provided in Figure C.1. This problem was assumed to be one dimensional with interior convection and conduction effects omitted. A simple analytical radiation calculation was done and compared to the simulated results. Boundary conditions for the glazing and wall were inputted into the CFD model and simulated. The discrete transfer radiation model was used in this study.

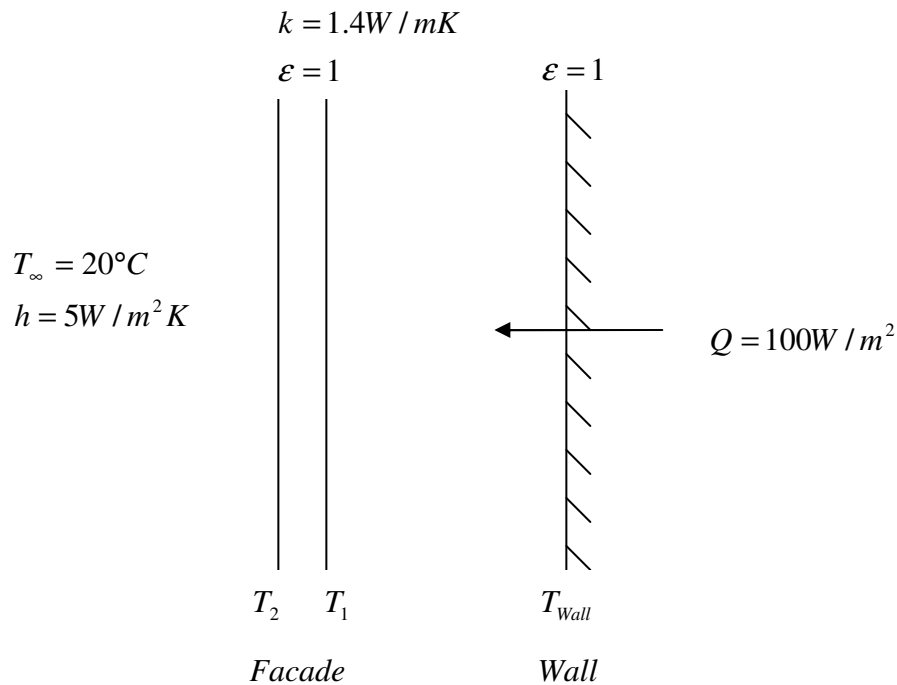


Figure C.1 Diagram of the radiation validation problem.

### Problem Analysis and Results

Listed below are the equations necessary to solve the analytical solution to this radiation problem. Equation C.1 represents the constant heat flux from solar radiation at the wall surface. Equation C.2 represents the radiation emitted from the wall. Equation C.3 represents the conduction within the glazed surface. Equation C.4 represents the convection occurring at the exterior side of the façade. Equation C.4 can immediately be solved for  $T_2$  with the values given in the problem. The temperature at  $T_2$  equals 313K. In turn, substituting the value for  $T_2$  into equation 3 provides a  $T_1$  temperature of 316.57K. Using equation C.2, the wall temperature is found to be 329.56K. Table C.1 is

a summary of the temperatures derived by both solutions. Comparing the analytical solution to the simulated solution indicates that the code produces accurate results.

$$Q'' = 100 \frac{W}{m^2} \quad \text{Equation C.1}$$

$$Q'' = \epsilon\sigma(T_{Wall}^4 - T_1^4) \quad \text{Equation C.2}$$

$$Q'' = \frac{k}{l}(T_1 - T_2) \quad \text{Equation C.3}$$

$$Q'' = h(T_2 - T_\infty) \quad \text{Equation C.4}$$

Location	Analytical Solution Temperatures [K]	Numerical Solution Temperatures [K]
$T_1$	313.00	312.98
$T_2$	316.57	316.58
$T_{Wall}$	329.55	329.56

Table C.1 Comparison of analytical and numerical solutions for  $\epsilon_{Wall} = 1$  and  $\epsilon_1 = 1$

The glass emissivity was then changed to 0.3. The inverse relationship between emissivity and reflectivity results in reflectivity to increase to 0.7. As a result, the wall temperature is expected to increase while glass temperatures remains the same. The analytical solution requires an effective emissivity to be calculated first and then the remaining wall temperature can be solved using Equations C.5 and C.6. Table C.2 provides a summary of results for the analytical and numerical solutions for the case when  $\epsilon_{wall} = 1$  and  $\epsilon_1 = 0.3$ . The effective emissivity was found to be 0.3. Figure C.2 is a resistance diagram representative of the radiation problem with differing emissivity values for the wall and facade. The results indicate that the analytical and numerical solutions produce very similar results.

The emissivity of the wall was then changed to 0.5 and the facade surface emissivity was selected to 0.3. Table C.3 represents the analytical and numerical results for the radiation problem when  $\epsilon_{wall} = 0.5$  and  $\epsilon_1 = 0.3$ . The effective emissivity was found to be 0.231. The results here also indicate that the analytical and numerical solutions also produce very similar results. It can be concluded that ANSYS-CFX does an accurate job at providing a heat transfer solution for this simple radiation problem which should also provide the user with confidence when utilizing the CFD code to solve more complex glazing radiation problems involving glazed surfaces.

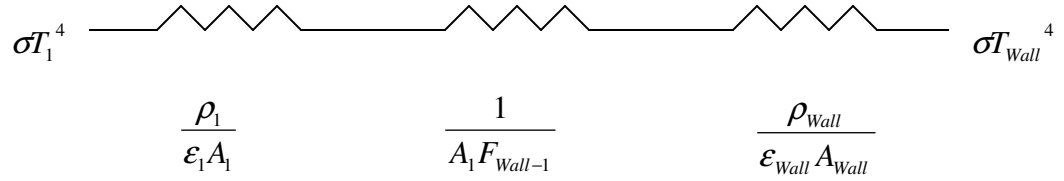


Figure 2. Resistance diagram representing the radiation heat transfer problem for different wall and facade emissivity values.

$$e_{eff} = \frac{1}{\left(\frac{\rho_1}{\epsilon_1 A_1}\right) + \left(\frac{1}{A_{wall} F_{wall-1}}\right) \left(\frac{\rho_{wall}}{\epsilon_{wall} A_{wall}}\right)} \quad \text{Equation C.5}$$

$$100W / m^2 = e_{eff} \sigma (T_{wall}^4 - T_1^4) \quad \text{Equation 6.}$$

Location	Analytical Solution Temperatures [K]	Numerical Solution Temperatures [K]
$T_1$	313.00	312.94
$T_2$	316.57	316.51
$T_{wall}$	355.06	354.87

Table C.2 Comparison of analytical and numerical solutions for  $\epsilon_{wall} = 1$  and  $\epsilon_1 = 0.3$

Location	Analytical Solution Temperatures [K]	Numerical Solution Temperatures [K]
$T_1$	313.00	312.94
$T_2$	316.57	316.51
$T_{Wall}$	364.27	363.90

Table C.3 Comparison of analytical and numerical solutions for  $\epsilon_{wall} = 0.5$  and  $\epsilon_1 = 0.3$

## **APPENDIX D: REFERENCE ATRIUM CASE RESULTS**

### Background

The hypothetical reference atrium, located in Toronto, Canada, was simulated for typical summer and winter conditions at solar noon. A few cases examining the effect of human occupant load were simulated but did not provide significantly different results compared to the case without human occupants. The results of these cases are presented here in this appendix for reference. Temperature contour plots for each of the cases are presented in Figures D.1 to D.4. The energy balances, temperatures, and velocities for the reference atrium are presented in Tables D.1 to D.16. The following cases are presented in this appendix:

- S(iii)a – Summer case with double glazing and occupant load 3by3
- S(iii)a – Summer case with double glazing and occupant load 4by4
- W(iii)a – Winter case with double glazing and occupant load 3by3
- W(iii)a – Winter case with double glazing and occupant load 4by4

*Case S(iii)a - Summer day using double glazed system with 3 by 3 occupant load*

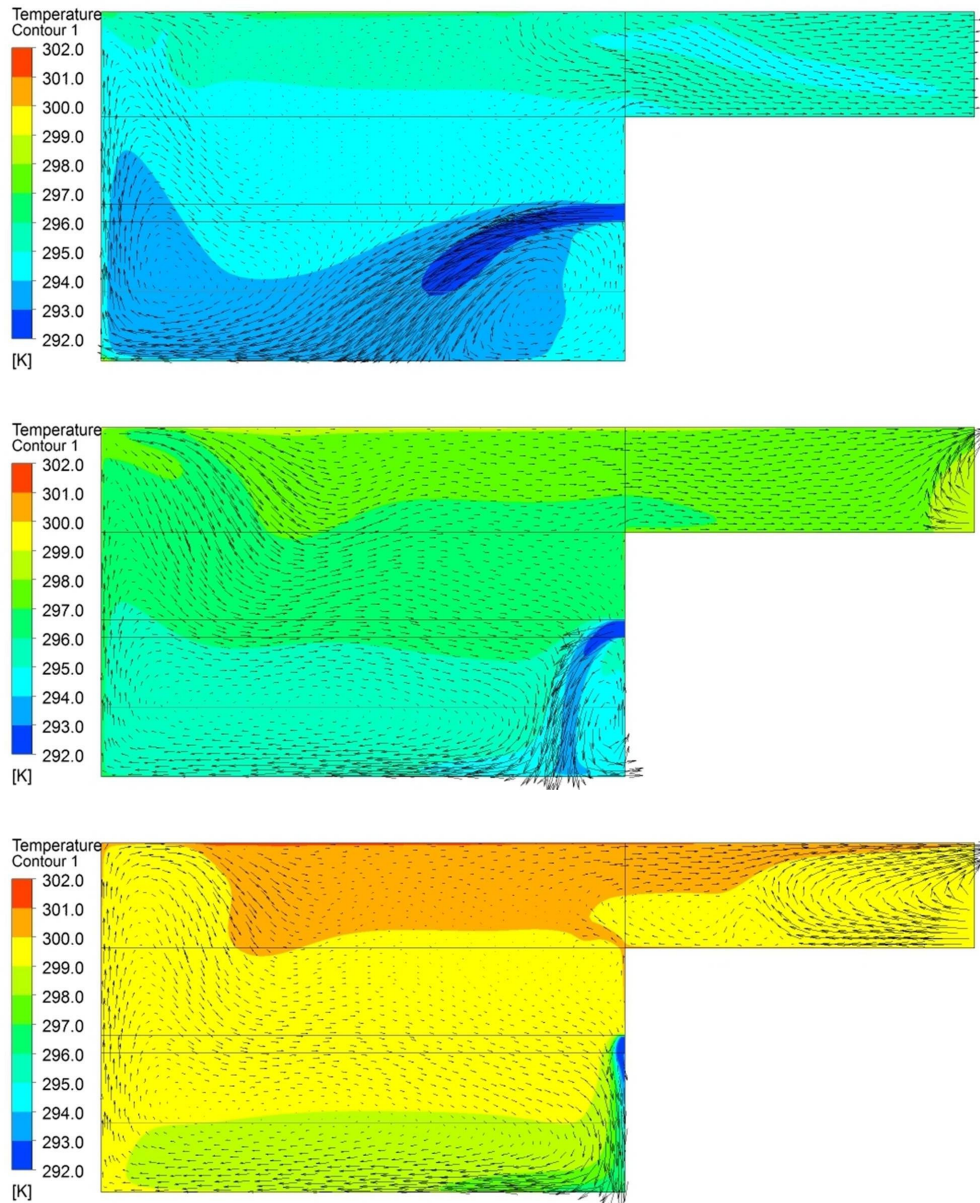


Figure D.1 Temperature contour and velocity distribution plots for reference atrium at plane parallel to the facade intersecting the midpoint of the supply for summer case with double glazing and human occupant load of 3by3 with: supply set to 19°C; heat flux on floor 100W/m<sup>2</sup>, and outside temperature set to 28°C. (Top) Supply set to 1m/s. (Middle) Supply set to 0.5m/s. (Bottom) Supply set to 0.25m/s.

Location	S(iii)a 1m/s	S(iii)a 0.5m/s	S(iii)a 0.25 m/s
	Energy [W]	Energy [W]	Energy [W]
Supply	-14720.0	-7717.0	-3985.2
Outlet	7166.0	1060.0	-1396.2
Facade	1641.0	760.3	-531.3
Floor	5925.3	5924.9	5924.9

Table D.1 Energy quantities for summer case S(iii)a.

Case	Location	Avg. Temp [K]	Max Temp [K]	Stratification [K]	Avg. Temp Near Floor [K]
S(iii)a 1m/s	Entire Atrium	295.1	311.1	0.7	294.8
	Occupied Space	295.2	311.1	-0.4	294.8
S(iii)a 0.5m/s	Entire Atrium	297.1	312.2	1.8	295.9
	Occupied Space	296.4	312.2	-0.1	295.9
S(iii)a 0.25m/s	Entire Atrium	299.8	314.5	1.5	298.9
	Occupied Space	299.3	314.5	0.2	298.9

Table D.2 Interior temperatures for summer case S(iii)a.

Case	Avg. Floor Temp [K]	Avg. Wall Temp [K]	Avg. Façade Temp. [K]
S(iii)a 1m/s	300.1	296.7	297.9
S(iii)a 0.5m/s	301.1	306.1	299.2
S(iii)a 0.25m/s	303.1	301.1	301.4

Table D.3 Average and maximum wall temperatures for summer case S(iii)a.

Case	Max Velocity [m/s]	Avg. Velocity [m/s]
S(iii) a1m/s	1.07	0.19
S(iii) a0.5m/s	0.80	0.18
S(iii) a0.25m/s	0.82	0.18

Table D.4 Average and maximum velocities for summer case S(iii)a.

*Case S(iii)b - Summer day using double glazed system with 4 by 4 occupant load*

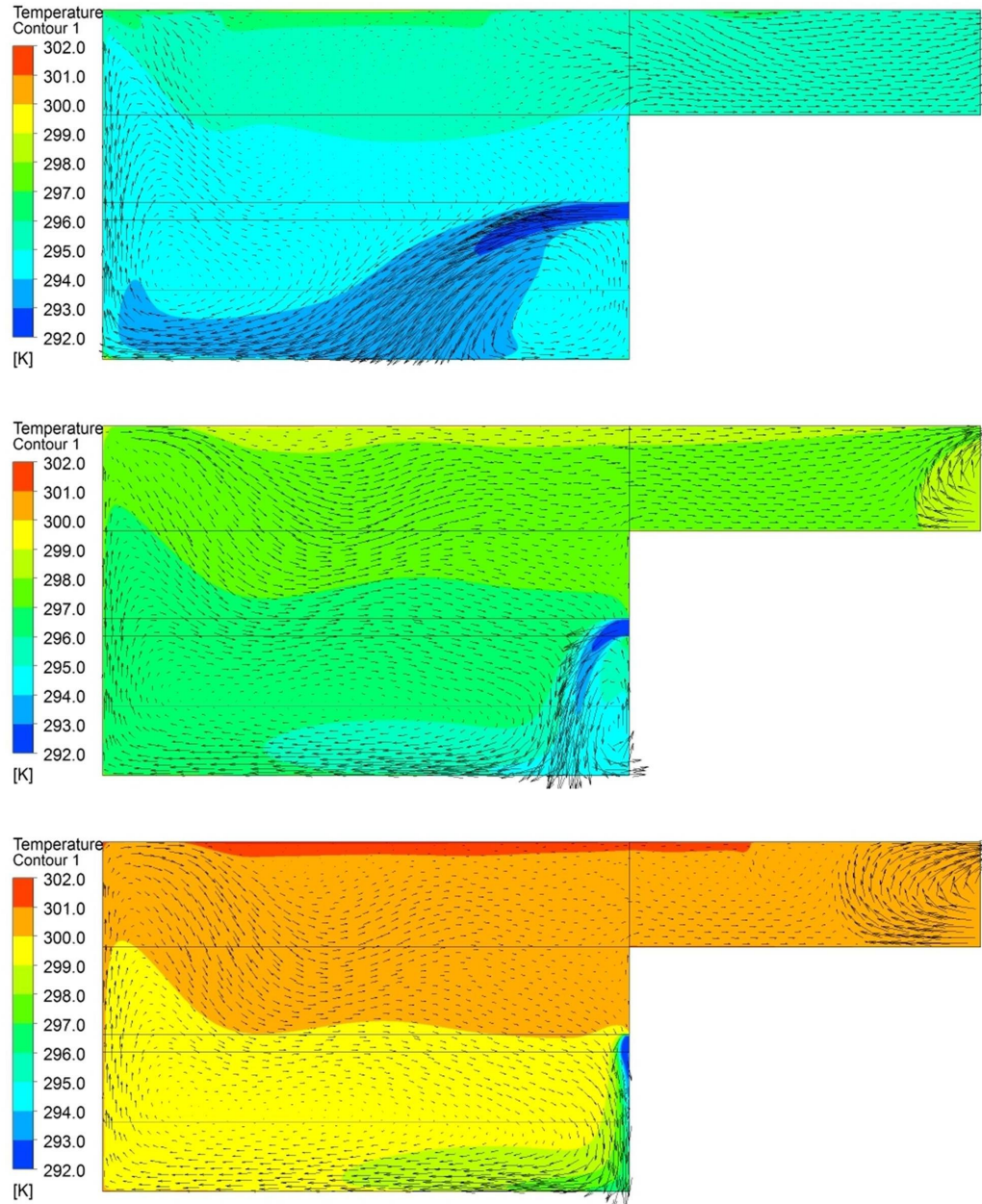


Figure D.2 Temperature contour and velocity distribution plots for reference atrium at plane parallel to the facade intersecting the midpoint of the supply for summer case with double glazing and human occupant load of 4by4 with: supply set to 19°C, heat flux on floor 100W/m<sup>2</sup>, outside temperature set to 28°C, and human heat load of 100W per person. (Top) Supply set to 1m/s. (Middle) Supply set to 0.5m/s. (Bottom) Supply set to 0.25m/s.

Location	S(iii)b 1m/s	S(iii)b 0.5m/s	S(iii)b 0.25 m/s
	Energy [W]	Energy [W]	Energy [W]
Supply	-14729.1	-7621	-4125.1
Outlet	6415	360.5	-1538
Facade	1465.3	413.0	-1215
Floor	6897	6896.9	6896.9

Table D.5 Energy quantities for summer case S(iii)b.

Case	Location	Avg. Temp [K]	Max Temp [K]	Stratification [K]	Avg. Temp Near Floor [K]
S(iii)b 1m/s	Entire Atrium	295.4	312.5	0.8	295.1
	Occupied Space	295.6	312.5	-0.4	295.1
S(iii)b 0.5m/s	Entire Atrium	297.5	312.6	1.8	296.3
	Occupied Space	296.8	312.6	-0.1	296.3
S(iii)b 0.25m/s	Entire Atrium	300.5	314.9	1.6	299.4
	Occupied Space	299.8	314.9	0.2	299.4

Table D.6 Interior temperatures for summer case S(iii)b.

Case	Avg. Floor Temp [K]	Avg. Wall Temp [K]	Avg. Façade Temp. [K]
S(iii)b 1m/s	300.8	297.1	298.2
S(iii)b 0.5m/s	301.6	299.1	299.7
S(iii)b 0.25m/s	303.7	301.7	301.9

Table D.7 Average and maximum wall temperatures for summer case S(iii)b.

Case	Max Velocity [m/s]	Avg. Velocity [m/s]
S(iii)b 1m/s	1.07	0.19
S(iii)b 0.5m/s	0.85	0.19
S(iii)b 0.25m/s	0.87	0.19

Table D.8 Average and maximum velocities for summer case S(iii)b.

*Case W(iii)a - Winter day using double glazed system with 3 by 3 occupant load*

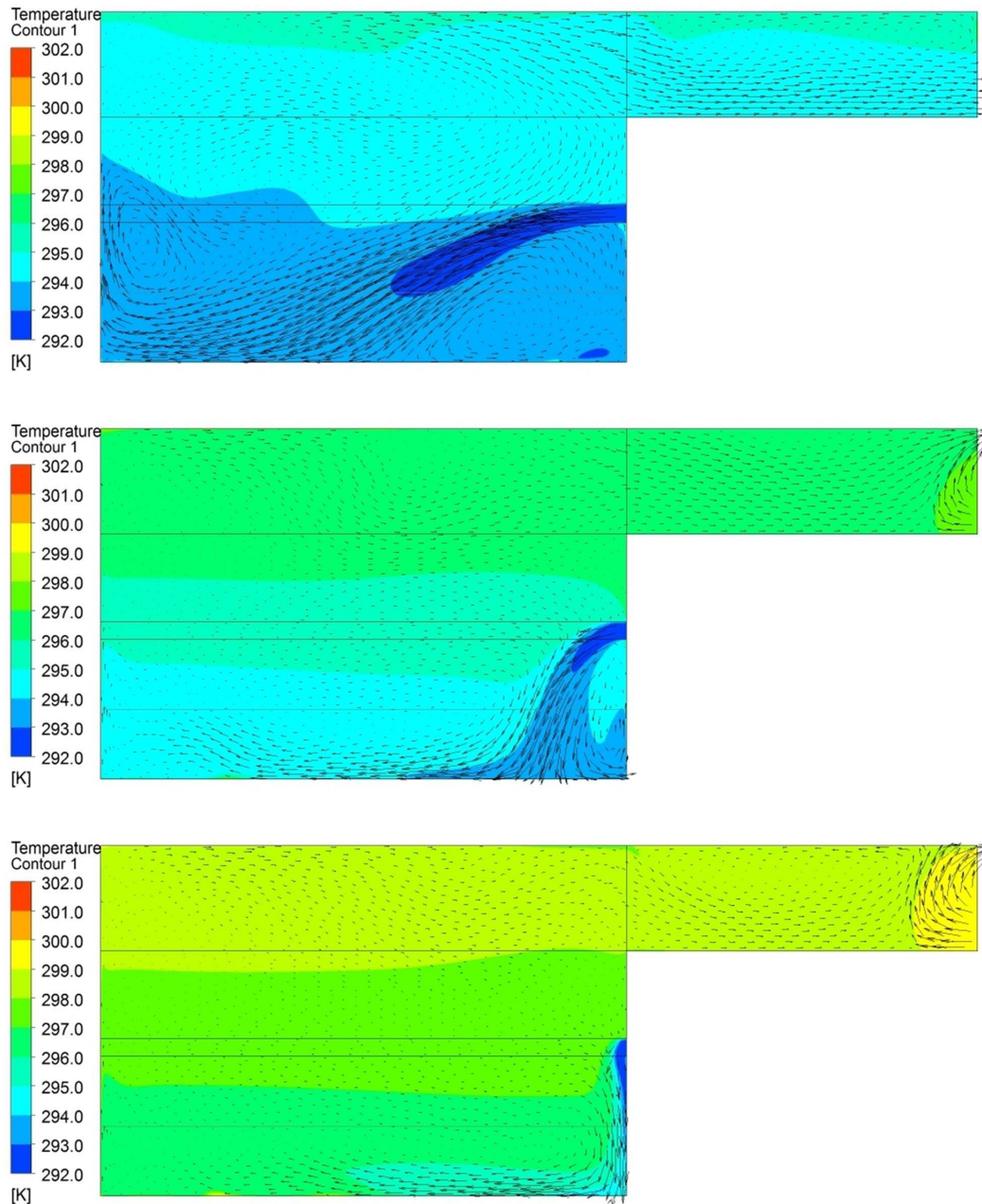


Figure D.3 Temperature contour plots and velocity distribution for reference atrium at plane parallel to the facade intersecting the midpoint of the supply for winter case with double glazing with human occupant load of 3by3: supply set to 19°C, heat flux on floor 50W/m<sup>2</sup>, heat flux on north wall 250W/m<sup>2</sup>, outside temperature set to -5°C, and human heat load of 100W. (Top) Supply set to 1m/s. (Middle) Supply set to 0.5m/s. (Bottom) Supply set to 0.25m/s.

Location	W(iii)a 1m/s	W(iii)a 0.5m/s	W(iii)a 0.25 m/s
	Energy [W]	Energy [W]	Energy [W]
Supply	-14671.8	-7368.7	-3726.4
Outlet	7845.1	1704.2	-1145.5
Facade	-9521.3	-10616.3	-11430.2
Floor	3870.3	3870.3	3870.3
North Wall	12452.6	12452.6	12452.6

Table D.9 Energy quantities for winter case W(iii)a.

Case	Location	Avg Temp [K]	Max Temp [K]	Stratification [K]	Avg. Temp Near Floor [K]
W(iii)a 1m/s	Entire Atrium	294.1	315.6	1.4	293.2
	Occupied Space	293.4	315.6	0.1	293.2
W(iii)a 0.5m/s	Entire Atrium	296.1	319.0	2.0	294.5
	Occupied Space	294.8	319.0	0.3	294.5
W(iii)a 0.25m/s	Entire Atrium	297.9	320.5	2.1	296.2
	Occupied Space	296.6	320.5	0.6	296.2

Table D.10 Interior temperatures for winter case W(iii)a.

Case	Avg. Floor Temp [K]	Avg. North Wall Temp. [K]	Avg. Wall Temp [K]	Avg. Façade Temp. [K]
W(iii)a 1m/s	295.0	298.6	294.7	290.2
W(iii)a 0.5m/s	296.5	300.6	296.5	291.8
W(iii)a 0.25m/s	298.0	302.3	298.1	293.3

Table D.11 Average and maximum wall temperatures for winter case W(iii)a.

Case	Max Velocity [m/s]	Avg Velocity [m/s]
W(iii)a 1m/s	1.15	0.18
W(iii)a 0.5m/s	1.13	0.17
W(iii)a 0.25m/s	1.13	0.18

Table D.12 Average and maximum velocities for winter case W(iii)a.

*Case W(iii)b - Winter day using double glazed system with 4 by 4 occupant load*

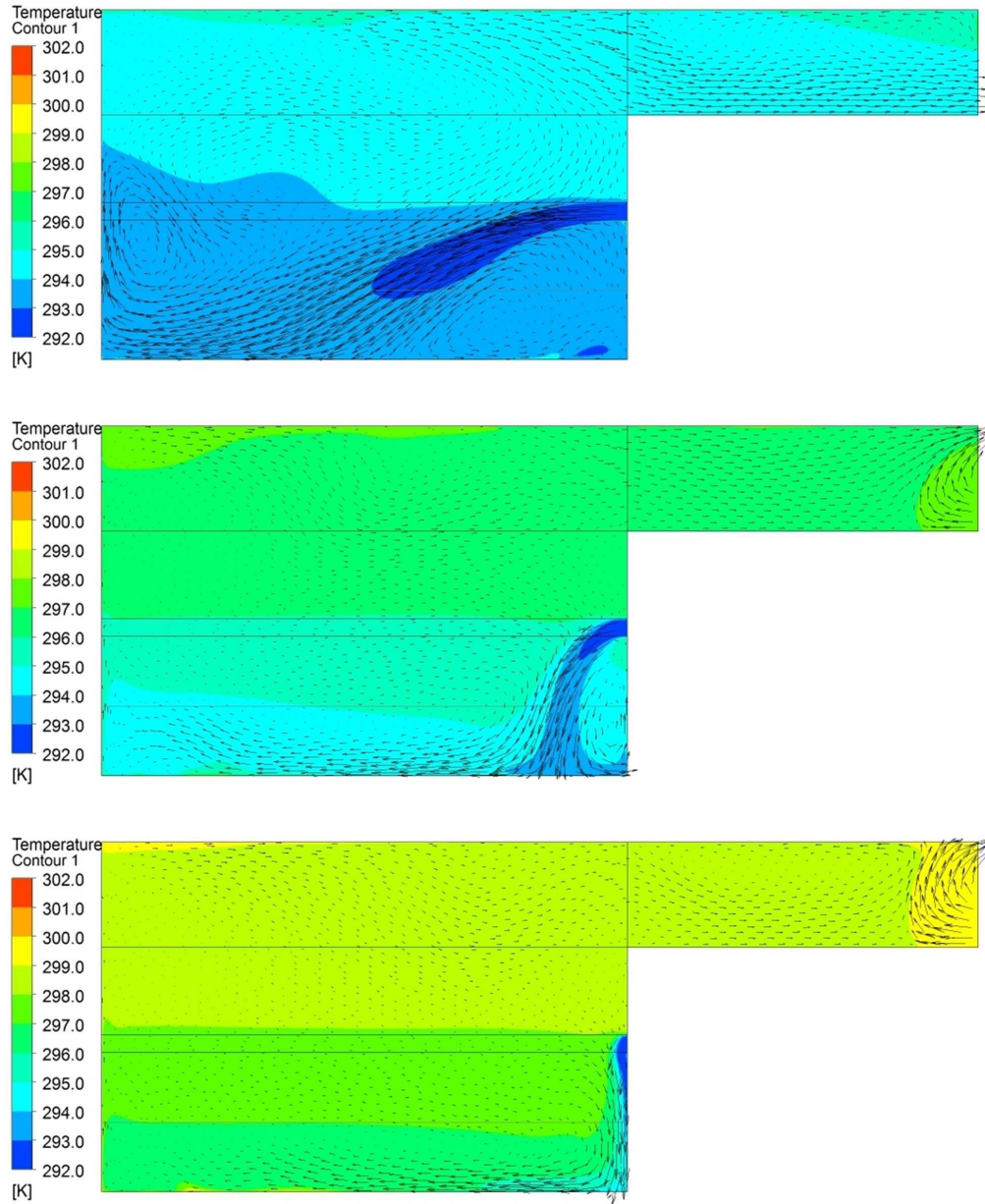


Figure D.4 Temperature contour and velocity distribution plots for reference atrium at plane parallel to the facade intersecting the midpoint of the supply for winter case with double glazing with human occupant load of 4by4: supply set to 19°C, heat flux on floor 50W/m<sup>2</sup>, heat flux on north wall 250W/m<sup>2</sup>, outside temperature set to -5°C, and human heat load of 100W. (Top) Supply set to 1m/s. (Middle) Supply set to 0.5m/s. (Bottom) Supply set to 0.25m/s.

Location	W(iii)b 1m/s	W(iii)b 0.5m/s	W(iii)b 0.25 m/s
	Energy [W]	Energy [W]	Energy [W]
Supply	-14683.0	-7380.3	-3738.2
Outlet	6945.5	78.5	-1602.3
Facade	-9465.1	-9895.1	-11845.3
Floor	4669.8	4669.8	4669.8
North Wall	12452.6	12452.6	12452.6

Table D.13 Energy quantities for winter case W(iii)b.

Case	Location	Avg. Temp [K]	Max Temp [K]	Stratification [K]	Avg. Temp Near Floor [K]
W(iii)b 1m/s	Entire Atrium	294.5	316.2	1.3	293.6
	Occupied Space	293.9	316.2	0.1	293.6
W(iii)b 0.5m/s	Entire Atrium	296.5	319.0	2.0	294.9
	Occupied Space	295.2	319.0	0.3	294.9
W(iii)b 0.25m/s	Entire Atrium	298.4	321.2	2.1	296.7
	Occupied Space	297.1	321.2	0.6	296.7

Table D.14 Interior temperatures for winter case W(iii)b.

Case	Avg. Floor Temp [K]	Avg. North Wall Temp. [K]	Avg. Wall Temp [K]	Avg. Façade Temp. [K]
W(iii)b 1m/s	295.6	299.1	295.2	290.7
W(iii)b 0.5m/s	297.1	301.1	297.1	292.2
W(iii)b 0.25m/s	298.6	302.9	298.7	293.8

Table D.15 Average and maximum wall temperatures for winter case W(iii)b.

Case	Max Velocity [m/s]	Avg. Velocity [m/s]
W(iii)b 1m/s	1.16	0.18
W(iii)b 0.5m/s	1.15	0.17
W(iii)b 0.25m/s	1.14	0.18

Table D.16 Average and maximum velocities for winter case W(iii)b.

## **APPENDIX E: CALCULATION OF SOLAR QUANTITIES**

### E.1 Solar Angles

#### Motivation

The position of the sun is very important to the calculation of the amount of solar radiation and the direction in which sunlight will strike a surface. The calculation of solar angles is necessary to determine accurate solar radiation quantities. Solar angles are dependent on the date, time of day, and the location of interest. The following quantities define the solar position. All equations are from Duffie and Beckman [1980].

#### Angle of Declination

The angle of declination represents the angular position of the sun at solar noon with respect to the plane of the equator. The declination angle is within  $-23.45^\circ \leq \delta \leq 23.45^\circ$ .

$$\delta = 23.45 \frac{\pi}{180} \sin \left[ 2\pi \left( \frac{284 + n}{365.25} \right) \right] \quad \text{Equation E.1}$$

where  $n$  is the day number with the first day being January 1st.

#### Local Standard Time Meridian

The local standard time meridian is a reference meridian for a local time zone.

$$LSTM = 15^\circ \cdot \Delta T_{GMT} \quad \text{Equation E.2}$$

where

$LSTM$  is the Local Standard Time Meridian and

$\Delta T_{GMT}$  is the difference in time from the location and the Greenwich Mean Time.

### Equation of Time

The equation of time is an empirical equation that corrects for the eccentricity of the earth's orbit and the earth's axial tilt. The equation of time is calculated in minutes.

$$EOT = 9.87 \sin(2B) - 7.53 \cos(B) - 1.5(B) \quad \text{Equation E.3}$$

$$B = \frac{360}{365}(d - 81) \quad \text{Equation E.4}$$

where  $d$  is the number of days since the start of the year.

### Time Correction Factor

The net time correction factor accounts for the variation of the local solar time within a given time zone due to the longitude variations within the time zone. The time correction factor is calculated in minutes.

$$TC = 4(LSTM - LONG) + EOT \quad \text{Equation E.5}$$

where

$LSTM$  is the Local Standard Time Meridian,

$LONG$  is the longitudinal position of the location, and

$OT$  is the Equation of Time.

### Local Solar Time

The local solar time corrects the local time using the time correction factor.

$$LST = LT + \frac{TC}{60} \quad \text{Equation E.6}$$

where

$LT$  is the local time and

$TC$  is the time correction factor.

### Hour Angle

The hour angle converts the local solar time into the number of degrees which the sun moves across the sky. At solar noon the hour angle is defined to be  $0^\circ$ .

$$HRA = 15^\circ(LST - 12) \quad \text{Equation E.7}$$

where  $LST$  is the local solar time.

### Altitude Angle

The altitude angle is the angular height of the sun measured from a horizontal surface. The altitude angle is  $90^\circ$  when the sun is at solar noon and  $0^\circ$  at sunrise. The zenith angle is similar to the altitude angle except that it is measured from a vertical surface.

$$\alpha = \sin^{-1}(\sin \delta \sin \phi + \cos \delta \cos \phi \cos(HRA)) \quad \text{Equation E.8}$$

where

$\phi$  is the latitude of the location,

$\delta$  is the declination angle, and

$HRA$  is the hour angle.

### Azimuth Angle

The azimuth angle is the angle in which the sun makes with respect to the north.

$$A_z = \cos^{-1} \left[ \frac{\sin \delta \cos \phi - \cos \delta \sin \phi \cos(HRA)}{\cos \alpha} \right] \quad \text{Equation E.9}$$

*if LST is <12* Azimuth =  $A_z$

*if LST is >12* Azimuth =  $360 - A_z$

where

$\phi$  is the latitude of the location,

$\delta$  is the declination angle,

$\alpha$  is the altitude angle, and

$HRA$  is the hour angle.

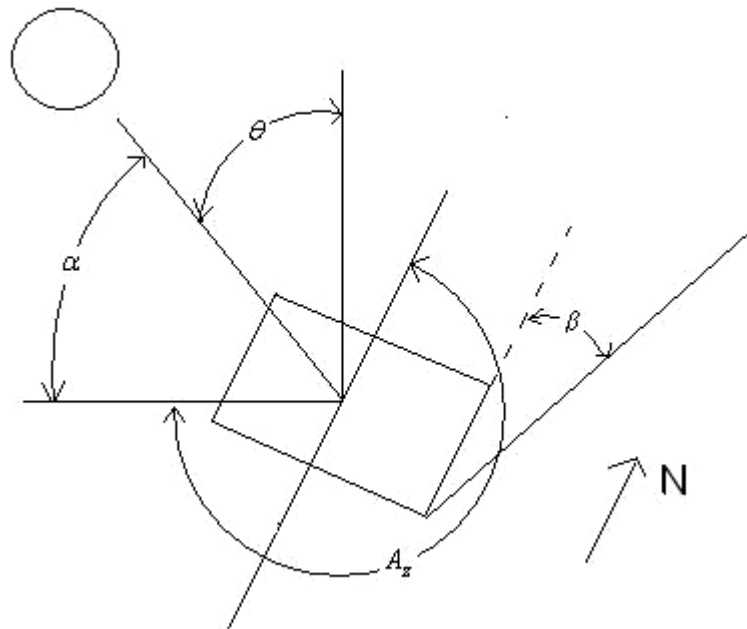


Figure E.1 Diagram of solar angles for a tilted surface. ( $\alpha$  - altitude angle,  $\theta$  - incidence angle,  $\beta$  - surface tilt angle,  $A_z$  - solar azimuth angle)

## E.2 Estimation of Solar Radiation

### Estimation of Clear Sky Beam Radiation

In order to estimate the amount of solar radiation, an approximation for clear sky solar radiation was used. The clear sky radiation model of Hottel [1976] has been used to approximate the solar radiation arriving at vertical and horizontal surfaces.

$$\tau_b = a_o + a_1 e^{\frac{-k}{\cos\theta_z}} \quad \text{Equation E.10}$$

$$a_o^* = 0.4237 - 0.00821(6 - \phi)^2 \quad \text{Equation E.11}$$

$$a_1^* = 0.5055 + (6.5 - \phi)^2 \quad \text{Equation E.12}$$

$$k^* = 0.2711 + 0.01858(2.5 - \phi)^2 \quad \text{Equation E.13}$$

where

$$a_o \equiv r_o a_o^*$$

$$a_1 \equiv r_1 a_1^*$$

$$k \equiv r_k k^*$$

$$G_{on} = 1325 \text{W/m}^2$$

Climate Type	$r_o$	$r_1$	$r_k$
Mid-Latitude Summer	0.97	0.99	1.02
Mid-Latitude Winter	1.03	1.01	1.00

Table E.1 Correction factors for solar radiation transmission through atmosphere.

*Total Solar Beam Radiation*

$$G_{cnb} = G_{on} \tau_b \quad \text{Equation E.14}$$

*Solar Beam Radiation Incident On Horizontal Surface*

$$G_{cnbh} = G_{on} \tau_b \cos \theta_z \quad \text{Equation E.15}$$

*Solar Beam Radiation Incident On Vertical Surface*

$$G_{cnbv} = G_{on} \tau_b \sin \theta \quad \text{Equation E.16}$$

where

$\theta$  is the incidence angle, the angle between the solar beam and the normal to a surface; which has the following relationship for a  $90^\circ$  surface:

$$\cos \theta = -\sin \delta \cos \phi \cos \gamma + \cos \delta \sin \phi \cos \gamma \cos \omega + \cos \delta \sin \gamma \sin \omega$$

Estimation of Clear Sky Diffuse Radiation

Liu and Jordan [1960] developed an empirical relationship between the transmission coefficient for beam and diffuse radiation for clear days.

*Total Diffuse Solar Radiation*

$$\tau_d = 0.2710 - 0.2939\tau_b \quad \text{Equation E.17}$$

*Diffuse Solar Radiation Incident On Horizontal Surface*

$$G_{cdh} = G_{on} \tau_d \cos \theta_z \quad \text{Equation E.18}$$

*Diffuse Solar Radiation Incident On Vertical Surface*

$$G_{cdv} = G_{on} \tau_d \sin \theta \quad \text{Equation E.19}$$

## **Appendix F: Natural Convection Validation**

### F.1 Background

#### *F.1.1 Natural Convection in Atria*

Natural convection is a common heat transfer mechanism occurring in geometries where one or more boundaries are subjected to a heat flux. In an atrium, solar radiation is transmitted through the facade surface and strikes the interior wall surfaces. Natural convection occurs when energy is transferred from the heated surface to the adjacent air. The warm air expands and this difference in density between the heated air and the surrounding air drives the less dense air upwards. Natural convection can be effective in causing circulation within a space, and if the space is designed correctly natural convection can be used to ventilate a space without any use of HVAC systems [Oosthuizen & Lightstone, 2009]. In order to have confidence in CFD predictions of flow and heat transfer in atria geometries, it is valuable to validate predictions against relevant experimental data or benchmark studies.

#### *F.1.2 Definitions*

This appendix presents the results of a validation study of the commercial code ANSYS-CFX for natural convection problems. A range of turbulence models are considered and recommendations are made as to the most appropriate model to use for atria simulations. Tables F.1 and F.2 provide definitions of the variable and the dimensionless groups used in this study.

Symbol	Definition	Value	Unit
$A$	Area of cavity wall		$m^2$
$g$	Gravity acceleration	-9.81	$m/s^2$
$k$	Thermal conductivity	2.61e-2	W/mK
$L$	Cavity side length		m
$Q$	Total heat flow		W
$T$	Temperature		K
$T_C$	Cold wall temperature		K
$T_h$	Hot wall temperature		K
$v$	Vertical velocity		m/s
$\alpha$	Thermal diffusivity	2.19e-5	$m^2/s$
$\beta$	Thermal expansivity	3.36e-3	1/K
$\nu$	Kinematic viscosity	1.54e-5	$m^2/s$

Table F.1. Variable definitions, units and values

Variable	Equation
Dimensionless Temperature	$T_{ND} = \frac{T - T_C}{T_h - T_C}$
Dimensionless Velocity	$v_{ND} = \frac{v}{\sqrt{g\beta L(T_h - T_C)}}$
Average Nusselt Number	$\overline{Nu} = \frac{QL}{Ak(T_h - T_C)}$
Rayleigh Number	$Ra = \frac{g\beta(T_h - T_C)L^3}{\nu\alpha}$

Table F.2. Dimensionless variable definitions

## **F.2 Simulations**

### *F.1.2 Laminar Natural Convection*

#### Description:

This section presents the results of a laminar natural convection validation study with predictions compared to the numerical benchmark solution of de Vahl Davis and Jones [1983].

An air filled differentially heated square cavity was tested at four different Rayleigh numbers:  $10^3$ ,  $10^4$ ,  $10^5$ , and  $10^6$ . The vertical walls were maintained at a constant temperature to satisfy the Rayleigh number and the horizontal walls were defined to be adiabatic. De Vahl Davis and Jones provide their solutions for various quantities such as maximum velocities and Nusselt numbers.

#### Boundary Conditions:

An air filled square cavity with dimensions of 0.1m x 0.1m was modeled. The hot wall and cold wall were defined based on the Rayleigh number. The cold wall was selected to be 300 K while the hot wall temperature was varied. The top and bottom walls were defined to be adiabatic and symmetry was applied on the remaining surfaces to simulate a two-dimensional flow. A diagram of the square cavity and its corresponding boundary conditions can be seen in Figure F.1.

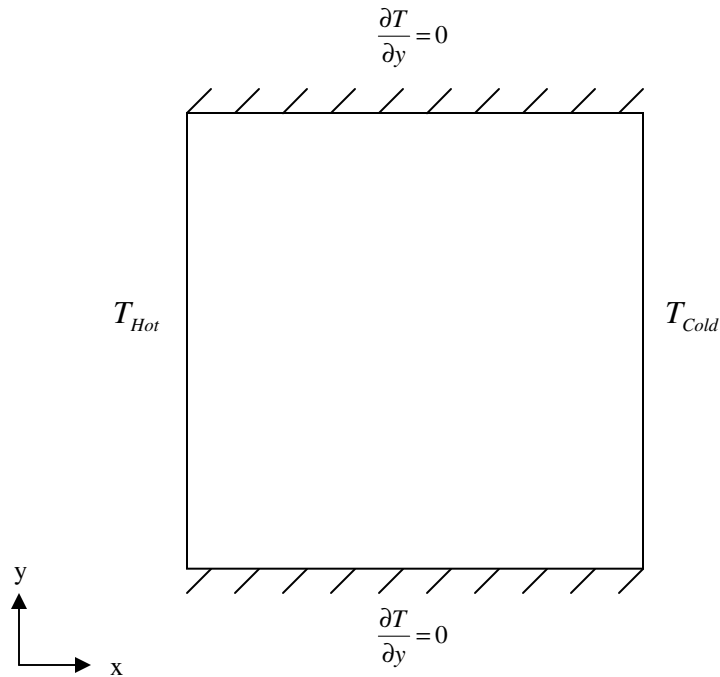


Figure F.1 Geometry and boundary conditions of the laminar natural convection in a square cavity problem.

Analysis:

A fluid flow and heat transfer analysis of this problem has been conducted using the commercial code ANSYS-CFX. Four meshes were constructed and then tested for grid independence: 50x50, 100x100, 200x200, and 400x400. The average Nusselt number for each mesh was compared against its benchmark experimental value. Figure F.2 and Table F.3 demonstrate the accuracy of the predicted solution for the three meshes.

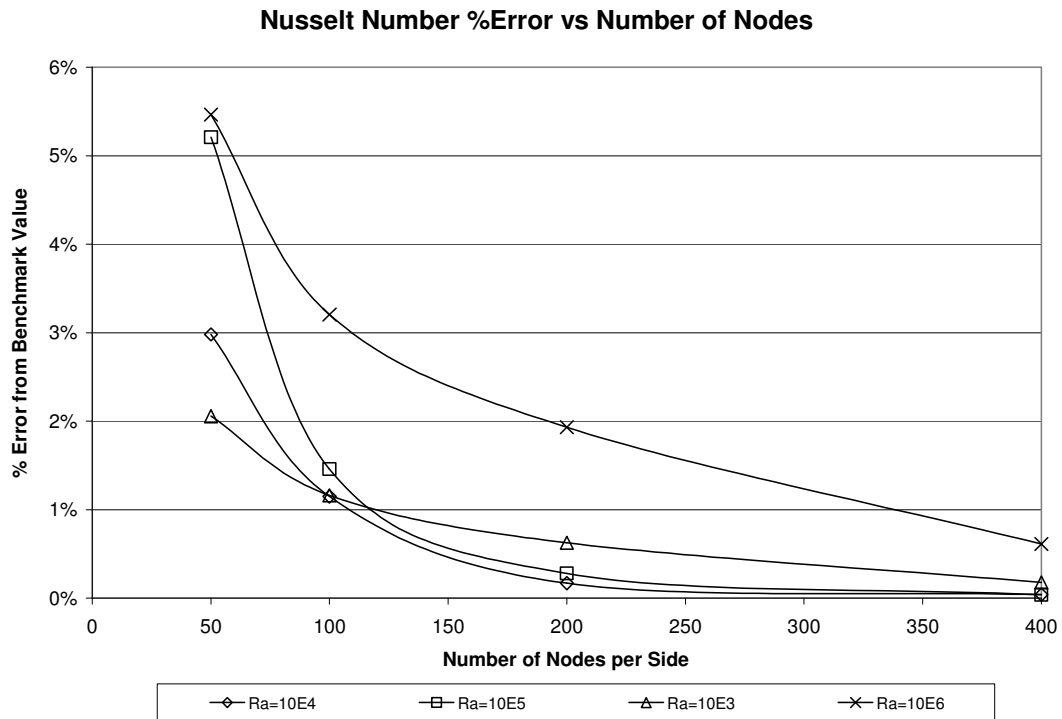


Figure F.2 Plot of Nusselt number percent error versus number of nodes.

Nodes Per Side	Ra 10E3			Ra 10E4		
	BM Nu	Nu	% Error	BM Nu	Nu	% Error
50	1.118	1.141	2.06%	2.243	2.312	2.98%
100	1.118	1.131	1.16%	2.243	2.271	1.15%
200	1.118	1.125	0.63%	2.243	2.249	0.17%
400	1.118	1.120	0.18%	2.243	2.246	0.04%
Extrapolated	1.118	1.116	0.17%	2.243	2.224	0.08%

Nodes Per Side	Ra 10E5			Ra 10E6		
	BM Nu	Nu	% Error	BM Nu	Nu	% Error
50	4.519	4.758	5.21%	8.800	9.281	5.45%
100	4.519	4.588	1.46%	8.800	9.082	3.18%
200	4.519	4.535	0.28%	8.800	8.970	1.93%
400	4.519	4.522	0.04%	8.800	8.854	0.57%
Extrapolated	4.519	4.511	0.11%	8.800	8.826	0.23%

Table F.3 Benchmark and predicted Nusselt Numbers for each case.

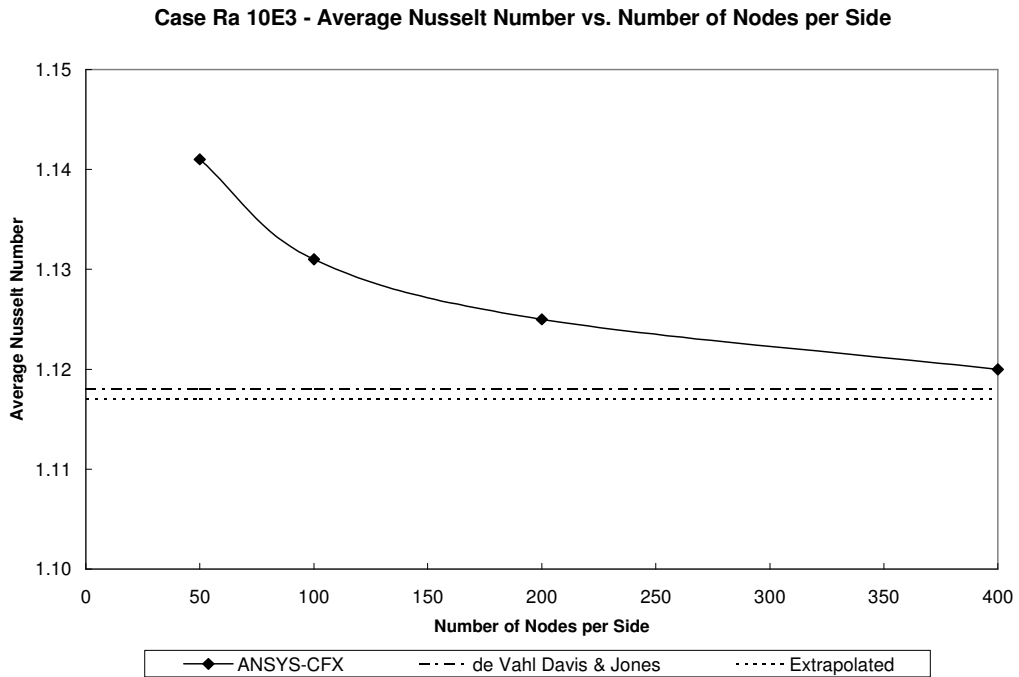


Figure F.3 Plot of average Nusselt number versus number of nodes per side for Rayleigh number equal to  $10^3$ .

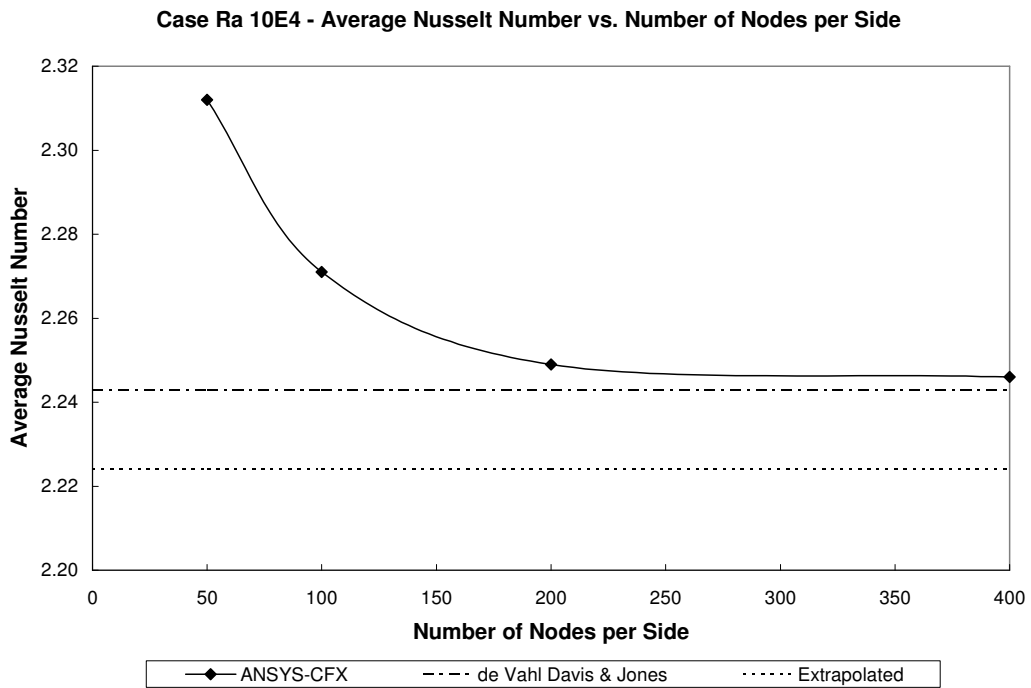


Figure F.4 Plot of average Nusselt number versus number of nodes per side for Rayleigh number equal to  $10^4$ .

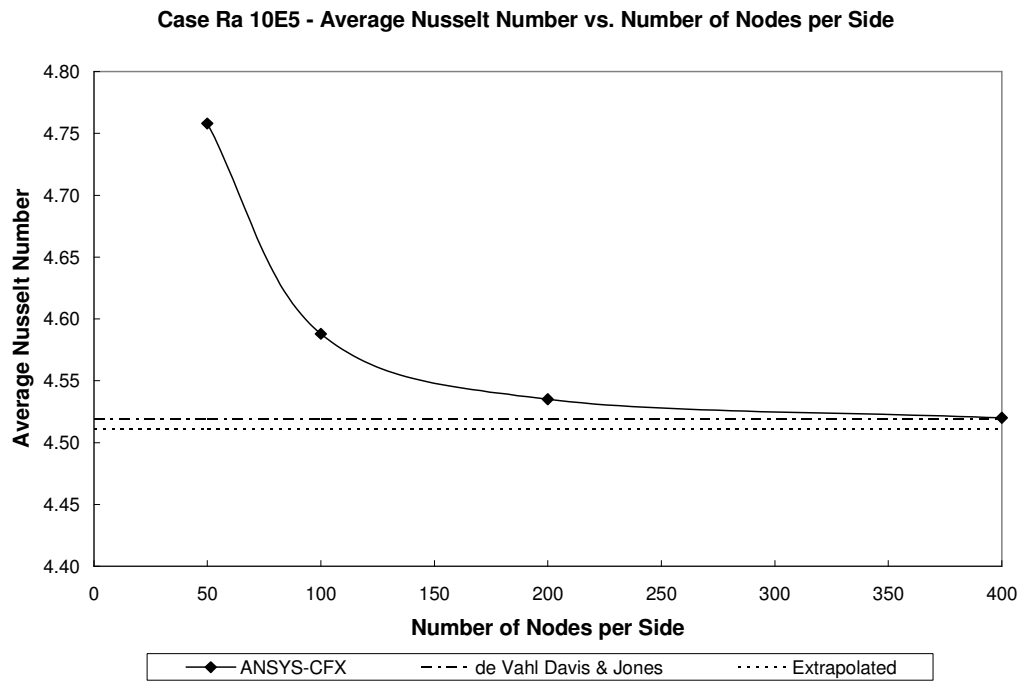


Figure F.5 Plot of average Nusselt number versus number of nodes per side for Rayleigh number equal to  $10^5$ .

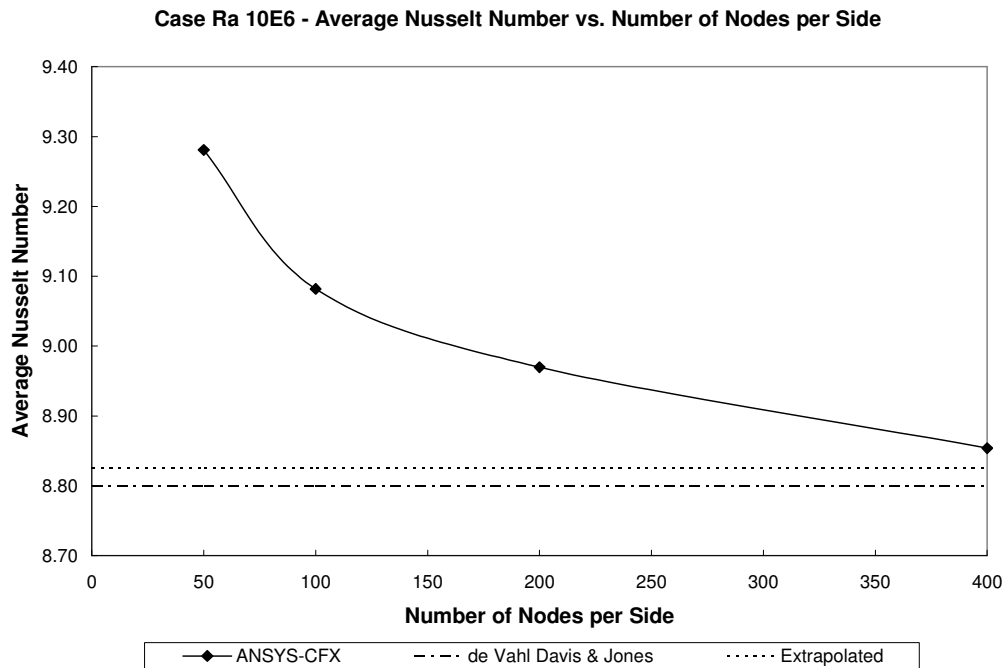


Figure F.6 Plot of average Nusselt number versus number of nodes per side for Rayleigh number equal to  $10^6$ .

It is demonstrated by Table F.3 and Figure F.2 that as expected, as the number of grid points is increased the accuracy in the predicted solution increases. The extrapolated value in Table F.1.1 comes from applying the Richardson extrapolation which presumes that the numerical error is proportional to the grid spacing raised to a power. The power exponent was found to be between 0.75 and 1 for the grids tested. Figures F.3, F.4, F.5, and F.6 are plots of average Nusselt number versus number of nodes per side for each Rayleigh number case. Nonetheless, all cases demonstrate exceptional accuracy as the number of nodes per side increase that demonstrate validation of predicted results against the numerical solution of de Vahl Davis and Jones.

#### Conclusions:

Predicting laminar natural convection flow within a differentially heated square cavity can easily be conducted using the commercial CFD code ANSYS-CFX. The results for Rayleigh numbers  $10^3$ ,  $10^4$ ,  $10^5$ , and  $10^6$  all produced exceptionally accurate results for Nusselt numbers especially as the grid was refined. The validation of predicted results against the numerical solution provided greater confidence in the correct use of the code.

### F.2.2 Turbulent Natural Convection

#### Background:

This section presents a validation study for turbulent natural convection flows. The large length scales in atria geometries tend to result in high Rayleigh numbers. As such, turbulent flow is usually obtained in atria. Code predictions of flow in a cavity are compared to the experimental data of Ampofo and Karayiannis [2003]. The objective of this section is to assess the performance of three different turbulence models against experimental data. The three turbulence models being tested are the k- $\epsilon$ , k- $\omega$ , and the Shear Stress Transport (SST) model.

#### Description:

In this benchmark study, Ampofo and Karayiannis physically modeled an air filled square cavity with differentially heated walls as seen in Figure F.7. The experimental apparatus was 0.75m wide, 0.75 in height, and 1.5m long. The two vertical walls have isothermal temperatures, the hot wall is kept at 50°C and the directly opposite cold wall is kept at 10°C.

#### Measurements:

Three variables were compared between experimental and predicted results: the average Nusselt number, the temperature along a horizontal line through the centre of the cavity, and the vertical velocity component at the centre of the cavity. The measurements of the experiment were taken on the mid plane along the z-direction at the centre line for

velocities and temperatures. It was proven by Penot & N'Dame [1992] and Tian & Karayiannis [Tian and Karayiannis, 2000] that two-dimensional flow is observed at the centre plane of the apparatus when the z-aspect ratio is greater than 1.8. The experimental error reported by Ampofo & Karayiannis [2003] is provided in Table F.4.

Parameter	Uncertainty
Wall Temperature	0.15 K
Air Temperature	0.10 K
Air Velocity	0.07 %
Rayleigh Number	0.62 %
Nusselt Number	0.25-1.13 %

Table F.4 Experimental uncertainty in measurements. (Ampofo & Karayiannis [2003])

Validation:

A CFD model of the experiment was created using ANSYS-CFX.

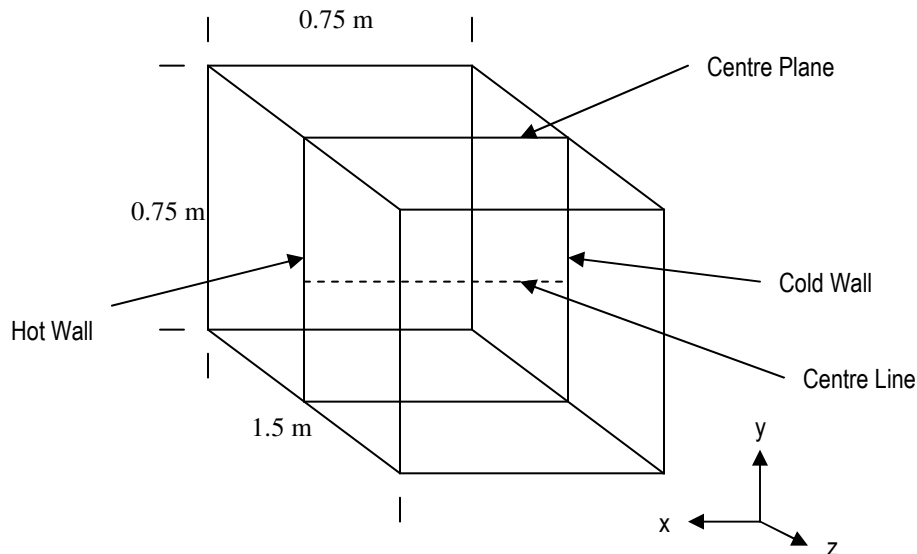


Figure F.7 Geometry of experimental apparatus.

Boundary Conditions:

The hot and cold walls were treated as no slip walls with uniform temperatures of 50°C and 10°C respectively. The top and bottom walls were treated as no slip walls with a temperature specified boundary condition. Although the top and bottom walls were designed to be as close to adiabatic as possible, Ampofo and Karayiannis specify that some heat losses occurred through the top and bottom walls. As a result, temperature measurements along the top and bottom walls are reported and are shown in Figures F.8 and F.9. A temperature distribution for the top and bottom walls was approximated and applied. The Rayleigh number for this experiment was determined to be  $1.58 \times 10^9$ .

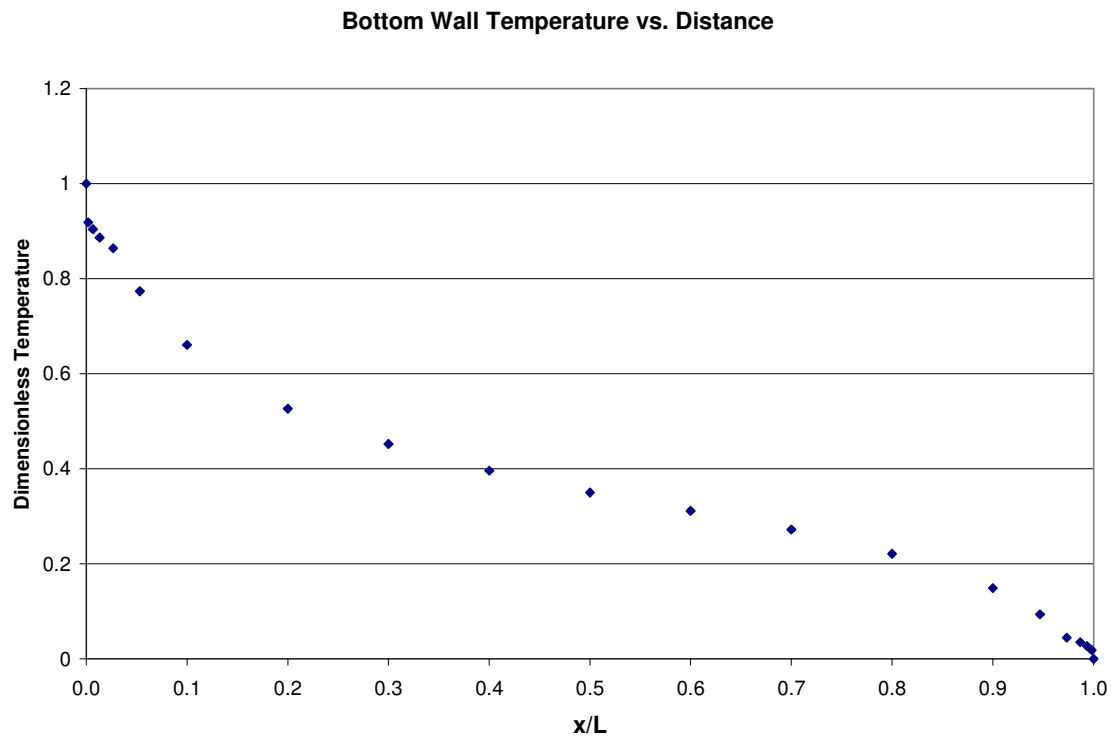


Figure F.8. Bottom Wall temperature distribution

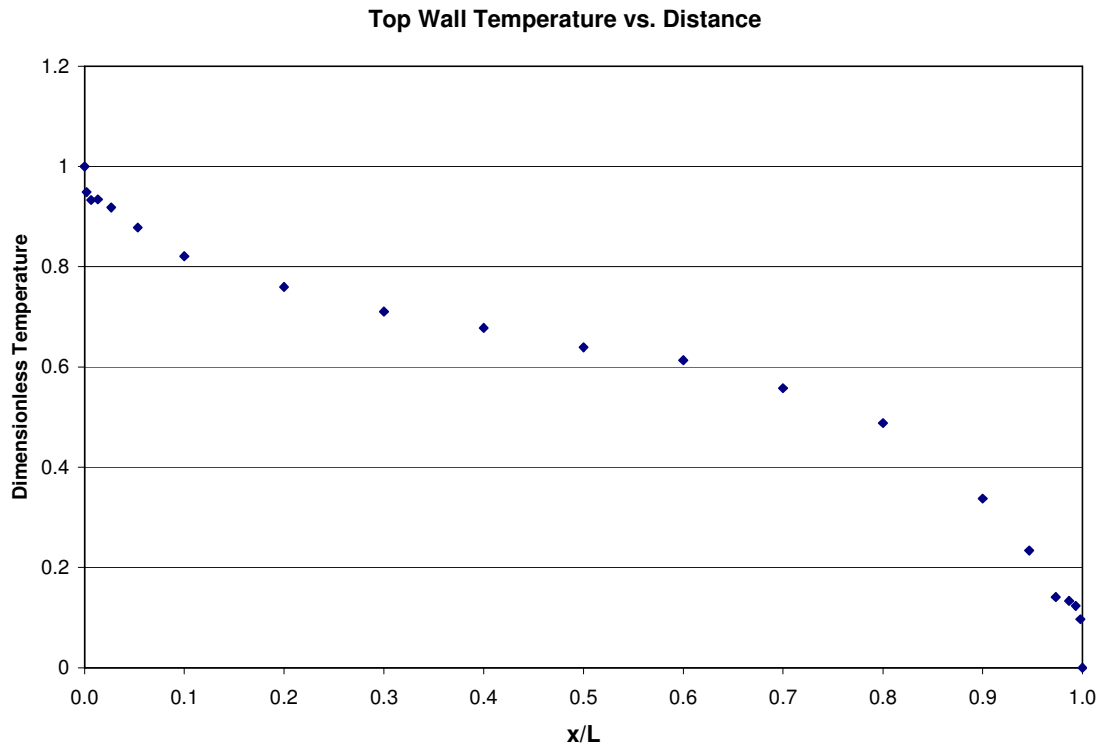


Figure F.9. Top Wall temperature distribution.

Meshes:

The mesh shown in Figure F.10 is the mesh used in these validations. The mesh was refined in areas close to the wall. Grid independence was tested using two meshes 80x80 and 160x160. Difference in results between the 80x80 and 160x160 meshes were negligible ( $\pm 1\%$ ) and the 80x80 mesh was determined to be grid independent. Figure F.11 demonstrates grid independence for the two meshes using the  $k-\omega$  turbulence model.

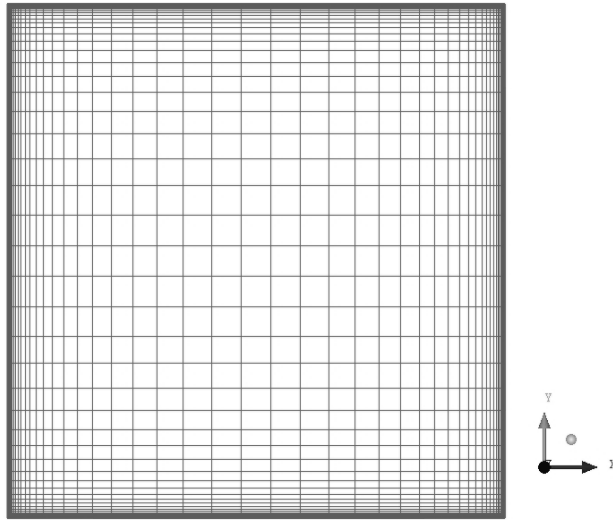


Figure F.10 Example of 80x80 mesh for turbulent natural convection simulations.

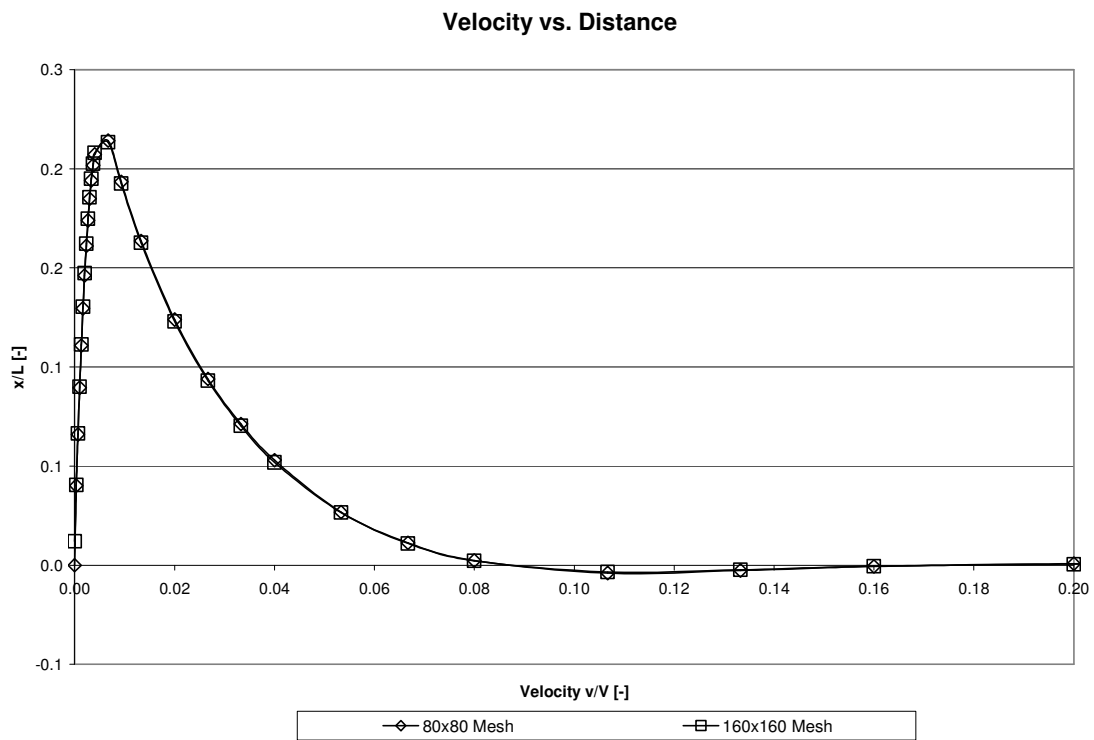


Figure F.11 Grid independence results for meshes 80x80 and 160x160 using the  $k-\omega$  turbulence model.

### Radiation Models:

The surface to surface Discrete Transfer radiation model found in ANSYS-CFX was used in the simulation of this problem. All walls were made of mild steel with a known emissivity of 0.1. The Discrete Transfer radiation model is recommended as a robust radiation model with ease on computational time. [ANSYS-CFX, 2009]

### Relaxation Factors and Timescale:

The local timescale factor was adjusted from ANSYS-CFX's default setting of Automatic Physical Scale to Local Timescale to aid in convergence. The local timescale factor was set to one. Relaxation factors were not adjusted as acceptable converged results were achieved after altering the timescale option.

### Results:

#### *Velocity*

The predicted results for the v-component of velocity using the k- $\epsilon$ , k- $\omega$ , and SST turbulence models can be seen in Figures F.12, F.13, and F.14 respectively. Each figure plots the experimental and predicted results for the v-component of velocity. The results are discussed and analyzed in the following discussion section. A comparison of the peak velocity (v-component) between predicted and experimental values can be seen in Table F.5 for the three different boundary conditions. Table F.5 also indicates the percentage difference between the predicted and experimental values.

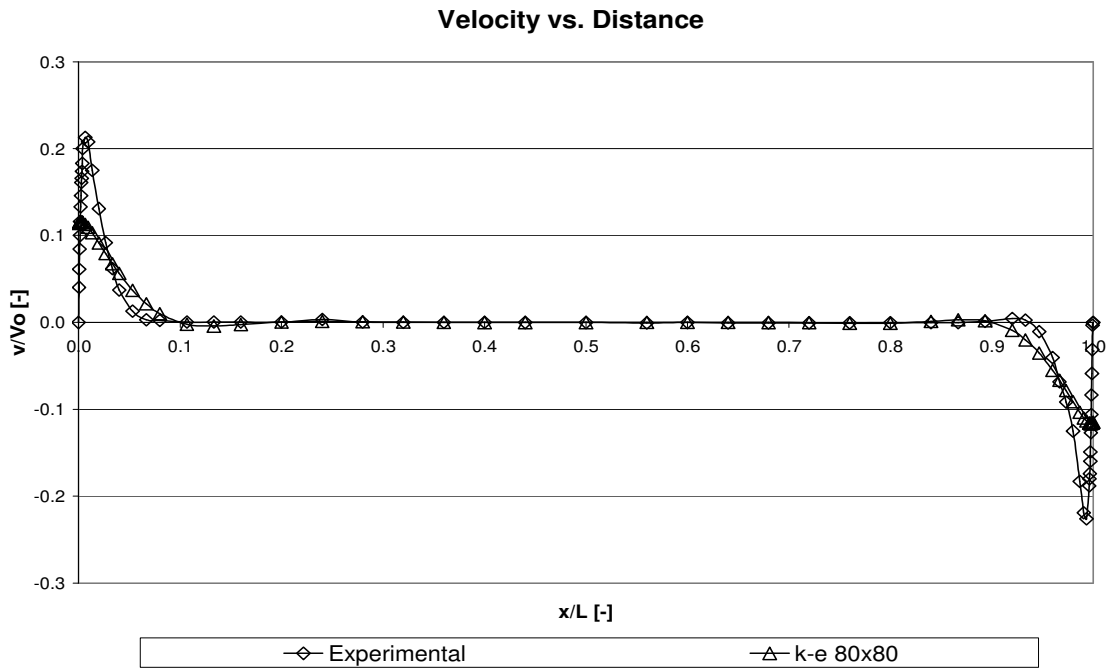


Figure F.12 Predicted velocity profile for k- $\epsilon$  model compared against experimental results.

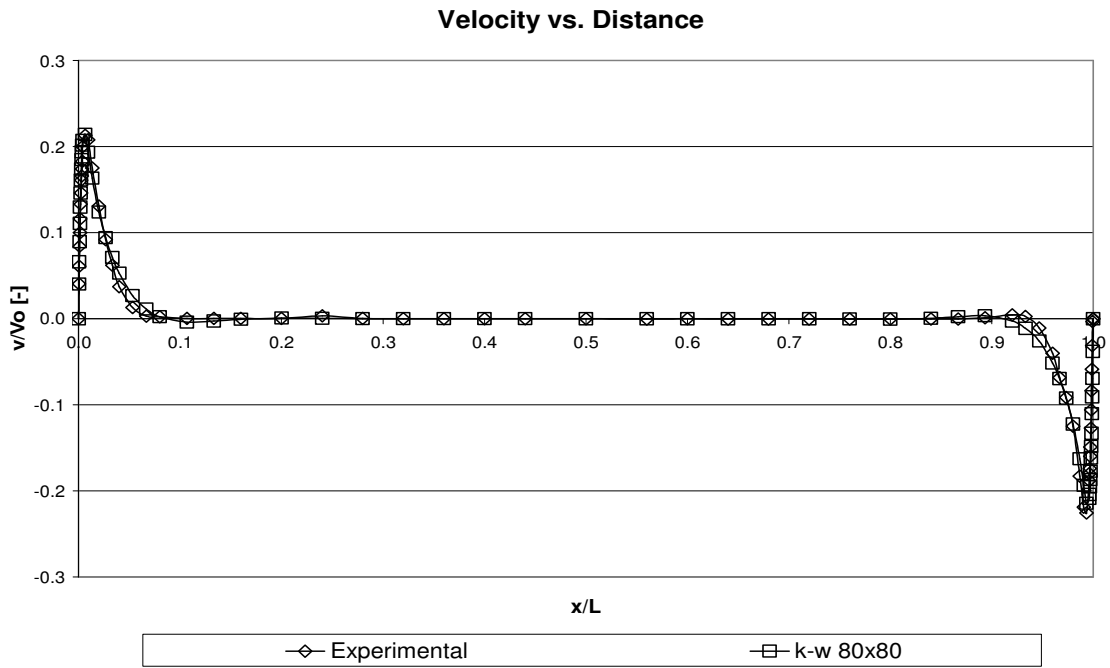


Figure F.13. Predicted velocity profile for k- $\omega$  model compared against experimental results.

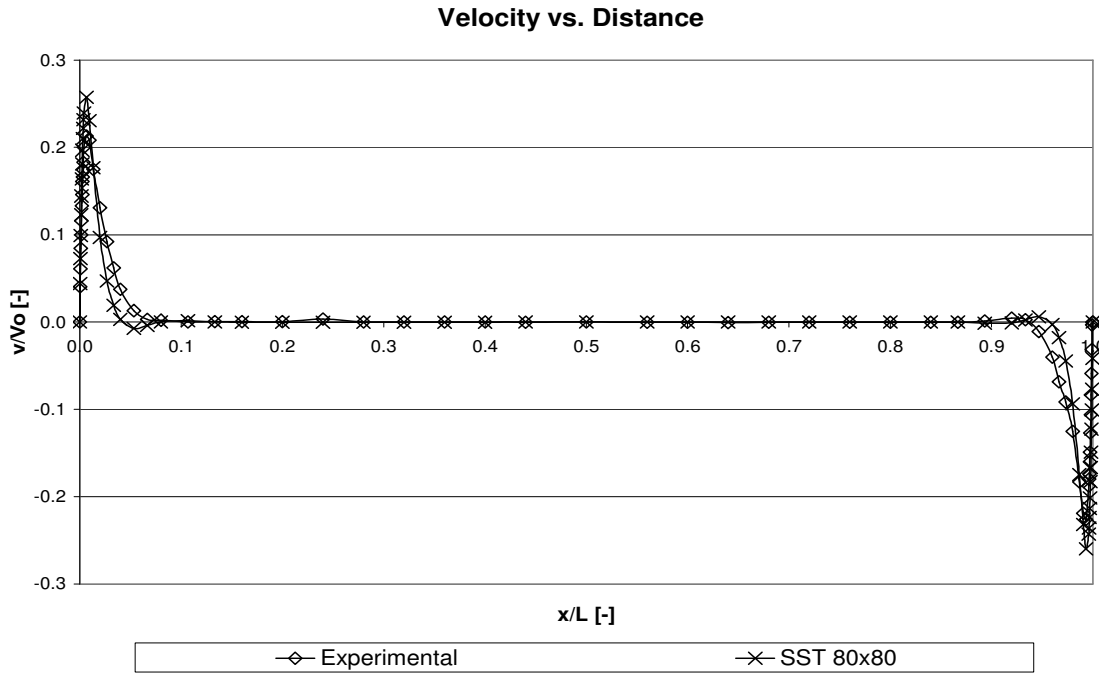


Figure F.14. Predicted velocity profile for SST model compared against experimental results.

<b>Turbulence Model</b>	<b>Location</b>	<b>x/L</b>	<b>Predicted</b>	<b>Experimental</b>	<b>% Error</b>
k- $\omega$ model	Hot Wall	6.67E-03	2.14E-01	2.13E-01	0.6%
	Cold Wall	9.93E-01	-2.15E-01	-2.26E-01	4.9%
k- $\epsilon$ model	Hot Wall	6.67E-03	1.09E-01	2.13E-01	49.0%
	Cold Wall	9.93E-01	-1.10E-01	-2.26E-01	51.1%
SST Model	Hot Wall	6.67E-03	2.56E-01	2.13E-01	20.1%
	Cold Wall	9.93E-01	-2.60E-01	-2.26E-01	15.0%

Table F.5 Predicted velocity ( $v$ -component) values compared against experimental values at two points (locations of maximum velocities near hot and cold walls).

### Temperature

The predicted results for temperature using  $k-\epsilon$ ,  $k-\omega$ , and SST turbulence models can be seen in Figures F.15, F.16, and F.17 respectively. Each figure plots the experimental and predicted results for temperature.

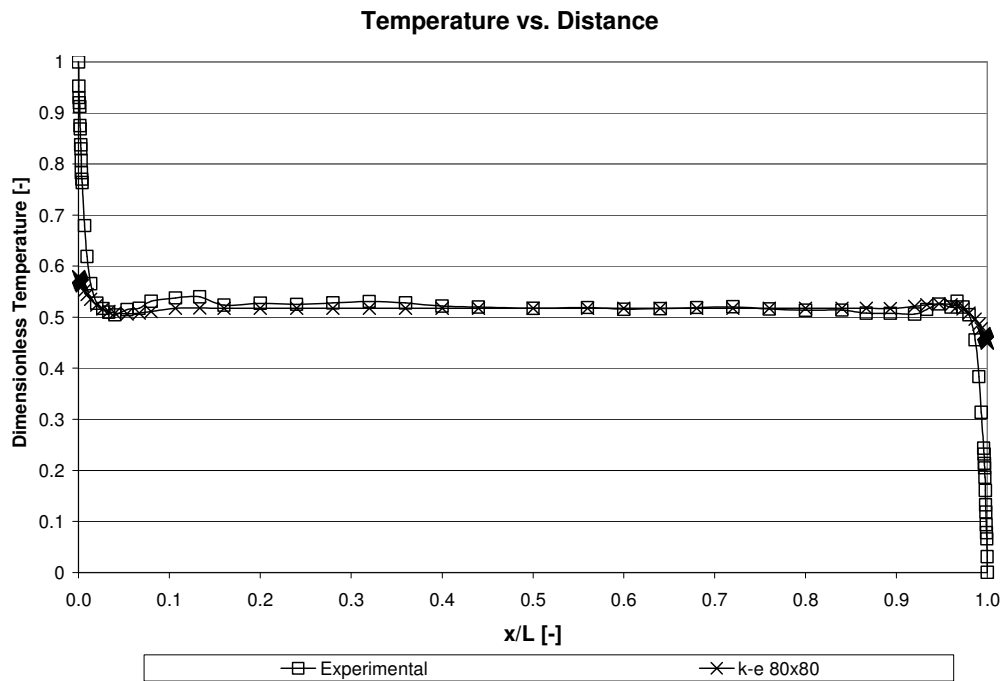


Figure F.15. Predicted temperature profile for  $k-\epsilon$  model compared against experimental results.

### Temperature vs. Distance

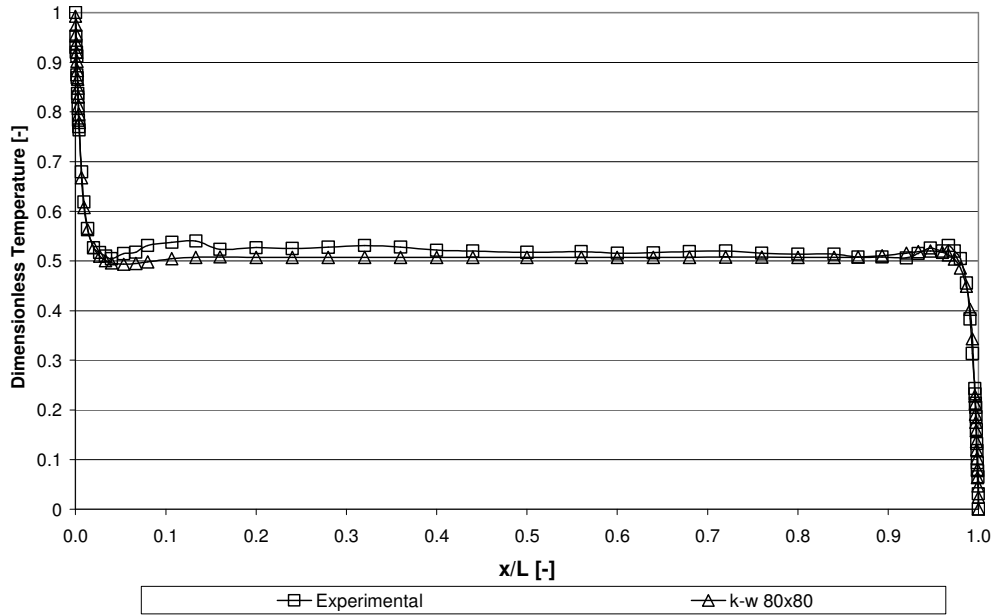


Figure F.16 Predicted temperature profile for k- $\omega$  model compared against experimental results.

### Temperature vs. Distance

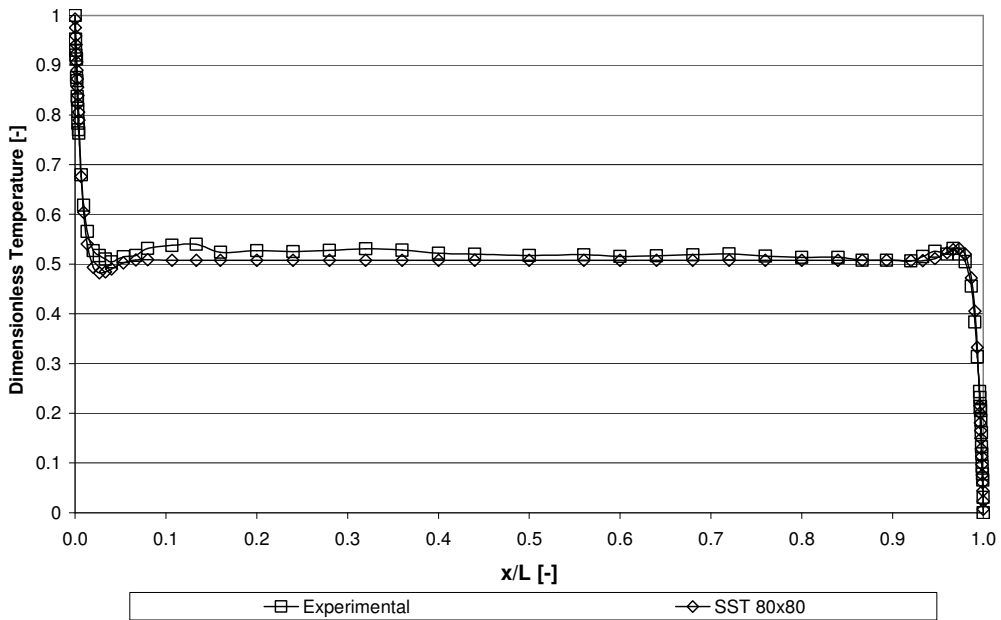


Figure F.17 Predicted temperature profile for SST model compared against experimental results.

Discussion:

*k- $\epsilon$  Model*

Satisfactory convergence of the k- $\epsilon$  turbulence model could not be achieved during simulations. This can be attributed to the wall function constraints in ANSYS-CFX not being satisfied due to the nature of flow and boundary conditions under consideration. The k- $\epsilon$  turbulence model uses a scalable wall function where grid points near the wall are calculated using a log wall boundary layer approximation. The scalable wall function requires a  $y^+$  value between 20 and 100, while having 10 nodes within the boundary layer. The closest  $y^+$  value that could be achieved with 10 nodes within the boundary layer was 0.26, as a result the k- $\epsilon$  turbulence model did not produce reliable accurate results. It should be noted in other similar studies such as Walsh and Leong [2003], the standard k- $\epsilon$  model in other commercial CFD codes were able to produce reliable converged results. This is due to the different wall treatments used amongst various CFD codes. Rundle [2009] also could not produce converged results when simulating this problem using ANSYS-CFX.

*k- $\omega$  Model*

The standard k- $\omega$  model proved to be the most accurate of the three turbulence models. The velocity predictions using the k- $\omega$  turbulence model produced highly accurate results compared to the experimental results of Ampofo and Karayiannis. By analyzing the expanded image of the boundary layer in Figure F.18, it can be seen that the standard k- $\omega$  model resolves the boundary layer effectively matching closely the

experimental data. Using the experimental measurement for peak velocity near the hot wall and cold wall as points of comparison, the predicted values differed with experimental by 0.6% and 4.9% respectively.

The temperature profile produced by the  $k-\omega$  turbulence model was also in good agreement with the experimental data and proved to be the most accurate model with results varying within  $\pm 5\%$  in some locations. The enlarged image of the thermal boundary layer near the hot wall seen in Figure F.19 demonstrates that the thermal boundary layer is also resolved well. Of the three turbulence models tested the  $k-\omega$  turbulence produced the most accurate temperature results when compared to experimental data.

The average Nusselt number was calculated for each of the four walls. The Nusselt numbers for each location is provided in Table F.6. The hot wall and cold wall Nusselt numbers were found to differ from experimental by 1.7% and 7.5% respectively. Heat loss through corners and the polynomial approximation of the top and bottom wall boundary conditions are attributing factors to the differences in average Nusselt numbers.

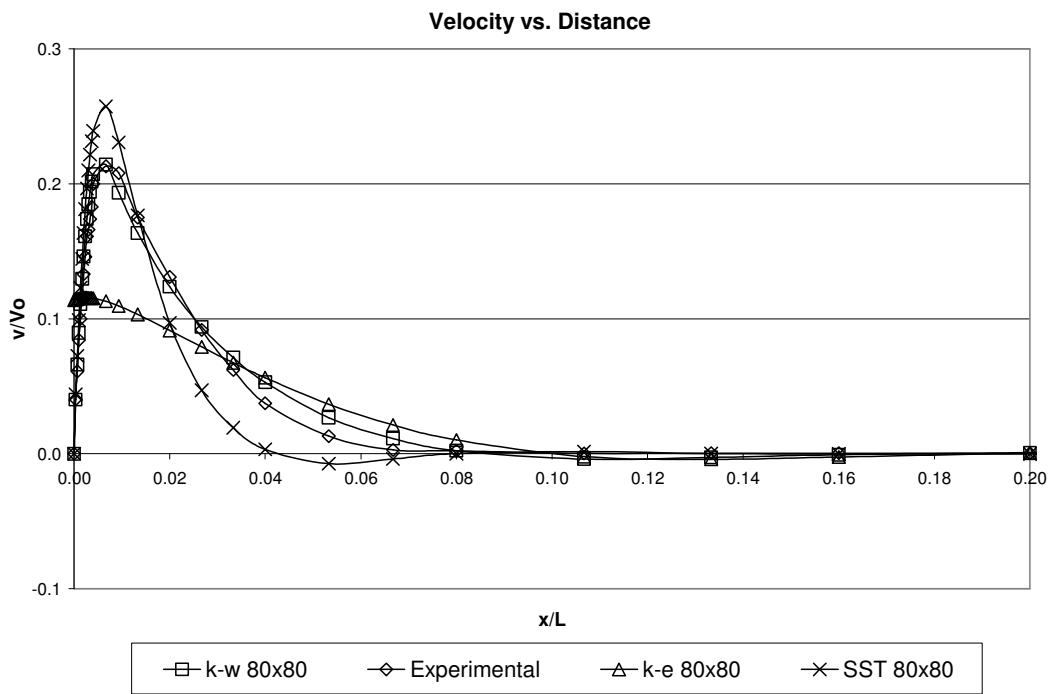


Figure F.18 Expanded image of velocity profiles near hot wall.

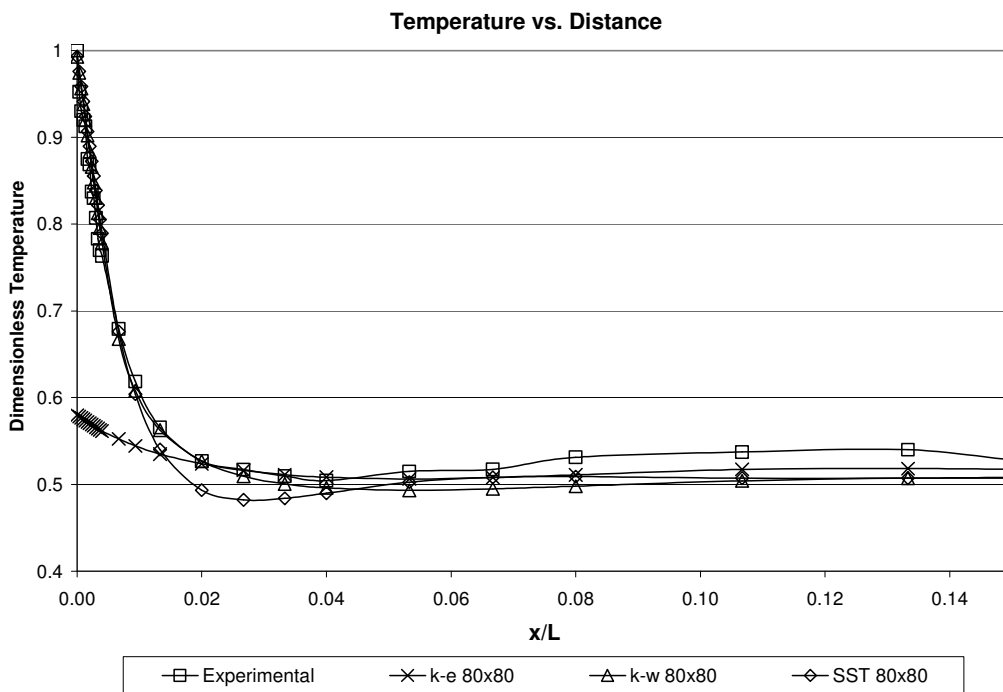


Figure F.19 Expanded image of temperature profile near hot wall.

<b>Turbulence Model</b>	<b>Location</b>	<b>Nusselt Number</b>	<b>Nusselt Number BM</b>	<b>% Error</b>
k- $\omega$ linear temp	Hot Wall	63.35	62.90	0.7%
	Cold Wall	-62.75	-62.60	0.2%
	Top Wall	-14.58	-13.90	4.9%
	Bottom Wall	14.00	14.40	-2.8%

Table F.6 Nusselt numbers using the k- $\omega$  turbulence model.

### *SST Model*

As seen in Figure F.18, the SST turbulence model provided fairly accurate velocity predictions when compared to the benchmark data. In the boundary layer near the hot wall, the SST model over predicts the velocity values in the  $x/L$  region 0 to 0.02. Also, the SST model under predicts the velocity in the  $x/L$  region 0.02 to 0.8 and causes a dip in the velocity profile that is not seen in the experimental data or the k- $\omega$  model results. This under prediction is mainly due to the SST model's blending function from the k- $\omega$  model to the k- $\epsilon$  model which is expected to occur within this region of the velocity profile [ANSYS, 2010]. It should be noted that the SST model produces a significantly thinner boundary layer than the k- $\omega$  model. When compared against the k- $\omega$  model and k- $\epsilon$  model, the k- $\omega$  model proves to be more accurate in modeling the velocity profile and matching the experimental data.

As seen in Figure F.19, the temperature profile deviated within  $\pm 7\%$  in some locations. The SST model produced similar results to the  $k-\omega$  model and closely matched the benchmark data for temperature. However, the SST model slightly under predicts the temperature in the  $x/L$  region 0.02 to 0.04 and causes a small dip in the temperature profile that is not seen in the experimental data. This under prediction is quite small and differs from the benchmark data at a maximum of 0.77K.

The SST model produced Nusselt numbers of varying accuracy compared to experimental results. The temperature specified boundary condition provided a hot wall Nusselt number with an error of 0.21% and a cold wall Nusselt number with an error of 3.4%. The top and bottom wall Nusselt numbers had errors of 27.1% and 16.2% respectively. When compared to the results of the  $k-\omega$  model, the  $k-\omega$  model produced greater accuracy in Nusselt numbers..

<b>Turbulence Model</b>	<b>Location</b>	<b>Nusselt Number</b>	<b>Nusselt Number BM</b>	<b>% Error</b>
SST temp. specified	Hot Wall	62.77	62.90	0.2%
	Cold Wall	-64.73	-62.60	3.4%
	Top Wall	-10.14	-13.90	27.1%
	Bottom Wall	12.07	14.40	16.2%

Table F.7 Nusselt numbers using the SST turbulence model.

Conclusions:

Overall, this study demonstrated that Ampofo and Karayiannis' turbulent natural convection benchmark problem can be modeled and simulated using the CFD code ANSYS-CFX. Although there were some discrepancies when comparing specific quantities the following conclusions can be made from this study:

1. Of the three turbulence models examined in this study, the  $k-\omega$  model proved to be the most accurate in verifying the benchmark results of Ampofo and Karayiannis. The velocity and temperature profiles of the  $k-\omega$  model matched closely to the profile of the experimental data.
2. The  $k-\epsilon$  model did not produce any reliable converged results likely due to the requirements of the scalable wall function required by ANSYS-CFX. Although numerous attempts were made to satisfy the required  $y^+$  values and number of boundary layer grid points, satisfactory convergence could not be achieved. Thus the results attained from these simulations were not reliable.
3. The SST turbulence model performed fairly well providing moderately accurate results however results were not as accurate using the  $k-\omega$  turbulence model.

4. Radiation effects should be accounted for when modeling this problem. Radiation accounts for 6-10% of the overall heat transfer within the square cavity.

### **F.3 Conclusion**

It is clear from these validation exercises that laminar and turbulent natural convection flow can be modeled using ANSYS-CFX and produce highly accurate predicted results. It is observed that there is greater ambiguity in the predicted results of turbulent cases versus the results of laminar cases, however this is expected as calculations involving turbulent flows often require modeled equations. The turbulent natural convection problem of Ampofo & Karayiannis provided a sound method of testing the performance of three standard turbulence models. The end results indicates that the  $k-\omega$  model excels beyond the  $k-\varepsilon$  and SST models by providing higher accuracy for both momentum and heat transfer quantities. As a result of this study, the  $k-\omega$  model is the optimum choice that will be used in the study of fluid flow and heat transfer in atrium geometries.